Engineered Thermally Sprayed Electrodes for Hydrogen Production by Alkaline Water Electrolysis

Maniya Aghasibeig

A Thesis

In the Department

of

Mechanical and Industrial Engineering

Presented in Partial Fulfillment of the Requirements

For the Degree of

Doctor of Philosophy (Mechanical and Industrial Engineering) at

Concordia University

Montreal, Quebec, Canada

December 2015

CONCORDIA UNIVERSITY
School of Graduate Studies

This is to certify that the thesis prepared

By: Maniya Aghasibeig

Entitled: Engineered Thermally Sprayed Electrodes for Hydrogen Production by Alkaline Water Electrolysis

and submitted in partial fulfillment of the requirements for the degree of

Doctor of Philosophy (Mechanical Engineering)

complies with the regulations of the University and meets the accepted standards with respect to originality and quality.

Signed by the final examining committee:

_____ Chair
Dr. F. Haghighat

_____ External Examiner
Dr. T. Coyle

_____ External to Program
Dr. M. Nokken

_____ Examiner
Dr. M. Pugh

_____ Examiner
Dr. P. Wood-Adams

_____ Thesis Co-Supervisor
Dr. R. Wuthrich

_____ Thesis Co-Supervisor
Dr. C. Moreau

_____ Thesis Co-Supervisor
Dr. A. Dolatabadi

Approved by: _____
           Dr. A. Dolatabadai, Graduate Program Director
December 7, 2015 _____
           Dr. A. Asif, Dean
           Faculty of Engineering and Computer Science

ABSTRACT

Engineered Thermally Sprayed Cathode Electrodes for Hydrogen Production by Alkaline Water Electrolysis

Maniya Aghasibeig, Ph.D.

Concordia University, 2015

Alkaline water electrolysis is one of the most promising methods for producing high purity hydrogen to be used as a clean and renewable energy carrier. However, due to the high costs of the electrolysers in addition to high energy consumption of the electrolysis process, this method is still not used for large scale hydrogen production in industrial applications. The costs associated with the materials and energy loss of this technology can be reduced by decreasing the hydrogen evolution overpotentials by using durable and inexpensive electrocatalysts with high intrinsic activities and large active surface areas.

The main objective of this work is to manufacture cathode electrodes for the hydrogen evolution reaction (HER) with modified surface structures and large effective areas, using different thermal spray techniques. For this purpose, new methodologies for manufacturing the electrodes are introduced while the surface morphology of the electrodes is designed and engineered by the coating processes. Nickel is used as electrode material as it shows high electrocatalytic activity, has high stability in alkaline solutions and is relatively inexpensive compared to noble metals with the best activities. Suspension plasma spray (SPS), high velocity oxy-fuel (HVOF) and cold spray are introduced as novel methods for producing nickel electrodes for the HER. A combination of atmospheric and suspension plasma spray, with optimized parameters toward enhancement of the electrode surface area, is effectively used for development of multiscale electrode surface structures with micron and nanosized features. In addition, the surface texture of the electrodes is

engineered by deposition of three-dimensional fin arrays by employing mesh screens when either the combined atmospheric and suspension plasma spray or HVOF processes were used. For these electrodes the surface area was mainly enhanced by deposition of the particles at normal and off-normal angles. The produced hierarchical multiscale electrode structures enhanced the electrocatalytic activity for the HER by increasing the accessibility of the electrode surface to the electrolyte besides facilitating the hydrogen bubble detachment. Finally, cold spray was used to manufacture the electrodes with large activities by peening of the electrode surface by the solid-state nickel particles during the deposition process. The activity of the electrodes was enhanced by increasing the surface defects and changing the electronic structure of the electrodes induced by the peening effect.

DEDICATION

Dedicated to my loving parents.

تقدیم به پدر و مادر عزیزم.

ACKNOWLEDGEMENTS

First and foremost, I would like to express my sincerest gratitude to my advisors Dr. Ali Dolatabadi, Dr. Rolf Wuthrich and Dr. Christian Moreau. Thank you all for giving me the opportunity to be a part of your groups and work with you over the course of this research. Your continuous support, guidance, patience and encouragement have immensely inspired me throughout the completion of this degree. It has been a privilege working with you.

I am grateful to Dr. Pugh, Dr. Drew and Dr. Medraj for giving me permission to use the facilities in their laboratories. I would like to thank Dr. Mohammad Jahazi at École de Technologie Supérieure (ETS) and Mr. John Gavita at Olympus Corporation for providing access to their confocal laser scanning microscopy. I am grateful to Dr. Sasha Omanovic at McGill University for giving permission to use the EIS system in his laboratory. Many Thanks to Mr. Nate Dennehy at Plasma Giken for his assistance with the cold spray experiments. I am thankful to Mr. Robert Oliver for his help in the Thermal Spray Laboratory.

I wish to thank the entire fellow members of Thermal Spray and Electrocatalytic Green Engineering Groups, particularly Dr. Fadhel Ben Ettouil, Navid Sharifi and Lucas Hof. Fadhel, thank you for always being there and helping me with the experiments during those long days in the thermal spray lab. Navid, I feel so fortunate knowing you and working with you. Thank you for your support and friendship from the first day we started to work together in the thermal spray lab. Lucas, I have greatly benefited from your help and support. Working with you has definitely been a rewarding experience. Jana, Andrew, Rahman, Frederic, Milad, Fariba, Ali, Alex, Bishoy, Omid, Shahin, Damir and Marc thank you for being such a helpful and great team.

I would like to extend my thanks to my friends Amin, Hanieh, Kourosh, Mohammad and Reza for always being there for me throughout the most challenging moments. I give

TABLE OF CONTENTS

LIST OF FIGURES

LIST OF TABLES

LIST OF ABBREVIATIONS

APS   Atmospheric Plasma Spray

BET   Brunauer, Emmett and Teller

BSE   Backscattered Electrons

CLSM   Confocal Laser Scanning Microscopy

CPE   Constant Phase Element

DOE   Design of Experiments

EBSD   Electron Backscatter Diffraction

ECDLC   Electrochemical Double Layer Capacitance

EIS   Electrochemical Impedance Spectroscopy

FRA   Frequency Response Analysis

GPES   General Purpose Electrochemical System

HER   Hydrogen Evolution Reaction

HVOF   High Velocity Oxy-Fuel

ICP   Inductively Coupled Plasma

ND   Normal Direction

PCD   Pearson's Crystal Data

PD   Perpendicular Direction

PVP   Polyvinylpyrrolidone

SD   Standard Deviation

SEM   Scanning Electron Microscopy

SN   Signal to Noise

SPS   Suspension Plasma Spray

XRD   X-ray Diffraction

CHAPTER 1

INTRODUCTION

During the past century with the fast development of modern industries, increasing consumption of fossil fuels has raised concerns about depletion of conventional energy resources in addition to the greenhouse gas emissions and global warming. Extensive efforts have been carried out to acquire alternative green and renewable energy resources [1, 2]. According to Clean Energy Canada and Natural Resources Canada, Canada invested nearly $ 11 billion in clean energy in the year 2014, and currently 16.9% of the country's total primary supply is provided by the renewable energies, mainly wind, solar and hydro [3, 4]. However, these resources are intermittent and might not be available throughout the whole year in all geographic regions. In this regard, hydrogen as the most abundant element in the world has received wide attention [5, 6]. When used as a fuel, hydrogen does not have pollution problems like fossil fuels or intermittently availability problems like wind or solar energies [2, 6]. However, hydrogen cannot be used as a primary energy resource but as an energy carrier, since it does not naturally occur in its molecular form and it needs to be produced [6, 7]. The produced hydrogen can then be stored as a portable fuel, and converted and used later when the energy is needed with no emissions other than water vapour; for instance for electricity production by combustion engines, gas turbines and fuel cells [8].

Among different methods of hydrogen production such as steam reforming from hydrocarbons, thermolysis and electrolysis, alkaline water electrolysis is considered to be

1

one of the most promising technologies [1, 9]. This method offers the advantage of producing hydrogen with a purity of 99.8% and more [10]. In a water electrolysis process, water is decomposed into hydrogen and oxygen by passing a direct current through cathode and anode electrodes placed in a conductive electrolytic solution [11]. The benefit of using an alkaline solution is less corrosion of the cell components compared to the acidic ones [10]. The overall reaction of water electrolysis is given by Eq. 1.1. The reactions occur on cathode and anode electrodes are shown by Eq. 1.2 and Eq. 1.3, respectively. Figure 1.1 presents a schematic view of water electrolysis process.

$$H_2O = H_2 + \tfrac{1}{2}\, O_2 \hspace{6cm} \text{Eq. 1.1}$$

$$2H_2O + 2\, e^- = H_2 + 2\, OH^- \hspace{4.2cm} \text{Eq. 1.2}$$

$$2\, OH^- = \tfrac{1}{2}\, O_2 + H_2O + 2\, e^- \hspace{4.3cm} \text{Eq. 1.3}$$
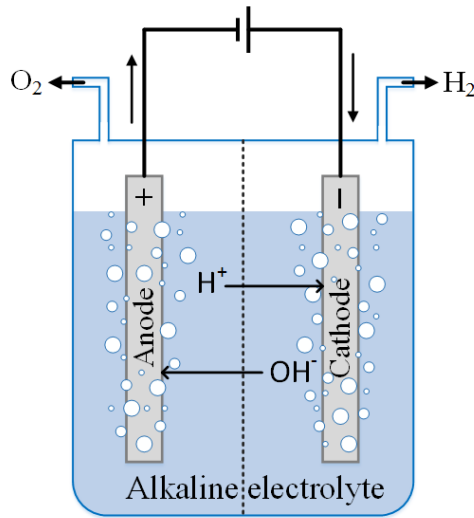
Figure 1.1- Schematic view of water electrolysis process.

To avoid the utilisation of fossil fuels to produce hydrogen, the electrical energy needed for splitting water into hydrogen and oxygen by electrolysis can be provided using different renewable resources, such as hydroelectricity, wind power or solar energy [7, 12]. Nonetheless, water electrolysis is still not used extensively for large scale hydrogen

production in industrial applications (it is used for only 4% of world hydrogen production). This low market is mainly associated with the high costs of the electrolysers besides excessive energy consumption of this process [13, 14]. Therefore, the main challenge for further improvements of the efficiency is to reduce the cost of the catalysts while minimizing the energy losses due to the hydrogen and oxygen evolution overpotentials. Design and fabrication of durable electrocatalysts with large active surface areas using inexpensive materials of high intrinsic catalytic activities are imperative in advancing the efficiency of this technology [13, 15, 16]. Some other factors that influence the process efficiency and need to be considered when designing the setup include operating temperature, type and concentration of the electrolyte, surface characteristics of the electrodes, and long-term stability of the electrodes [13].

1.1 Electrocatalytic activity

Hydrogen evolution reaction (HER) starts with the discharge of a water molecule (Volmer step, Eq. 1.4) followed by either electrochemical desorption (Heyrovsky step, Eq. 1.5), or chemical recombination (Tafel step, Eq. 1.6) depending on the hydrogen-metal bond strength [13, 17].

$$H_2O + e^- + M = M\text{-}H_{ads} + OH^- \qquad \text{Eq. 1.4}$$

$$M\text{-}H_{ads} + H_2O + e^- = H_2 + OH^- + M \qquad \text{Eq. 1.5}$$

$$2M\text{-}H_{ads} = H_2 + 2M \qquad \text{Eq. 1.6}$$

where M presents the metallic electrode and $M\text{-}H_{ads}$ shows the adsorbed hydrogen atom on the electrode surface.

Hydrogen evolution reaction is a function of several factors, including the rate of electron transfer from the surface of a metal to hydrogen ions. The rate of electron transfer depends on the electrode overpotential $,\eta$, which is the additional potential over the thermodynamic one that is required to overcome the reaction resistances [17].

$$\eta = E - E_0 \qquad \text{Eq. 1.7}$$

where E is the experimentally observed potential and E_0 is the thermodynamically determined potential. At high overpotentials, variation of the logarithm of current density (current per unit area), j, with potential becomes linear, and is shown by Tafel equation [13, 17].

$$\eta = a + b \, log \, j \qquad \text{Eq. 1.8}$$

a and b are known as Tafel constants, where

$$a = \frac{2.3 \, RT}{\alpha nF} \, log \, j_0 \qquad \text{Eq. 1.9}$$

is the Tafel intercept, and the Tafel slope is given by :

$$b = \frac{-2.3 \, RT}{\alpha nF} \qquad \text{Eq. 1.10}$$

In these equations, R is the universal gas constant, T the absolute temperature, α the electron transfer coefficient of the reaction, F the Faraday constant, and j_0 represents the exchange current density [17].

The exchange current density is defined as the rate of each cathodic or anodic reactions (equal and opposite) at equilibrium (η=0), and it is generally used as a measure for electrocatalytic activity. Using a steady-state polarization curve, the exchange current density can be derived from extrapolation of the linear part of the Tafel curve to the equilibrium potential as plotted in Figure 1.2 [17]. However, since the Tafel slope b could also be influenced by the intrinsic electrocatalytic activity and change of the electronic structure, using exchange current density to evaluate the catalytic activity might sometimes be misleading. Therefore, the value of overpotential at a specific high current density, generally 100, 250 or 500 mA/cm^2, is also used along with exchange current density to determine the electrocatalytic activity [13, 18].
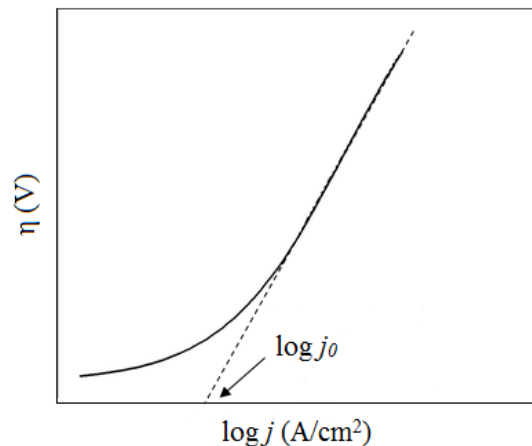
Figure 1.2- Exchange current density on a steady-state polarization curve.

1.1.1 Electrode materials and intrinsic activity

The electrocatalytic activity varies from metal to metal and depends on the bonding energy of hydrogen chemisorbed to the surface of that metal. The relation between the exchange current density, j_0, for the HER and $M\text{-}H_{ads}$ bond strength for various metals are illustrated by a volcano-shaped curve, shown in Figure 1.3 [19]. From this plot, it is seen that platinum has the highest exchange current density with an intermediate hydrogen-metal bonding energy. It is therefore the best-known electrocatalyst for the HER, and it has been widely studied as the cathode electrode material for the electrolysis process [19-21]. The intermediate bond strength favors both adsorption and desorption of hydrogen to/from the metal surface [21]. Nonetheless, platinum and other noble metals with high activities are rare and expensive, which has limited their commercial usage as electrode materials for water electrolysis. As an alternative, nickel has been widely investigated, since not only it is electrocatalytically active but also it has high stability in alkaline solutions. Besides this, nickel has much lower costs than the noble metals [22-26]. Practically, the lower electrocatalytic activity of nickel (compared to noble metals) can be compensated by increasing its intrinsic activity by obtaining nickel-based alloys, or by increasing its apparent activity by enhancing the surface area of the electrode [20, 21, 27-29].

5
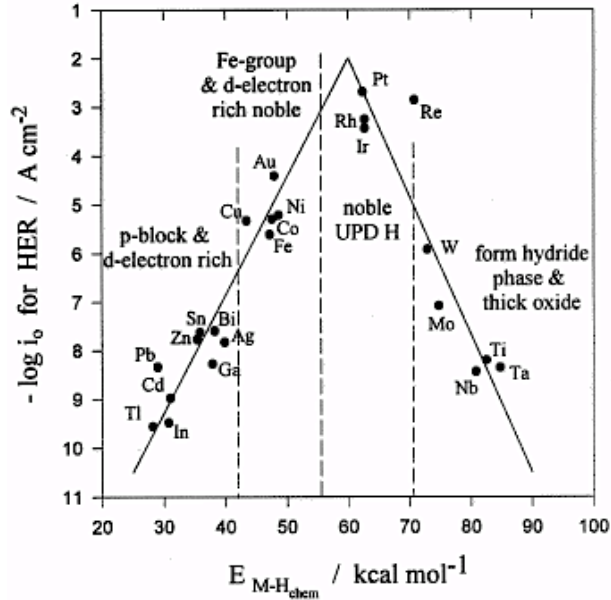
Figure 1.3- Volcano plot for log j_0 values for the
HER as a function of M-H bond energy [19].

It has been shown that alloying nickel with other transition metals (Fe, Mo, W, Ti, Zr, Co) results in an increased electrocatalytic activity of the electrode for the HER compared to pure nickel. Higher activities were obtained when nickel was combined with metals from the right side branch of the Volcano curve to obtain intermediate bond strengths [26, 30-33]. Among different investigated nickel-based alloys, nickel-molybdenum alloys are found to yield the highest electrocatalytic activities, and therefore, they have been studied extensively as cathode electrode material for alkaline water electrolysis [16, 26, 31-34]. Brown et al. [31] have reported superior performance of nickel-molybdenum electrodes compared to the other nickel-tungsten or nickel-vanadium ones. They showed that increasing the molybdenum content up to 30 at.% resulted in an overvoltage as low as -83 mV at 1 A/cm^2 and 70 °C. However, the activity started to diminish, when the molybdenum content was increased beyond a critical point [31]. The unfavorable effect of molybdenum addition higher than a certain level on the electrocatalytic activity was also reported by Birry et al. [26] and Chialvo et al. [34].

The increased catalytic activity of the nickel-molybdenum alloys could be related to the synergetic effect between the alloying elements, induced by the change of the electronic

density of the d-orbitals. Jaksic [35, 36] explained the synergism by the interaction of hypo-hyper-d-electronic components using Brewer-Engels theory. According to this theory, when transition metals with internally paired d-electrons are alloyed with transition metals with the empty or half-filled vacant d-orbitals, strong bonding is achieved by electron transfer from the former to vacant d-orbitals of the latter. As a result, stable intermetallic compounds with high electrocatalytic activities are obtained. Ezaki et al. [37] correlated the Fermi energy level to the hydrogen overpotentials in alloys. Therefore, for nickel-molybdenum alloys the enhanced electrocatalytic activity is expected to be associated with the increased Fermi energy, which facilitates the electron transfer from the metal surface to hydrogen ions and results in lower overpotentials [32]. However, the effect of synergism is still not well understood since the characterization and theoretical analysis is not sufficiently comprehensive yet [38]. Furthermore, addition of molybdenum is proven to enhance the long-term stability of the electrodes under continuous and intermittent electrolysis. It also affects the electrode microstructure by reducing the grain size, and thus, increasing the active surface area [26, 39, 40].

Besides alloying, microstructural properties and surface crystallography of an electrode also substantially influence the intrinsic electrocatalytic activity. Nanostructured electrodes have received much attention to be used for the HER since they significantly increase the electrocatalytic activity by enhancing the active surface area. Furthermore, they present a high volume fraction of surface defects, such as grain boundaries, dislocations, vacancies, etc. [41-43]. Therefore, they provide favourable electronic structures for the electrodes featured by large amounts of displaced atoms located at interfaces between adjacent grains. These surface defects and irregularities provide increased amount of interfaces for electrochemical reactions [41].

1.1.2   Electrode surface area and morphology

Electrode activity is characterized based on two types of geometric and real surface areas. The geometric surface area presents the projected surface of an electrode that was used for electrocatalytic measurements, whereas the real surface area includes all the surface that participated in the HER, i.e. the area added by the surface asperities. Accordingly, the terms

of apparent and intrinsic activities are applied when the geometric or real surface areas are used for the measurements, respectively.

A larger effective electrode surface adds to the reaction area by providing more electrode-electrolyte interface, reducing the operating current density, and contributing to a higher electrocatalytic activity [44-46]. The active area can be increased by enhancing the ratio between the real to geometric surface areas by increasing the electrode surface asperities, such as surface roughness and porosity. This objective can be achieved by several methods, some of which are provided below. The effect of the surface roughness on the electrocatalytic activity is well-documented in the literature [27, 29, 42, 47].

One of the mostly used methods to enhance the surface area is using Raney nickel as electrode material. Raney nickel is characterized by its large surface roughness, and it is considered to be an excellent electrocatalysts for the HER. Raney nickel activated electrodes are produced by leaching the aluminum or zinc content of the deposited precursor nickel-aluminum or nickel-zinc alloy with a caustic solution. Consequently, a very porous and coarse structured nickel residue is obtained, characterized by a high surface roughness factor [26, 40, 48]. Application of Raney nickel as an active electrocatalyst for the HER is widely reported in the literature [26, 30, 40, 49]. The superior electrochemical activity of Raney nickel is indeed a result of its large effective surface area and formation of active sites. However, it does not show long-term stability for the HER, especially in intermittent conditions due to dissolution of the un-leached active phases by the caustic electrolyte [2, 50, 51]. Therefore, more research is required to enhance the long-term performance of this catalyst. In addition, there are safety concerns with using Raney nickel as it has pyrophoric properties and it needs to be stored in an inert carrier, such as ethanol or water [52]. Moreover, long leaching times at elevated temperatures and additional rinsing steps are other drawbacks of using Raney nickel electrodes [53].

The surface area could also be increased by engineering the physical configuration and morphological modification of an electrode without addition of another material. For this purpose, it is common to modify the electrode surface by adding slits, fins or perforations with appropriate sizes that prevent entrapment of the hydrogen gas [11, 13, 54]. For a highly electrocatalytic active electrode, a large surface area with a good accessibility for diffusive mass transport of the reactants and their products within the

electrode structure is required [11, 13]. To maintain a high surface area during the electrolysis process, the electrode surface should be modified in such a way that facilitates the escape of the hydrogen gas bubbles from the surface, since the gas bubbles could be a major source of electrical resistances. Consequently, such electrode structure increases the surface available for the HER while reduces the reaction resistance and ohmic loss introduced by the bubbles [55]. In addition, electrode wettability also affects the bubble detachment from the surface and replacement of the bubbles by the electrolyte at the electrode/electrolyte interface [56, 57]. These physical surface properties, such as surface morphology and roughness, highly depend on the method used for preparation of the electrode.

1.1.3   Evaluation of the active electrode surface area

One of the key parameters to assess the performance of an electrode in terms of its intrinsic activity (independent of the effect of the added surface area) is to evaluate its real surface area. However, it is very difficult to determine the real surface area of an electrode, especially for nickel. In some studies, Brunauer-Emmett-Teller (BET) method, based on gas adsorption, has been used to evaluate the real surface area [58-60]. Nevertheless, it should be considered that the BET area does not necessarily correspond to the electrochemical active area as it measures the total surface area, including the area that may not contribute to the HER (presence of oxides, surface blockage by gas bubbles, etc.).

Another approach is to calculate the real surface area using electrochemical techniques. Several techniques have been proposed for this purpose [32, 61, 62]. Electrochemical impedance spectroscopy (EIS) is considered as one of the most appropriate methods for determination of the real surface area [62]. The data derived from the EIS measurements can be used to evaluate the electrochemical double layer capacitance (ECDLC), as explained in Chapter 5. The ECDLC forms at electrode/electrolyte interface, and it arises from charge accumulation in two layers when voltage is applied [11]. Figure 1.4 shows a schematic view of the double layer capacitance.

It is well-known that the ECDLC of an electrode is proportional to its real surface area [17, 48]. Hence, the surface area can be calculated having the surface roughness factor,

R_f, which can be evaluated using the ECDLC value. The roughness factor is the ratio between the double layer capacitances of the electrode and a smooth nickel surface with a capacitance value of 20 $\mu F\ cm^{-2}$ [17, 48]. Having the roughness factor, the real surface area then can be calculated using Eq. 1.11 [32].

$$A_{real} = R_f \times A_{geometric}$$
<div align="right">Eq. 1.11</div>
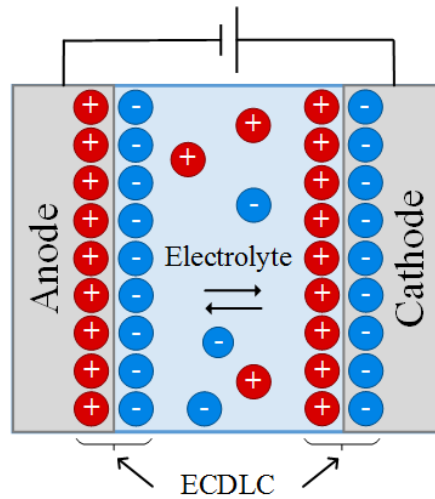
Figure 1.4- Schematic view of the double layer capacitances formed on the electrodes.

1.2 Processes for manufacturing electrodes

Conventional electrode production techniques to prepare nickel-based electrodes for the HER include electrodeposition [15, 28, 33, 62], thermal decomposition [31, 51, 63], electroless plating [59, 64, 65], pressing [66, 67], sintering [68-70], etc [34, 71]. Nonetheless, most of these processes exhibit considerable disadvantages, such as undesired decomposition reactions and phase transformations due to high temperatures and long processing times, low mechanical stability of the coatings due to limited coating thickness, and multi-step time consuming production processes.

Various thermal spraying techniques are expected to be promising for production of electrode coatings in cost effective processes with high deposition rates [39, 72, 73]. Thermal spray is a group of processes in which a heat source is used to melt feedstock materials (metallic or nonmetallic), generally in the form of powder, that is propelled at high velocities toward a substrate by a stream of gas or an atomization jet. The coatings are then formed by successive impact of the molten or semi-molten droplets on the surface of the substrate, followed by flattening, cooling and solidification. Different heat sources can be used to generate the thermal energy required for the spraying process, such as chemical combustion or electrical methods [74-76]. Figure 1.5 shows a schematic overview of the thermal spray process.
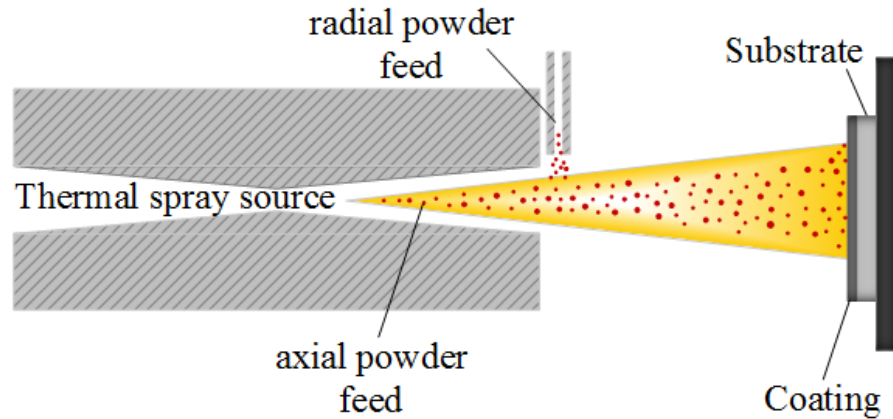
Figure 1.5- Schematic view of a thermal spray process. The powder feeding could be conducted by either radial or axial injection.

Using thermal spraying, the surface morphology, microstructure and porosity of the coatings can be controlled by selection of the spraying parameters [77-79]. A large variety of materials can be sprayed to manufacture electrode coatings needing no or only a slight post-processing or heat treatment. Different thermal spraying techniques include plasma spray, wire arc spray, flame spray, high velocity oxy-fuel (HVOF), and cold spray. Figure 1.6 compares the temperature and velocity ranges of the particles for these thermal spraying processes. In addition, a brief explanation of each process that was used for production of the electrodes in the literature and in this research is provided below.

11
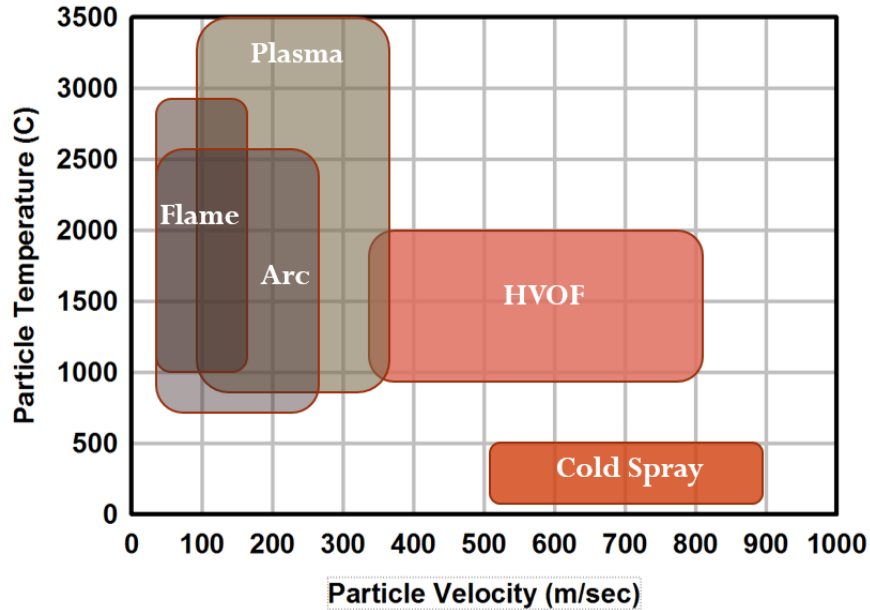
Figure 1.6- Gas temperature and particle velocity for thermal spray processes. The data is adopted from Reference [80].

1.2.1 Wire arc spray

Wire arc spray, commercially introduced in the early 1960s, is a thermal spray method, which is particularly used for high deposition rates. In this process, an electric arc is generated between two consumable wire electrodes that meet when continuously fed into the gun and are connected to a direct current power source. Subsequently, the tips of the wires melt by the arc, and then atomize into fine droplets and accelerate toward a substrate by compressed air. Thereafter, the coatings are formed by impact, deformation and solidification of the molten particles on the surface of the substrate. Figure 1.7 shows a schematic view of this process. Wire arc spray offers a considerable higher thermal efficiency compared to other thermal spray techniques due to the direct melting of the wires by the arc. In addition, the substrate heating is also minimized in this method as no flame or hot gas jet is used. To reduce the level of oxidation of the inflight droplets, high atomizing air flow and short spray distances are used [74, 76].
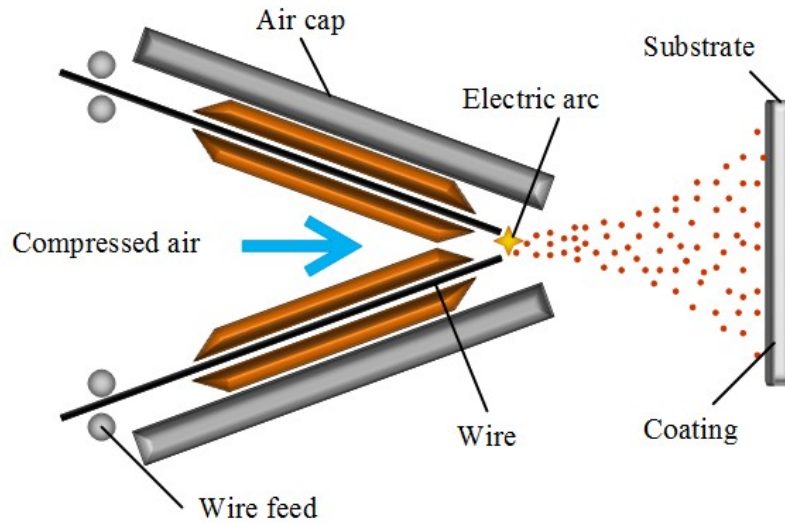
Figure 1.7- Schematic view of a wire arc spray process.

1.2.2 Plasma spray

1.2.2.1 Atmospheric plasma spray

In an atmospheric plasma spray (APS), the plasma plume is generated by ionization of a jet of argon or nitrogen as the primary gas mixed with hydrogen or helium as the secondary gas by a strong electric arc between a tungsten cathode and a copper anode. Powder particles with the typically average particle size of 10-100 μm are then introduced into the high velocity, high temperature plasma jet by a carrier gas (usually argon) and melt. Consequently, coatings are formed by acceleration, impact, flattening and deposition of molten particles on the surface of a substrate [74, 81]. The input power is controlled by the gases that were used to generate the plasma as well as the applied current. As the flame temperature reaches as high as 15,000 °C, a wide variety of coating materials, including metals, ceramic and composites, can be used as the starting powder. However, since the coatings are usually sprayed in atmospheric environment, some oxidation of the molten metal particles is expected [74]. A schematic view of this process is shown in Figure 4.2.

1.2.2.2   Suspension plasma spray

In recent years, there has been a major interest in producing plasma sprayed coatings, utilizing nanosized powder particles. This interest arouse from the unique properties and superior performances of nanostructured coatings [42, 82]. However, nanosized particles cannot be used directly in plasma spray due to their low flowability and injection difficulties they cause in the spraying system. Suspension plasma spray (SPS), an alternative to conventional plasma spray techniques, was first invented in the mid-1990s in the University of Sherbrooke, Canada [83]. In SPS process, the same atmospheric plasma spray system described in section 1.2.1.1 is employed, only a fluid is used as the powder carrier instead of a gas. The liquid suspension is basically made of mixing the feedstock powder particles, with particle sizes ranging from tens of nanometers to a few micrometers, and a liquid phase, which is mostly ethanol, water or a mixture of both. Nevertheless, sub-micron sized particles have the tendency to agglomerate and sediment, even when stirring the suspension. To overcome this problem, an appropriate dispersant needs to be added to the solution [84].

In a SPS process, the suspension is injected into the plasma jet and undergoes fragmentation of the liquid stream into droplets. The liquid phase is then evaporated, and the accelerated particles partially or fully melt depending on their residence time within the plasma flow. Finally, a deposition is formed on a substrate as described for APS [84, 85]. In SPS, the spraying distances are rather short, between 4 and 6 cm, since smaller particles decelerate faster and undergo extremely rapid heating and cooling rates [78, 84]. In this process, suspension viscosity and particle load into the plasma jet are amongst the main factors that control the morphology of the coatings [84, 86]. A schematic view of a SPS process in illustrated in Chapter 3 (Figure 3.1).

1.2.3   High velocity oxy-fuel

High velocity oxy-fuel (HVOF), commercially introduced at the beginning of 1980s, is a thermal spray process that allows deposition of surface coatings with a low-oxide content at higher particle velocities and relatively lower temperatures compared to plasma spray

[74, 76, 77]. In a HVOF process, a mixture of the fuel gas or fuel liquid (hydrogen, propylene, propane, acetylene, kerosene, etc.) and oxygen is introduced into a combustion chamber, ignited and combusted. Subsequently, the exhausted gas accelerates in a converging-diverging nozzle before it emerges into the atmosphere at supersonic velocities. The expansion of the high velocity flow (500 to 1200 m/s) at the exit of the nozzle results in formation of shock diamonds. The gas velocity is determined by the pressure in the combustion chamber (typically 0.3 to 1 MPa) [74, 76]. The powder feedstock, normally in the range of 5 to 45 μm, may be injected radially or axially into the gas by nitrogen or argon as the carrier gas [76]. The coating is then formed by acceleration, melting, impact and deposition of the melted or partially melted particles on a substrate. The resulting coatings show high densities and a very well adhesion due to the high particle velocities [74, 76]. A schematic of a typical HVOF system is provided in Chapter 5 (Figure 5.2).

1.2.4   Cold spray

Cold spray, invented in the mid-1980s, is a thermal spray technique in which the coatings are formed by deposition of solid-state particles [87, 88]. In a cold spray process, a preheated compressed gas (generally nitrogen, air, or helium) accelerates through a converging-diverging nozzle to develop a supersonic flow. The gas temperature substantially reduces at the nozzle exit. Subsequently, the injected solid powder particles in the range of 1 to 50 μm impact on a substrate at high velocities and at temperatures near room temperature, well below their melting point. To form a coating, the velocity of the particles needs to be higher than a so-called critical velocity (which depends on the particle and substrate materials) upon impact [74, 88-92]. Consequently, the impinging particles experience plastic deformation and shear instability at the interface and form a coating with a good bond and cohesion strength [75, 87, 93, 94]. High quality coatings can be obtained by using this method, which are characterized by high deposition efficiency, high coating density, improved adhesion and a low level of oxides. Low oxidation levels are related to the low operating temperature of the cold spray process due to the rapid decrease of the gas

temperature upon acceleration [74, 89, 95]. A schematic view of a cold spray system is shown in Figure 6.1.

1.3 Thermal spray for electrode fabrication

In 1977 Coker et al. [96] proposed coating ferrous electrodes by different types of metal powders using flame spraying and plasma spraying to reduce the hydrogen production overvoltage in chlor-alkali cells. They related the improved electrocatalytic activities to the increased surface area of the electrodes and efficient release of hydrogen bubbles due to produced surface roughness by the spraying process. Since then, several studies have been conducted on using different thermal spraying techniques for development of nickel-based electrode coatings for the HER, a summary of which is provided in Table 1.1.

In most of these studies, the main focus was on increasing the intrinsic activity and the real surface area of the electrodes by producing coatings of Raney nickel, nickel-molybdenum and Raney nickel-molybdenum alloys [26, 39, 40, 72, 97]. Nonetheless, the effect of the spray parameters, spray conditions and surface modifications on the activities of the electrodes was not addressed in detail. In addition, mainly plasma spray methods, specifically in controlled environments, were used for producing the cathode electrode coatings rather than other thermal spraying techniques [26, 39, 40]. This interest towards using plasma spray could be related to its maturity and wide application in various fields [74]. Using thermal spray to deposit electrode coatings started as early as 1970s, when HVOF and cold spray were not commercially developed yet [74, 96]. In addition, higher temperature and lower velocity of plasma spray compared to other spraying techniques such as HVOF and cold spray, allows deposition of a larger variety of materials to develop coatings with higher porosity (Figure 1.6).

Moreover, application of Raney nickel as the electrode material (Table 1.1) requires using high concentrations of hazardous caustic solutions for the leaching process at high temperatures besides additional rinsing steps and producing more waste [26, 39, 40, 72, 97]. In addition, in some of these studies the electrolysis process was conducted at elevated temperatures to increase the electrolyte conductivity and promote bubble detachment from the surface [39, 40, 98]. However, increased cell temperatures results in higher operating

costs correlated with the electricity consumption, and it also reduces the lifetime of the cell components due to a more corrosive operating environment. The issue associated with the gas bubble resistances could be resolved by modification and engineering of the electrode surface profiles by optimization of the coating processes which has not been comprehensively addressed in the literature. Therefore, due to the aforementioned gaps and issues of the previous studies further research and development efforts are required to advance the production of the electrodes by thermal spraying processes for the HER.

Table 1.1- Summary of the research conducted on using thermal spraying techniques to produce electrode coatings for the HER.

Author	Year	Material	Coating process	Electrolyte	Cell temperature (°C)	η (mV)	j_0 (A/cm^2)
Hall [98]	1983	Ni	Atmospheric plasma spray	30% KOH	80	η_{200} = 108	2×10^{-4}
Schiller et al. [39]	1995	Ni-Al	Vacuum plasma spray	25% KOH	70	η_{1000} = 120	-
Miousse et al. [40]	1995	Ni-Al-Mo	Low pressure plasma spray	1M NaOH	70	η_{250} = 148	2.0×10^{-3}
Fournier et al. [97]	1999	Ni-Al	Wire arc spray	1M NaOH	25	η_{250} = 179	2.7×10^{-4}
Birry et al. [26]	2004	Ni-Al	Vacuum plasma spray	1M KOH	25	η_{250} = 170	1.7×10^{-2}
		Ni-Al-Mo	Vacuum plasma spray	1M KOH	25	η_{250} = 67	2.7×10^{-1}
Kellenberger et al. [73]	2007	Ni	Wire arc spray	1M NaOH	25	-	3.7×10^{-4}
		Ni-Ti	Wire arc Spray	1M NaOH	25	-	5.3×10^{-3}
Chade et al. [72]	2013	Ni-Al	Atmospheric plasma spray	30% KOH	30	η_{300} = 91	1.8×10^{-2}

1.4 Objectives

This study is a novel multidisciplinary research covering materials, mechanical and electrochemical engineering to design, manufacture and characterize cathode electrodes for the HER. The final objective of this work is to improve the energy efficiency of the alkaline water electrolysis process for hydrogen production using thermal spraying for manufacturing nickel cathode electrodes. While most of the previous works in this field focused on increasing the catalytic activity by using nickel alloys, in this research the effect of spraying conditions along with the developed coating microstructures and morphologies on electrode activities are studied, independent of using any specific alloying elements. The main objectives of this research study are summarized as follows:

- To investigate the capability of using suspension plasma spray, high velocity oxy-fuel and cold spray as novel methods for producing highly active nickel-based cathode electrodes
  - $\rightarrow$ Reducing the oxidation issues associated with using atmospheric plasma spray by using other thermal spray methods that require lower spraying temperatures, i.e. HVOF and cold spray

- To investigate the effect of spraying parameters on the morphology, microstructure and electrochemical performance of the manufactured electrodes

- To improve the intrinsic activity of the electrodes by changing the electronic structure and introducing surface defects to the electrodes to act as active sites for the HER

- To increase the apparent electrocatalytic activity by enhancing the real surface area of the electrodes.
  - $\rightarrow$ Developing multiscale surface structures composed of micron and nanosized features, where nanosized structure provides the enhanced surface area while the micronsized features facilitate hydrogen bubble departure from the surface

→ Engineering 3-dimesional surface textures composed of various levels of macro- and microscopic features

1.5 Thesis organization

This thesis is divided into seven chapters. The first chapter provides a brief introduction about hydrogen production by alkaline water electrolysis, including the important parameters that affect the electrocatalytic activity of an electrode. A short description of the thermal spray processes along with a general literature review of their applications in producing electrodes for alkaline water electrolysis is also given in this chapter. Finally, the objectives of the thesis are presented.

Chapter 2 presents atmospheric and suspension plasma spraying as two promising methods for producing cathode electrode coatings with large active surface areas. This chapter focuses on optimization of the spray parameters for maximizing the electrode surface area, using Taguchi method for design of experiments. The optimum conditions for preparation of a stable suspension to be used in the SPS process are also discussed.

Chapter 3 introduces the combination of the two atmospheric and suspension plasma spray techniques as an original method to develop high performance electrodes composed of a multiscale micro/nanosized surface structure, using the results obtained from the previous chapter. It also includes optimization of the number of passes used for depositing suspension plasma spray coatings to maximize the efficiency of the hydrogen evolution reaction. Furthermore, the effect of wettability and microstructure on the electrocatalytic activity of the electrodes is studied.

Chapter 4 takes a further step towards increasing the electrocatalytic activity of the electrodes by engineering their surfaces. For this purpose, deposition of three-dimensional fin arrays on the electrodes surfaces by spraying through mesh screens, using the combined atmospheric and suspension plasma spraying is proposed. This novel methodology contributes to the development of electrode coatings with various roughness levels from macro- to nanosized, which also facilitates the escape of hydrogen gas bubbles from the surface. In addition, the effect of the surface area added by the macroscopic and

microscopic surface features on the electrocatalytic activity of the electrodes is investigated.

In Chapter 5, high velocity oxy-fuel is introduced as a novel method for producing nickel-based coatings for alkaline water electrolysis. The spray parameters are selected based on deposition of mostly solid-state particles on the surface of the electrodes in order to reduce the oxidation of the coatings. Using the same methodology as Chapter 4, the surface texture of the electrodes is engineered by deposition of pyramidal fin arrays using mesh screen masks. Various surface microstructures and roughness levels were obtained on the electrodes due to the normal and off-normal deposition of the particles, and their effect on the electrocatalytic performance of the electrodes is studied.

Chapter 6 includes a fundamental study of using cold spray as a novel method for preparation of the electrocatalysts for hydrogen evolution by deposition of solid-state particles. The influence of cold spraying parameters and peening of the surface by the spraying particles on the surface morphology and microstructure of the developed coatings is studied. Furthermore, the electrochemical performances of the electrodes including both apparent and intrinsic activities are evaluated thoroughly, using both steady-state polarization curves and electrochemical impedance spectroscopy methods. Finally, the effect of the electrodes surface topography, microstructure, residual stress and surface strain on the obtained electrocatalytic activities are discussed.

Chapter 7 summarizes the conclusions and contributions of this research, and provides a list of recommendations for the future work.

CHAPTER 2

ARTICLE 1: Electrocatalytically Active Nickel-Based Electrode Coatings Formed by Atmospheric and Suspension Plasma Spraying

M. Aghasibeig, M. Mousavi[1], F. Ben Ettouil[2], C. Moreau, R. Wuthrich, A. Dolatabadi

Department of Mechanical and Industrial Engineering, Concordia University
Montreal, QC H3G 1M8, Canada

Abstract

Ni-based electrode coatings with enhanced surface areas, for hydrogen production, were developed using atmospheric plasma spray (APS) and suspension plasma spray (SPS) processes. The results revealed a larger electrochemical active surface area for the coatings produced by SPS compared to those produced by APS process. SEM micrographs showed

---

[1] Mr. M. Mousavi assisted with suspension preparation for the SPS process.

[2] Dr. F. Ben Ettouil assisted with design and development of the injection setup for the SPS process.

that the surface microstructure of the sample with the largest surface area was composed of a large number of small cauliflower-like aggregates with an average diameter of 10 μm.

2.1 Introduction

During the past century with the fast development of modern industries, increase of the environmental pollution and high costs of the fossil fuels has raised the demand of acquiring alternative resources of energy. Extensive efforts have been carried out to obtain new renewable energy resources at lower prices compared to the conventional fuels, and to reduce the damaging effects of climate change by mitigating greenhouse gas emissions [2, 99]. Hydrogen is considered to be a promising clean energy carrier to replace fossil derivative fuels. One of the most promising techniques for producing high purity hydrogen is alkaline water electrolysis, giving the advantage of a more controllable corrosion rate and cheaper construction materials [7]. However, costs of the electrolysis process have been a great concern since it is highly dependent on the costs of the electrical energy [2, 100]. Therefore, to improve the energy efficiency of the electrolysis process, hydrogen evolution over-potentials that contribute significantly to cell energy losses should be lowered. To achieve this goal, advanced electrolysers with high performance electrodes need to be developed to obtain hydrogen at diminishing costs with minimum energy consumption [15]. Using high intrinsic active electrode materials with enhanced electrode surface areas is a possible route of increasing the efficiency of the hydrogen evolution reaction (HER) [26, 101]. A good accessibility for diffusive mass transport of the reactants and their products inside the porous structure is another requirement for the electrodes for HER [102].

Although platinum is the best-known electrocatalyst for HER, its commercial use as cathode electrode material has been limited due to its expensiveness and rarity. In industrial applications, often nickel replaces platinum, since not only it is a catalytically active metal but also it has high stability in alkaline solutions at elevated temperatures [39]. Among

different surface modification techniques, plasma spraying has demonstrated its capability to produce porous electrode coatings in a cost effective process, taking advantage of the surface morphology produced by the spraying process [39, 98, 101]. Possibility of forming coatings at high deposition rates with moderate operating costs has made this method superior compared to other surface coating techniques, such as electrodeposition, sintering, vacuum deposition and etc [103]. Reduction of hydrogen evolution overpotentials when using plasma sprayed nickel-based cathode electrodes has been addressed in several works [39, 97, 98].

In recent years, there has been a major interest towards development of plasma sprayed coatings, utilizing nanosized particles. This interest arouse from the unique features of nanometer scale coatings, such as increased surface areas and superior performances. For Ti-based electrodes, Irissou et al. [104] showed that the hydrogen evolution overpotentials of nanostructured electrodes were significantly lower compared to the ones prepared by the micron-sized powder. However, nanosized particles cannot be used directly for plasma spraying due to the difficulties with their injection into the core of the plasma jet. Suspension plasma spray (SPS), based on injection of a liquid feedstock, is a novel method developed to overcome the injection problem of sub-micron and nanosized particles. The suspension is basically made by dispersing the feedstock powder particles with the particle sizes ranging from tens of nanometers to a few micrometers in a liquid phase, which is mostly ethanol, water or a mixture of both. Addition of a dispersant is usually needed to reduce the agglomeration and sedimentation of the particles [105, 106].

The objective of this work was to develop Ni-based electrode coatings with enhanced surface areas for the hydrogen evolution reaction, using atmospheric plasma spray (APS) and SPS processes. The effects of spraying parameters of each process on the electrochemical active surface areas of the coated samples were studied. The results were compared for the coatings produced by APS and SPS processes.

2.2 Material and methods

2.2.1 Spraying materials

Two different commercial powders, nickel with the nominal particle size in the range of -75 to +45 µm and nickel oxide with the nominal particle size in the range of -5 µm to +500 nm, were used for APS and SPS processes, respectively. Nickel powder has a tendency to sediment and agglomerate in the suspension because of its high specific mass and magnetic properties [107]. Due to the difficulties in obtaining a stable nickel suspension, nickel oxide powder was used instead. A series of stable suspensions containing 10 wt.% of NiO powder in ethanol as the solvent were prepared for the SPS process. To increase time-stability of the particle dispersion and to prevent agglomeration of the particles, polyvinylpyrrolidone (PVP) was added as the dispersing agent. 1, 2, 3, 4 and 5 wt.% of PVP were added to the suspension at different test tubes to adjust its mass percentage by sedimentation tests.

2.2.2 Injection setup

The injection system for SPS was composed of two tanks, one containing the suspension and the other one containing ethanol. For the spraying process, the tanks were pressurized with N_2 gas. To avoid contamination and clogging of the injection system, the ethanol stored in the tank was used to clean the injection system after each suspension projection. The position of the injector, having a 200-µm diameter nozzle, was adjusted in such a way that the suspension drops penetrate adequately to the plasma jet at the nozzle exit [108].

2.2.3 Spraying processes

Plasma spraying experiments were carried out using a Sulzer Metco 3MB atmospheric plasma-spraying gun, mounted on a computer-controlled robotic arm. Coatings were deposited on grit blasted, rectangular low carbon steel coupons of dimensions $25 \times 25 \times 3$ mm^3. Argon was used as the primary plasma gas as well as the powder carrier gas, and hydrogen was used as the secondary gas.

To determine optimum operating conditions for producing coatings with a high surface area, while having a minimum number of experimental runs, Taguchi statistical method [109] was employed in design of the experiments (DOE). Using such an approach greatly reduce the experimental time and cost. DOE is further useful in evaluation of the importance of each selected coating variable on the surface areas of the coatings.

Table 2.1 shows the L_9 orthogonal array designed for APS processes. The table was produced using a combination of standoff distance, current, plasma gas flow rate, and torch traverse speed as spraying variables, each with three selected levels (two levels for the torch traverse speed). The 15 over-layers were deposited at a constant powder feeding rate of 30 g/min to create APS coating. Table 2.2 shows the L_8 orthogonal array used for SPS processes. The array consists of a combination of five variables including standoff distance, suspension flow rate, plasma gas flow rate, current and torch traverse speed, each having two selected levels. Each SPS coating was composed of deposition of 20 over-layers.

Table 2.1- Plasma spraying parameters used for APS coatings.

Run order	Standoff Distance (cm)	Current (A)	Plasma gas flow (Ar/H$_2$) (NLPM)	Torch traverse speed (m/s)
A1	12	400	35/2.2	0.5
A2	12	450	35/4.4	1
A3	12	500	35/6.6	1
A4	17	400	35/4.4	0.5
A5	17	450	35/6.6	0.5
A6	17	500	35/2.2	1
A7	22	400	35/6.6	1
A8	22	450	35/2.2	0.5
A9	22	500	35/4.4	0.5

Table 2.2- Plasma spraying parameters used for SPS coatings.

Run order	Standoff distance (cm)	Suspension flow rate (g/min)	Plasma gas flow (Ar/H$_2$) (NLPM)	Current (A)	Torch traverse speed (m/s)
S1	4	31.2	50/5	500	0.5
S2	4	31.2	50/5	450	1
S3	4	22.8	50/3	500	0.5
S4	4	22.8	50/3	450	1
S5	6	31.2	50/3	500	1
S6	6	31.2	50/3	450	0.5
S7	6	22.8	50/5	500	1
S8	6	22.8	50/5	450	0.5

2.2.4 Characterization and analysis

One of the key parameters to assess the performance of an electrode is its electrochemical active surface area. It is well known that the electrochemical double layer capacitance (ECDLC) of an electrode is proportional to the electrochemical active surface area of the material used (typically 20 μF/cm^2) [17]. Therefore, for initial comparison of the electrochemical active surface area of the coatings formed by APS and SPS processes, their ECDLC were measured. A three-electrode configuration was used for all measurements. A Pt wire and an Hg/HgO electrode (saturated 1M KOH) were used as counter and reference electrodes in a 0.5 M NaOH solution. A geometrical surface area of 0.78 cm^2 of each coating was exposed to the electrolyte as the working electrode. The cell was bubbled with nitrogen before and during the measurements to de-oxygenate the electrolyte solution.

Cyclic voltammetry measurements were performed at five scan rates of 0.02, 0.05, 0.1, 0.15, and 0.2 V/s in the potential window from -1.35 to 0.7 V vs. Hg/HgO using an in-house potentiostat. The region around -0.1 to 0.4 V vs. Hg/HgO is considered to be essentially free of faradic current and was used to evaluate the contribution of the ECDLC to the recorded current (Figure 2.1). Three ECDLC measurements were performed on each

sample. The capacitance values were calculated by dividing the average current at the center of the positive and negative sweeps of the resulting cyclic voltammograms by the scan rates [17].
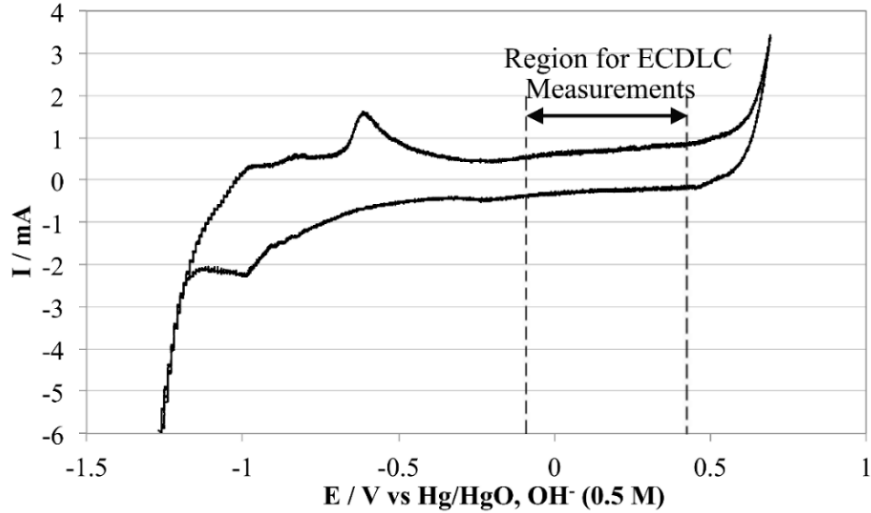
Figure 2.1- Cyclic voltammetry of S6 sample, and non-faradic region used for ECDLC measurements between the dashed lines (scan rate of 0.02 V/s).

Signal-to-noise (*S/N*) ratio, a measure of robustness, was used to analyze the influence of each spraying control factor on the specific surface area of the coatings. Since the goal was to maximize the specific surface area, the *S/N* ratio of "larger is better" was used. This category is calculated as a logarithmic transformation of loss function:

$$S/N = (-10 \times log \sum \frac{1}{Y^2} /n)$$

<div align="right">Eq. 2.1</div>

Where n is the number of observations, and Y is the observed data.
Morphology of powder particles and coating surfaces were studied by a Hitachi S-3400N VP scanning electron microscope (SEM).

2.3 Results and discussion

2.3.1 Precursor materials

Figure 2.2 shows SEM images of the morphology of precursor micron-sized Ni and submicron-sized NiO powders used in this study. Sedimentation results of the suspensions are depicted in Figure 2.3. It can be seen that the minimum sedimentation was obtained for the suspension containing 1 wt.% PVP. The viscosity of this suspension was measured by a Cannon-Fenske reverse flow capillary viscometer with an error margin of $\pm0.38\%$. Kinematic viscosity of the suspension was measured 1.69×10^{-6} m^2/s at 22 ºC, showing a 15.6% increase with respect to the viscosity of ethanol.
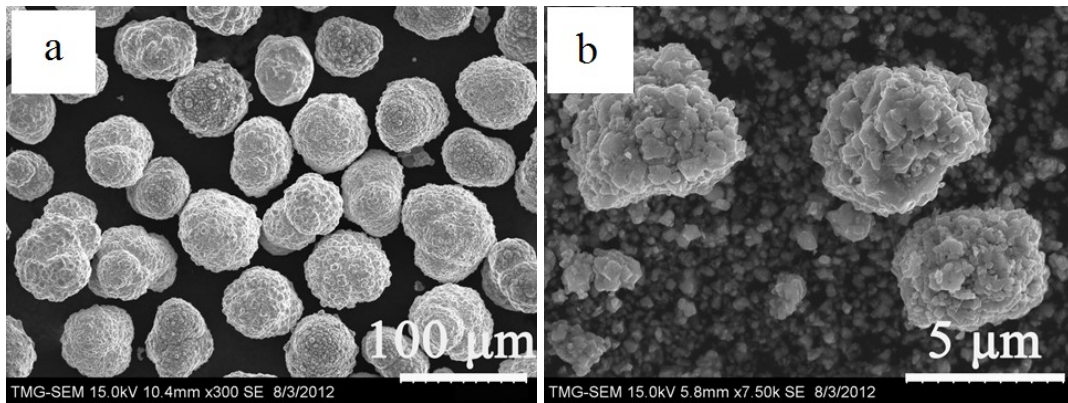
Figure 2.2- Morphology of precursor powders: (a) Ni powder and (b) NiO powder.
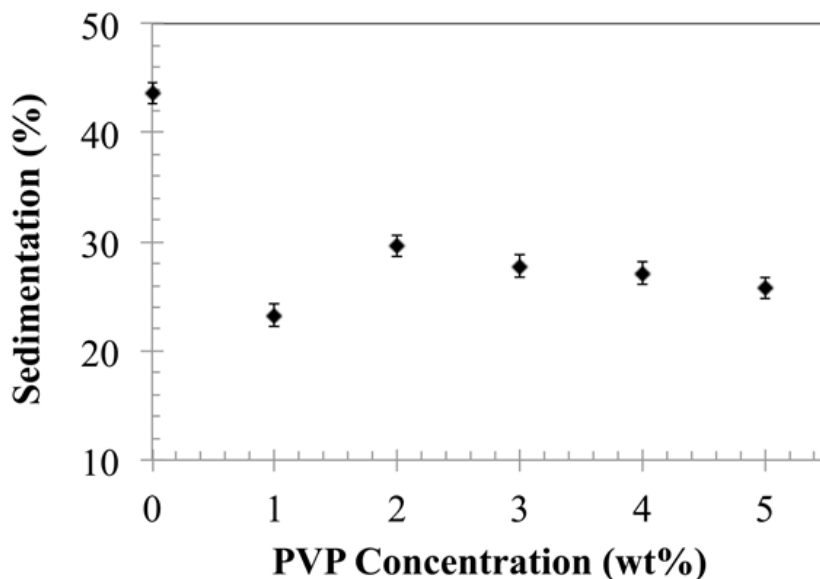
Figure 2.3- Sedimentation test results for 10 wt.% NiO suspension and
0 to 5 wt.% PVP after 14 days. The error bars show the error margin
of the viscometer ($\pm$0.38%).

2.3.2 ECDLC measurements

Figure 2.4 shows the calculated double layer capacitances for all APS and SPS samples. As illustrated in this figure, by coating the sample using either APS or SPS, the ECDLC values are increased significantly compared to the uncoated substrate. Nevertheless, the samples coated with the suspension exhibited a larger ECDLC compared to the APS deposited ones. As indicated above, the double layer capacitance of a sample is in a direct relation with its electrochemical active surface area. Therefore, it can be concluded that the coatings produced by nanosized powder have a larger electrochemical active surface area in comparison with those produced by micron-sized powder. Smaller standard deviation of ECDLC values of APS-coated samples indicate more homogeneous coatings compared to the SPS-coated ones. On the other hand, larger variation of ECDLC between SPS coatings indicate that the SPS process is more sensitive to the spraying parameters, i.e., a small variation of the spraying parameters can greatly affect the surface area of the

coatings. This can be mainly related to the much smaller powder particles used in the SPS process.
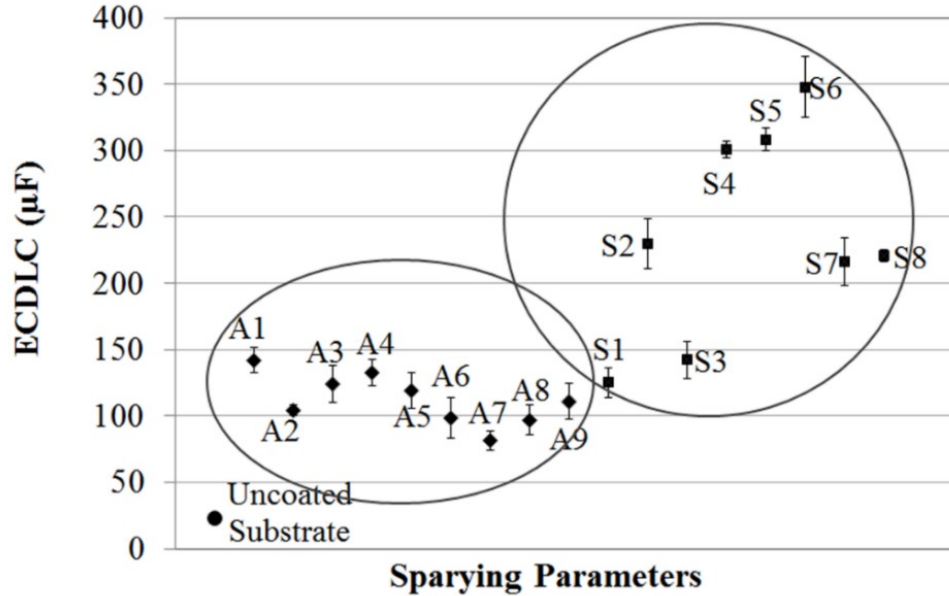
Figure 2.4- Electric double layer capacitance of APS- and SPS-coated samples, evaluated from three measurements on each sample and the error bars show the standard deviations.

2.3.3 APS coatings

ECDLC results, illustrated in Figure 2.4, indicate that A7 with 82 µF has the lowest and A1 with approximately 142 µF has the highest capacitance among APS-coated samples. Surface SEM micrographs of these two samples can be seen in Figure 2.5. The images show that the top surface of A7 coating is composed of larger splats with diameters of >100 µm, while A1 has a finer and rougher surface structure. The presence of semi-molten and re-solidified particles is evident in the latter coating. Plasma sprayed coatings are formed by deposition of flattened splats created by impact and rapid solidification of molten and semi molten particles. The size, morphology, and bonding of the splats along with porosity determine the structural properties of that deposit. The different surface structures can be directly related to the plasma spraying parameters that were used to form the coatings [81].

Table 2.3 presents the *S/N* response data for the electric double layer capacitance. Based on the value differences between the larger and smaller levels, the relative importance of each factor is quantified as factor ranks. The results indicate that standoff distance has the greatest influence on the electro-active surface area, followed by torch traverse speed, current and hydrogen gas flow.
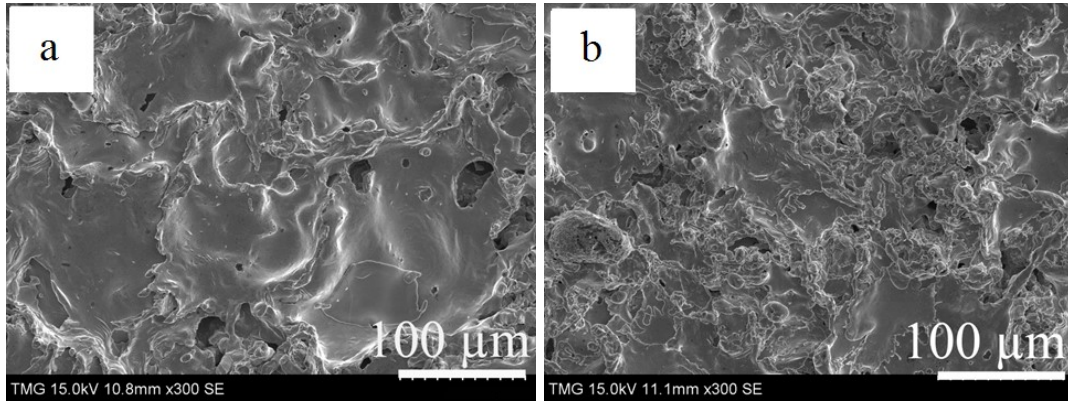
Figure 2.5- SEM surface images of APS samples (a) A7 and (b) A1.

Table 2.3- Response table for Signal to Noise Ratios for APS.

Level	Standoff distance	Current	Hydrogen gas flow	Torch traverse speed
1	42.27	42.16	41.81	42.39
2	42.36	41.58	42.16	41.24
3	41.00	41.90	41.66	-
Delta	1.36	0.59	0.50	1.15
Rank	1	3	4	2

Figure 2.6 shows the effect of each control factor level on the active surface area. At 12 cm standoff distance, higher velocity and temperature of the impacting particles provide a better cohesion between the depositing layer and the substrate. Meanwhile, the smaller particles have a tendency to re-solidify because of the more rapid heat loss and deceleration at longer inflight paths. This combination of completely melted, semi-melted and re-solidified particles leads to the formation of deposits with a higher degree of porosity,

rougher surfaces, and consequently larger surface areas. Increasing the standoff distance from 12 to 17 cm did not have any significant effect on the electrochemical active surface area of the coatings. By further increase of the standoff distance to 22 cm, the particle velocity and temperature are further reduced at the time of impact to the substrate. Therefore, more inflight particles at longer spray distances are re-solidified, which also causes a weaker adhesion of the particles to the substrate. In this case, only a limited number of particles, which are still molten and semi-molten by the time of impact, would adhere to the substrate and fabricate coatings consisting of larger splats with lower open porosity, and thus, a more limited specific surface area. For a better understanding of the behavior of inflight particles, their temperature and velocity at the point of impact need to be determined using a DPV-2000 on-line diagnostic system.
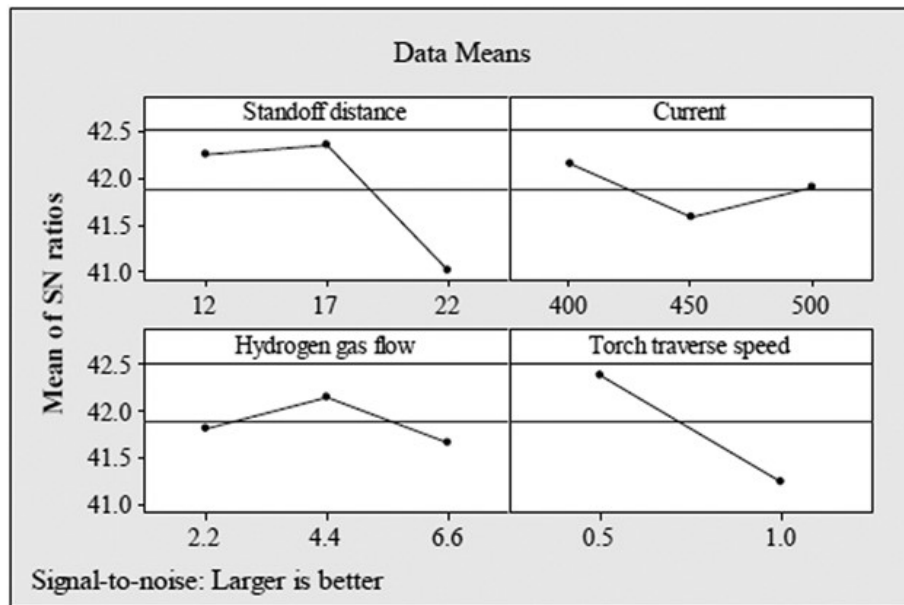
Figure 2.6- Main effects plot for S/N ratios for APS.

The second parameter that affected the active surface area is torch traverse speed. The results indicate that by increasing the torch traverse speed from 0.5 m/s to 1m/s, the active surface area was reduced. There is no clear explanation for this behavior, and further investigations are required. The results in Figure 2.6 and Table 2.3 show that the current and hydrogen gas flow did not have a significant effect on the electrochemical active

33

surface area. Since the goal here is to maximize the specific surface area, the factor levels that produce the highest mean should be employed. Analysis of the results leads to the conclusion that a factor combination of 17 cm standoff distance, 400 A current, 4.4 NLPM hydrogen flow, and 0.5 m/s gun travel speed generates the maximum surface area. For this combination, an *S/N* ratio of 43.13 was predicted. However, further experiments are required to confirm its accuracy.

2.3.4 SPS coatings

Figure 2.4 shows that S1 with 125 µF and S6 with 348 µF has the smallest and the largest capacitance for SPS coatings, respectively. SEM images of these two surfaces are shown in Figure 2.7.
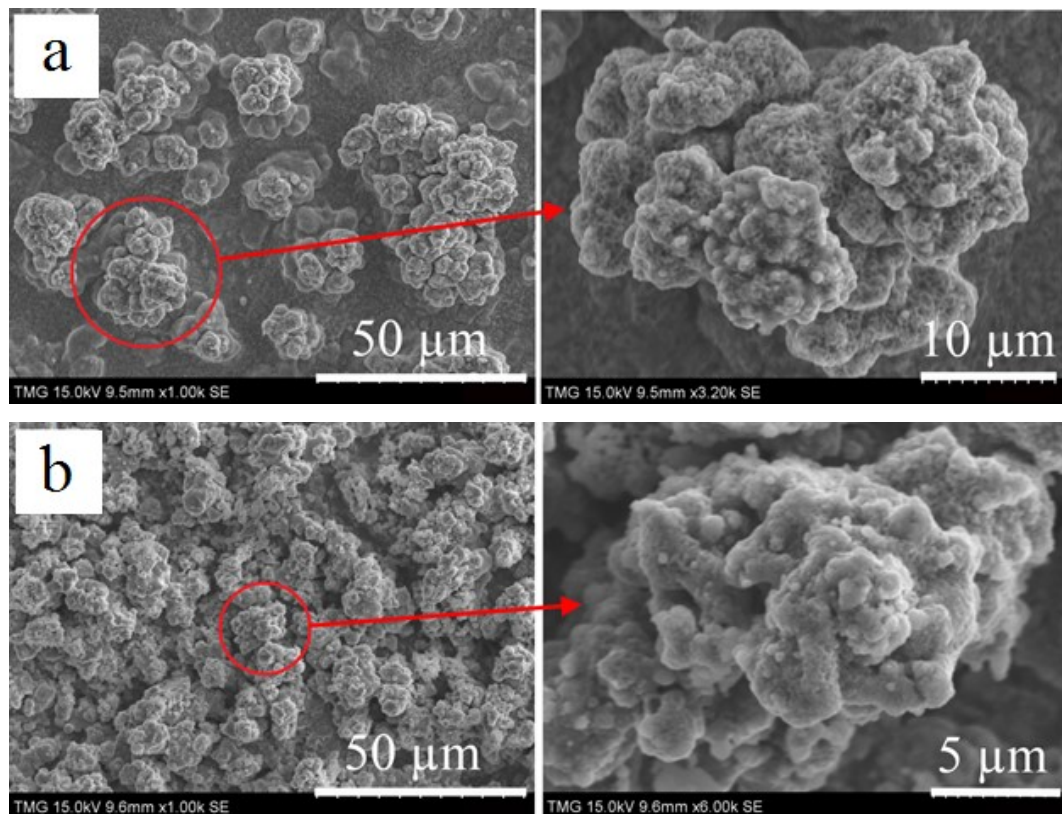
Figure 2.7- SEM surface images of SPS samples: (a) S1 and (b) S6.

As illustrated in Figure 2.7, the surface of S1 coating is mainly composed of dispersed cauliflower-like aggregates with diameters larger than 20 μm, and the coating does not cover the whole substrate. For S6 coating, larger amounts of smaller aggregates (~ 10 μm) are deposited on the surface and form a rougher surface with more specific surface area. Formation of cauliflower-like microstructures using SPS process is widely reported in the literature [110-112].

Table 2.4 shows that the significance of the spraying variables for SPS coatings from high to low are current, standoff distance, hydrogen gas flow, torch traverse speed, and suspension flow rate. Figure 2.8 depicts the effect of various factor levels on the produced surface areas. The influence of spraying variables on the specific surface areas of the SPS coatings can be discussed as follows.

Table 2.4- Response table for Signal to Noise Ratios for SPS.

Level	Standoff distance	Suspension flow rate	Hydrogen gas flow	Current	Torch traverse speed
1	46.16	48.04	49.01	49.12	46.24
2	49.04	47.15	46.20	46.07	48.95
Delta	2.88	0.89	2.81	3.05	2.72
Rank	2	5	3	1	4
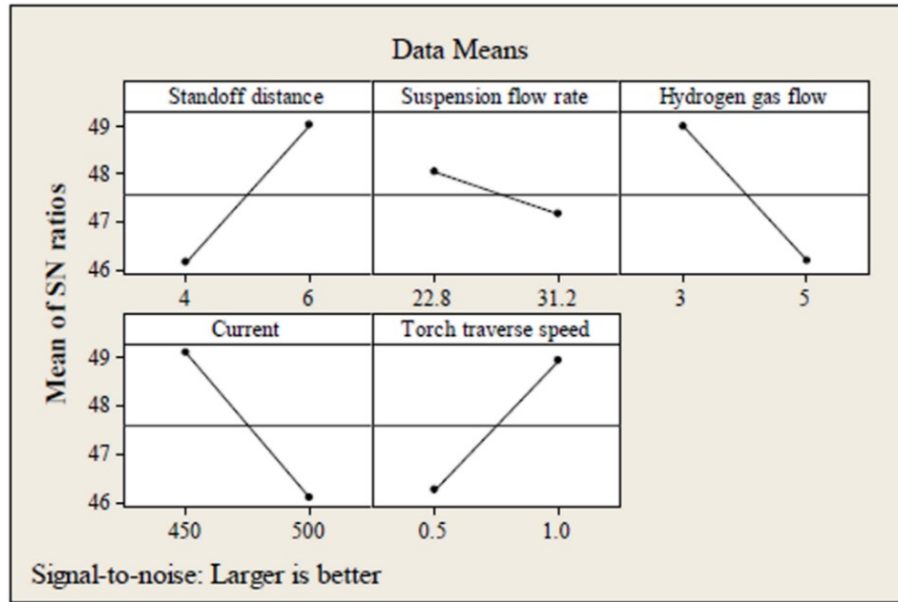
Figure 2.8- Main effects plot for S/N ratios for SPS.

By increasing the spray distance from 4 to 6 cm, the electrochemical active surface area is increased. This effect can be described by formation of more porous structures due to the deposition of cooler and slower particles at higher spraying distances. The effect of current and hydrogen gas flow can be attributed to their influence on the input power. Higher current and hydrogen gas flow rate result in an elevated input power. For the SPS experiments input power was varied from 22 kW at the hydrogen flow rate of 3 NLPM and current of 450 A to 28 kW at the hydrogen flow rate of 5 NLPM and current of 500 A. It has been shown that higher power levels result in an increasing temperature and velocity of the sprayed particles in addition to the higher temperature of the top surface of the coating [113], which cause higher expansion of the impinging particles on the surface, densification of coating, and thus, a smaller surface area.

The results of Figure 2.8 and Table 2.4 show that the torch traverse speed had a slightly lower effect on the active surface area compared to the spray distance and input power, and suspension flow rate did not have a significant effect on the surface area. The results indicate that the real surface is maximized at 6 cm standoff distance, 22.8 g/min of suspension flow rate, 3 NLPM hydrogen gas flow, 450 A current and 1 m/s torch traverse speed. Using a combination of these factor levels, an *S/N* ratio of 53.76 is predicted.

2.4 Conclusions

APS and SPS coating processes were used to produce nickel-based electrode coatings with enhanced surface areas for hydrogen production. Electrocatalytically active electrodes with large surface areas can significantly reduce the costs of electrolysis and increase the efficiency of the process. Taguchi method of DOE was used to define the optimum spraying conditions. Electric double layer capacitances of the coatings were determined as measures for their electrochemical active surface areas. The results showed higher surface areas for all SPS deposits compared to the APS ones. This can be attributed to the formation of very fine porous agglomerates with an average diameter of 10 µm on the surface of the SPS coatings. ECDLC was increased by a factor of 7 for the APS and by a factor of 17 for the SPS-coated samples with the largest surface areas compared to the sandblasted substrate. The effects of spraying variables of each process on the specific surface areas of the coatings were studied. By analysis of the results, the standoff distance in APS and current in SPS were identified as the most significant factors affecting the electrochemical active surface areas of the coatings. Generally, generation of larger surface areas was related to the deposition of semi-molten and re-solidified particles and formation of more porous structures. For further increase of the electrochemical active surface area of APS and SPS deposits, more optimization of coating parameters is required. In addition, both APS- and SPS-coated samples need to be reduced to resume the activity of the electrodes.

CHAPTER 3

ARTICLE 2: Fabrication of Nickel Electrode Coatings by Combined Atmospheric and Suspension Plasma Spray Processes

Maniya Aghasibeig, Christian Moreau, Ali Dolatabadi, Rolf Wuthrich

Department of Mechanical and Industrial Engineering, Concordia University
Montreal, QC H3G 1M8, Canada

Abstract

Atmospheric plasma spray and suspension plasma spray were presented as two promising methods for manufacturing nickel cathode electrode coatings for alkaline water electrolysis, using micron and submicron-sized powders, respectively. A combination of both processes was also successfully utilized as a novel method by deposition of a suspension plasma sprayed layer on an atmospheric plasma sprayed one to develop high performance electrodes. The coated electrodes were then characterized in terms of their microstructure, surface topography, wettability and steady state polarization curves. The highest electrocatalytic activity was obtained for an electrode coated by the combined method with the exchange current density and overpotential (η_{250}) values of 6.2×10^{-4} A/cm^2

and -386 mV, respectively. The increased activity of this electrode was attributed to its large specific surface area with a high surface roughness value (S_a = 14.4 μm) comprising a multiscale micron/submicron-sized surface structure. It is expected that the dual microstructure of this electrode in addition to its superhydrophilic behaviour (with contact angles below 10°) enhances the activity by providing more reaction sites for hydrogen adsorption, promoting the diffusive mass transport of the reactants, and facilitating hydrogen bubble ascension from the pores.

3.1 Introduction

In recent years, production of high purity hydrogen by alkaline water electrolysis as a clean energy carrier has gained significant attention due to the increasingly damaging effects of the greenhouse gas emissions and environmental pollution [1]. However, high electricity consumption of the electrolysis process has made this method costly for large scale hydrogen production, and therefore, its efficiency needs to be increased by reducing the hydrogen production overpotentials [13, 14]. For this purpose, two methods have been proposed including manufacturing electrodes using intrinsic active materials and enhancing the electrode active surface area [13, 114, 115]. Nickel is widely used as the electrode material for the hydrogen evolution reaction (HER), because it has relatively high catalytic activity and is inexpensive compared to noble metals such as platinum [21, 116].

Among various electrode production techniques, plasma spray has demonstrated its capability to manufacture nickel based electrode coatings with large surface areas and high roughness values [26, 40, 47, 117-119]. In atmospheric plasma spray (APS), the plasma plume is generated by ionization of a jet of argon or nitrogen as the primary gas mixed with hydrogen or helium as the secondary gas by a strong electric arc generated between the cathode and the anode. Micron size particles with an average particle size of 10 to 100 μm are introduced into the high velocity, high temperature plasma jet. Subsequently, coatings

are generated by acceleration, impact, flattering and deposition of molten and semi molten particles on the surface of a substrate [81].

It has been shown that manufacturing electrodes with nanostructured surfaces significantly enhances their electrocatalytic activity, which could be related to their unique electronic properties and presence of a large density of surface defects, such as grain boundaries [42, 120]. However, submicron and nanosized particles cannot be used directly in plasma spraying due to their low flowability and injection difficulties they cause in the spraying system. Suspension plasma spray (SPS), invented in the mid-1990s in the University of Sherbrooke, Canada, is an alternative to the conventional plasma spray for injection of submicron and nanosized particles using a liquid feedstock [121]. In a SPS process, the suspension undergoes fragmentation and vaporization of the droplets after its injection into the plasma jet (Figure 3.1). The particles are then accelerated, partially or fully melted depending on their residence time within the plasma flow and form a coating upon impact on the substrate [84, 85]. Since smaller particles decelerate faster and undergo extremely rapid heating and cooling rates, the spraying distances are usually shorter in SPS (4 to 6 cm) compared to APS (8 to 12 cm) [84].
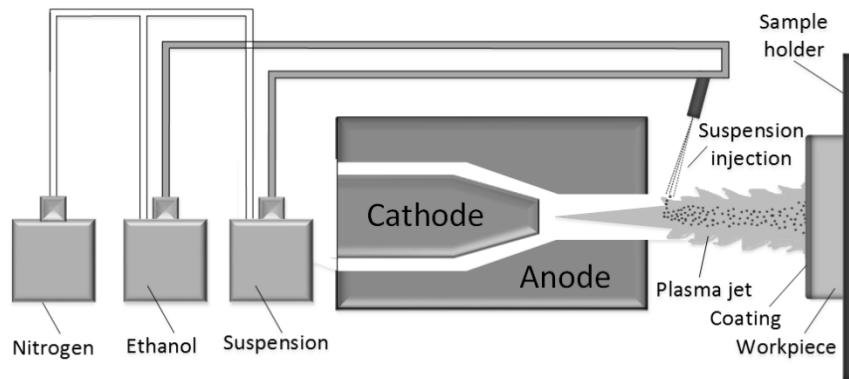
Figure 3.1- Schematic view of the SPS process.

It is worth noting that a fraction of the inner surface of the coatings that could be efficiently used for hydrogen production could easily get blocked by the hydrogen bubbles at very small pore sizes of the developed coating. This could consequently reduce the electrocatalytic activity by imposing additional electrical resistances and ohmic losses, and

thus, decrease the rate of the HER [122, 123]. Therefore, controlling the size of the pores is one of the most important parameters that should be considered during deposition of the nanostructured coatings.

Preliminary results on combining the APS and SPS methods for manufacturing electrodes with hybrid micron and submicron-sized surface structures were reported by the authors recently [119]. In the current study, further optimization of the HER efficiency was carried out by investigating the influence of the number of the passes deposited by SPS on top of the APS coated electrodes. Such unique microstructures and surface morphologies developed by the combined APS-SPS method are expected to provide enhanced electrode surface areas, and overcome the hydrogen bubble blockage problem within the pores. Electrocatalytic activity of the produced electrodes was determined for the HER, and it was compared to the activities of those electrodes produced by solely APS and SPS coating processes.

3.2   Material and methods

3.2.1   Materials and spray conditions

The starting powders used to deposit the electrode coatings included nickel Metco 56C-NS (Oerlikon Metco, USA), and nickel oxide FCM NiO-F (fuelcellmaterials.com, USA) for APS and SPS coating processes, respectively. Figure 3.2 shows the particle morphology of both powders.

Particle size distribution of both powders was determined by a laser diffraction particle size analyser (Malvern Instruments Ltd., England) using a 300 mm lens. The results, illustrated in Figure 3.3, show a distribution width of 45 to 90 μm for the micron sized nickel powder and from100 nm to 11 μm for the submicron sized nickel oxide powder. The distribution widths of D10, D50, and D90 were measured to be 60, 69, and 78 μm for nickel and 0.20, 0.73 and 4 μm for nickel oxide powders, respectively.
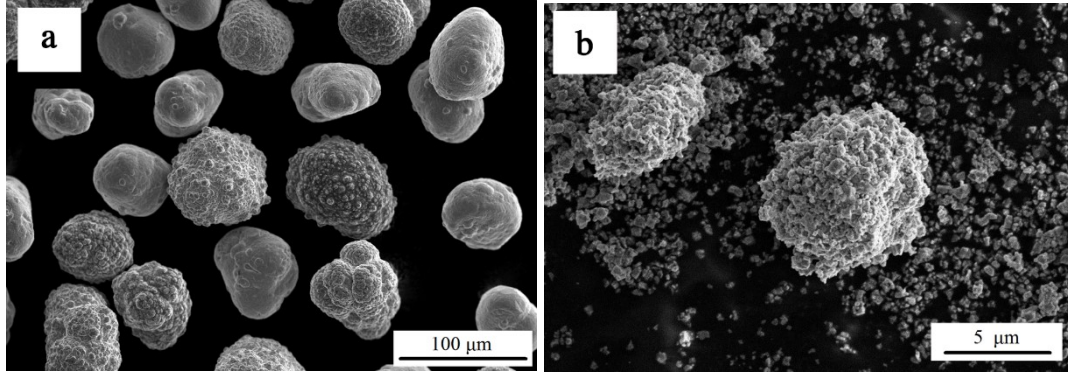
Figure 3.2- SEM morphology of the precursor powders, (a) nickel and (b) nickel oxide.
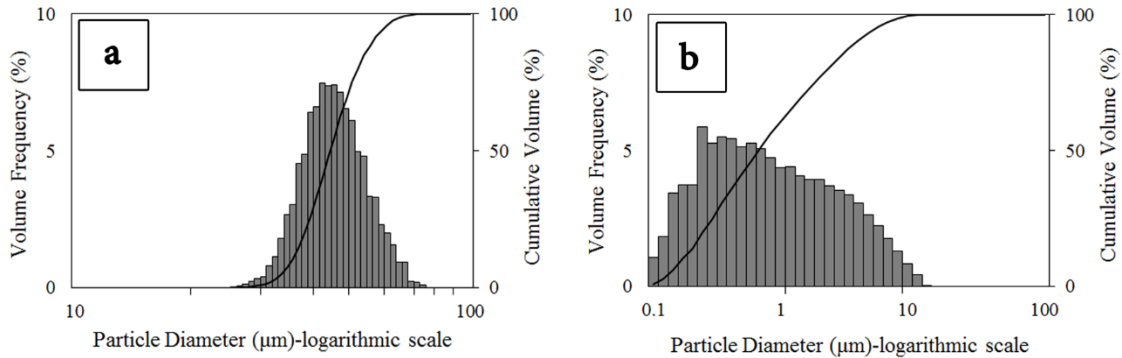
Figure 3.3- Histograms showing the particle size distributions for the (a) nickel and (b) nickel oxide powders.

Suspensions for the SPS were prepared by mixing of 10 wt.% of nickel oxide powder with 1 wt.% of polyvinylpyrrolidone (PVP) as dispersing agent in ethanol. The injection setup for the SPS process was developed in-house and described in detail in a previous work [118]. A 200 μm internal diameter tube was used to radially inject the suspension into the plasma jet.

All coatings were deposited using a 40 kW Sulzer Metco 3MB atmospheric plasma spray gun mounted on a six-axis robotic arm. Argon and hydrogen were used as the primary and the secondary plasma gases, respectively, whereas nitrogen was used as the carrier gas for injecting dry powders in APS. The depositions were carried out onto rectangular Inconel 600 coupons with a surface area of 645 mm^2.

Atmospheric and suspension plasma sprayed electrodes were prepared by deposition of 8 and 25 passes on the substrate coupons, respectively. To take advantage of a multiscale surface structure, three additional electrodes were prepared by suspension plasma spraying of thin layer coatings on top of the APS deposited electrodes. To determine the optimum number of the passes required to deposit by SPS for maximizing the efficiency of the HER, 3, 6 and 10 passes were deposited by SPS. For simplicity, these three electrodes were named S3, S6 and S10, respectively, throughout this paper. The plasma spraying parameters used for deposition of APS and SPS coated electrodes, listed in Table 3.1, were selected based on the methodology reported previously [118, 119]. The parameters were obtained by optimization of the processes towards maximizing the surface area of the coatings while having a good adhesion to the substrate.

Table 3.1- Spraying parameters used in APS and SPS processes.

Process	Standoff distance (mm)	Feeding rate (g/min)	Plasma gas flow (Ar/H$_2$) (SLPM)	Torch traverse speed (m/s)	Current (A)
APS	80	15 (powder)	60/2	0.5	500
SPS	60	31 (suspension)	50/3	0.5	450

3.2.2 Characterization of the electrodes

Temperature and velocity of the inflight particles were measured for the APS process at the standoff distance using a DPV eVOLUTION system (Tecnar Automation Ltd., Canada). DPV eVOLUTION system is an online diagnostic system for online monitoring of the inflight particle characteristics based on their thermal radiation emission. However, due to the small size of the particles in a liquid medium in SPS, this system cannot be used for velocity and temperature measurements. A FLIR A320 infrared camera (FLIR Systems Inc., USA) was used for monitoring the temperature of the substrates during the APS coating process.

All coatings were reduced as Ni particles were partially oxidized during spraying at high temperatures in atmospheric environment during APS, and nickel oxide powder was used as the starting material in SPS. The reduction of nickel oxide coatings to nickel was conducted in 100 vol.% hydrogen in a tube furnace at 650 °C for 1 hour, with 2 °C/min heating and cooling rates.

To prepare polished cross-sections of the as-sprayed specimens, coated samples were cut using a precision cut-off machine (Secotom-15, Struers A/S, Denmark), and then mounted and polished by standard metallographic procedures to a final finish of 0.05 μm. A scanning electron microscope (SEM) (S-3400N, Hitachi High Technologies America, Inc., USA) operating at 15 kV was used to study the specimen cross-sections, morphology of starting powders and top surfaces of the coated electrodes. Three dimensional surface topography, roughness and surface ratio of the electrodes were determined using a 3D Confocal Laser Scanning Microscope (CLSM) (LEXT-OLS4000, Olympus Corporation, Japan) with a resolution of 10 nm in the z direction and 120 nm in the xy plane. The surface ratio indicates the ratio between the specific and the projected surface areas. To study the mass transport within the produced coatings and the effect of surface coverage by the gas bubbles on catalyst activities, wettability of the coatings was determined [56, 57]. The contact angle of 10 μL water droplets on electrode surfaces were measured using a backlit imaging setup after the electrodes were cleaned ultrasonically in acetone. A code developed by Stalder et al. [124] as a plugin to ImageJ [125] software was used to make the image analysis and contact angle measurements.

Electrochemical measurements were conducted using a conventional three electrode setup and a SRS potentiostat (EC301, Stanford Research Systems, Inc., USA). No forced flow was applied. The coated samples were used as the working electrode, a platinum wire as the counter electrode and an Hg/HgO electrode saturated in 1 M KOH (-0.924 V vs. Hg/HgO) as the reference electrode in a 1 M NaOH electrolytic solution. The electrolyte was bubbled with nitrogen gas during the measurements to deoxygenate the solution. Prior to each measurement, the working electrode was pre-polarized for 1800 s at -1.6 V vs. Hg/HgO to remove the surface nickel oxides present on the coatings. Steady-state polarization curves were recorded in the current range of 10 μA to 1 A at room temperature.

The electrocatalytic activity of the electrodes was evaluated from extrapolation of the linear part of the Tafel curves to the equilibrium potential.

3.3   Results and discussion

3.3.1   Morphological studies

3.3.1.1   APS coated electrode

Figure 3.4a and b shows the top surface SEM micrograph and backscattered electron (BSE) cross-sectional image of the reduced APS coated electrode. The cross-sectional image of the coating before reduction is shown in Figure 4c. The surface structure is comprised of 10 to 50 μm fragmented splats and resolidified particles. The cross-sectional image shows an approximate coating thickness of 100 μm with a good bonding to the substrate. The micrographs display a porous microstructure with high surface roughness. Before reduction, interlamellar cracks can be mainly observed in the cross-sectional image (Figure 4c). However, the intersplat bonding was improved by healing of some of the microcracks, whereas dispersed globular pores were formed (Figure 4b) by reduction of nickel oxide formed at high spraying temperatures to nickel in the hydrogen-rich reduction furnace. In addition, formation of a porous microstructure could also be related to the spraying conditions.

It has been shown that the substrate temperature besides the temperature and velocity of the inflight particles at the point of impact substantially control the coating formation and microstructure during the plasma spraying process [126, 127]. For the APS coated electrode, the substrate's temperature was measured in the range of 90 to 150 $^{\circ}$C. At this relatively low substrate temperature, the amount of gas entrapped underneath splats was increased favouring formation of interlamellar pores and splashing of the melted droplets [128, 129].
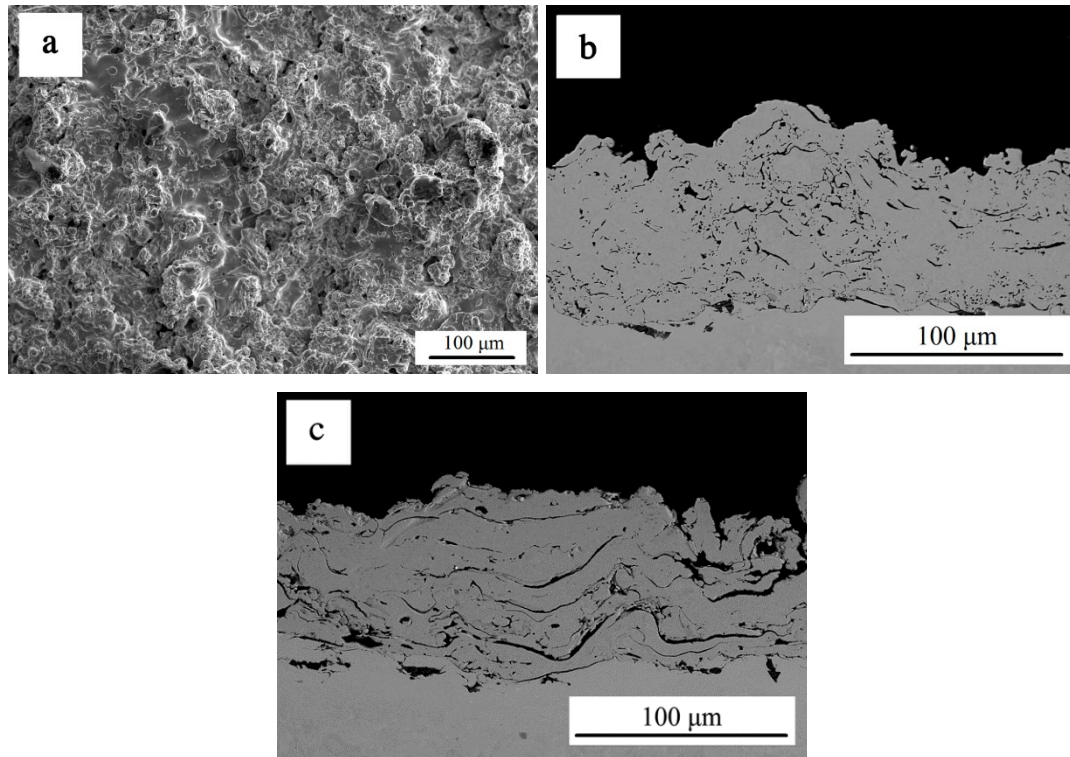
Figure 3.4- Micrographs of the APS coated electrode, (a) SEM of the top surface after reduction, (b) BSE of the cross-section after reduction, and (c) BSE of the cross-section before reduction.

The temperature and velocity of the spray particles at the substrate standoff distance were measured at 2126±213 °C (SD) and 101±31 m/s (SD), respectively. At this temperature, it is expected that the nickel particles were fully melted upon impact to the substrate (nickel melting point: 1453 °C). Splashing of the impinging molten particles upon high velocity impact on the substrate and their break down into smaller droplets could also be responsible for the formation of splash splats, resolidified structure and the high surface roughness.

3.3.1.2   SPS coated electrode

Figure 3.5a and b shows the top surface and cross-section SEM images of the reduced SPS coated electrode. The cross-section of this electrode before reduction is shown in Figure

5c. The coating exhibits a fine microstructure composed of cauliflower-like clusters with sizes of few tens of micrometres. The cross-sectional image exhibits a highly porous and rough coating with a nonuniform thickness of approximately 10 to 40 µm. Formation of this coating structure could be associated with different factors.
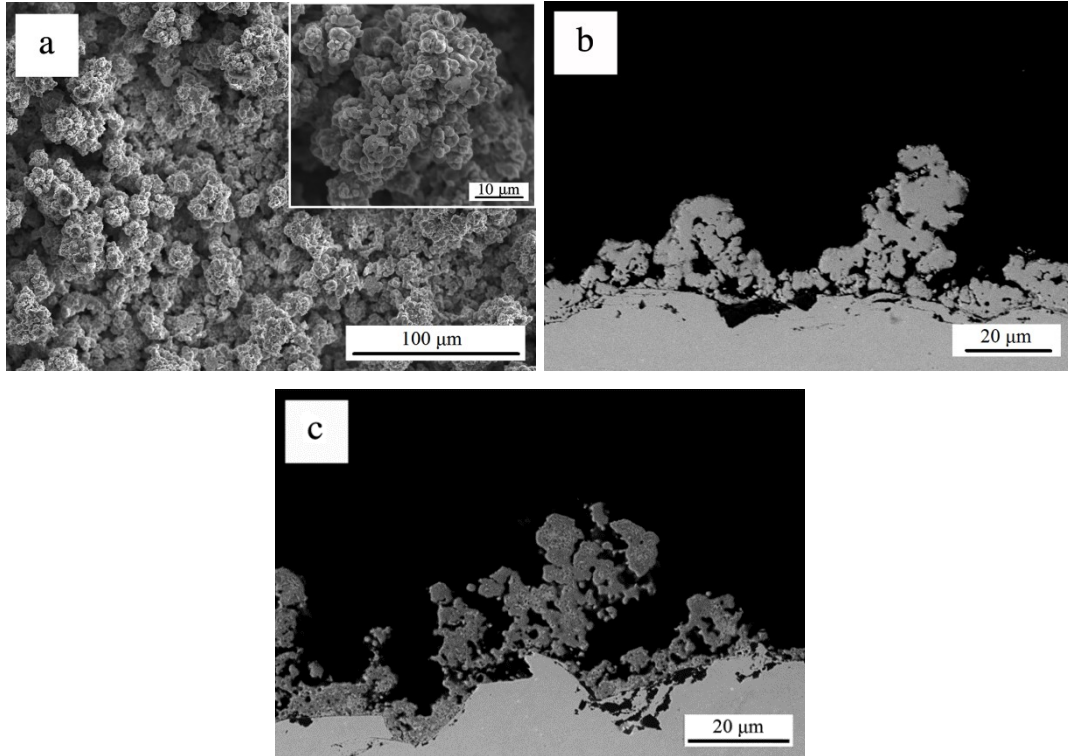
Figure 3.5- SEM micrographs of the SPS coated electrode, (a) reduced top surface, (b) reduced cross-section, and (c) unreduced cross-section. The inset shows a zoomed in view.

One factor could be the presence of untreated or poorly treated particles due to improper penetration of the suspension into the hot plasma jet, which affected the degree of the particles melting and the level of porosity in the deposit. As a wide particle size distribution (Figure 3.3-b) was used to prepare the suspensions, the smaller particles from the tail of the distribution could not penetrate into the core of the plasma jet. Therefore, these particles could not fully melt as they passed through the plasma jet fringes with lower temperatures. On the other hand, larger agglomerated particles also could not get fully melted under the selected spraying parameters, leading to a porous coating structure. It

was shown by Fauchais et al. [107] that high instabilities and voltage fluctuations of the plasma jet (especially for argon and hydrogen plasma) in SPS impedes homogenous processing of the suspension. These fluctuations are also responsible for random particle trajectories, and therefore, their nonuniform penetration, fragmentation and melting at different zones of the flame. In addition, similar to the APS coatings, reduction of the oxides could also add to the coating porosity.

The nonuniform thickness and high porosity of this coating could also be explained by the formation of a strong stagnation flow on the substrate. The smaller droplets with lower momentum deviate from the spray direction and move laterally along the substrate when they reach this boundary layer. Consequently, the deflected droplets impact on the sides of the surface asperities, which eventually yielded the creation of a porous coating featuring a higher thickness on the surface bumps [130, 131]. In addition, the relatively large standoff distance (60 mm) could also favour formation of the rough and porous coating microstructure. It is expected for the particles to have a lower temperature and velocity at the point of impact at larger spraying distances. Therefore, the lower temperature could result in deposition of a larger number of resolidified particles, where the lower velocity could cause higher deflection of the particles due to the stagnation flow.

3.3.1.3   Combined APS-SPS coated electrodes

Figure 3.6a to c illustrates top surface SEM images of the electrodes S3, S6 and S10 after reduction, and Figure 6d shows the top surface image of electrode S10 before reduction. The BSE cross-sectional micrographs of the last 50 μm near the top surface of each coating, where the SPS layers were deposited, are also provided in the images. In all three coatings the combined spraying technique resulted in the development of unique microstructures, comprised of submicron-sized particles deposited by SPS on the top surface of the coatings with micron sized features fabricated by APS. As shown in the cross-sectional images, the SPS layers are well bonded to the beneath APS deposits in all coatings. Increase of the electrode porosity due to the reduction of the oxides can be clearly seen by comparison between the cross-sectional images in Figures 6c and d. Electrodes S6 and S10 exhibit almost similar top surface morphologies consisting of the cauliflower-like features on top

of the existing surface protrusions. However, for electrode S3 with a smaller number of SPS passes, the dominant microstructure is the one fabricated by APS.
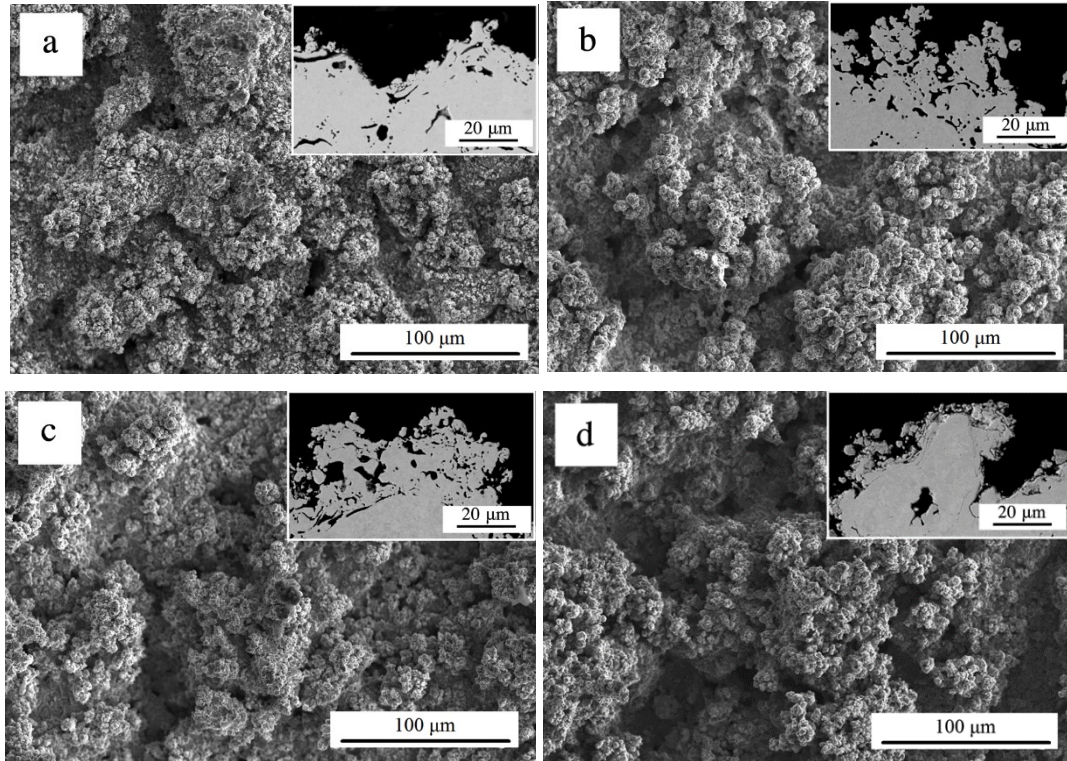
Figure 3.6- Top surface SEM and their cross-sectional BSE micrographs of the reduced electrodes, (a) S3, (b) S6, (c) S10, and (d) unreduced electrode S10.

For these three electrodes, the high surface roughness of the already deposited APS coatings (Figure 3.4) causes deviation of the spraying angle locally from 90° on the existing surface asperities during deposition of the additional SPS layers, which led to the formation of a large variation of roughness values and porosity sizes and levels in the final microstructures [132]. The explanations given previously in section 3.1.2 on the formation of the porous structure with a nonuniform coating thickness also apply for these electrodes.

3.3.2 Surface area and roughness measurements

Figure 3.7 illustrates the CLSM 3D surface topographies of the coated electrodes of scanned surface areas of about 1055×1050 μm^2. Surface ratio of the electrodes (specific area/projected area) and the average surface roughness data (S_a) based on the scanned surfaces of the electrode coatings are presented in Table 3.2. The measured surface roughness of the sandblasted substrate was 4.6 μm.

The results indicate that the APS coated electrode with the surface ratio of 4.6 demonstrated the smallest specific surface area. By addition of the submicron-sized features on the top surface of this electrode, the surface area was increased. By increasing the number of SPS layers, the surface area was more enhanced and the largest area was obtained for electrode S10 with a surface ratio of 7.6. The SPS coated electrode also exhibited a large specific surface area with the ratio of 7.3, whereas the lowest surface roughness was obtained for this sample. This could be due to the small size of the particles that was used to make this deposition directly on the sandblasted substrate with a low surface roughness value, besides deposition of a larger number of passes by SPS compared to electrodes S3, S6 and S10. The images also show that the surface peaks are more uniformly distributed in the APS and SPS coatings compared to those deposited with the combined method.
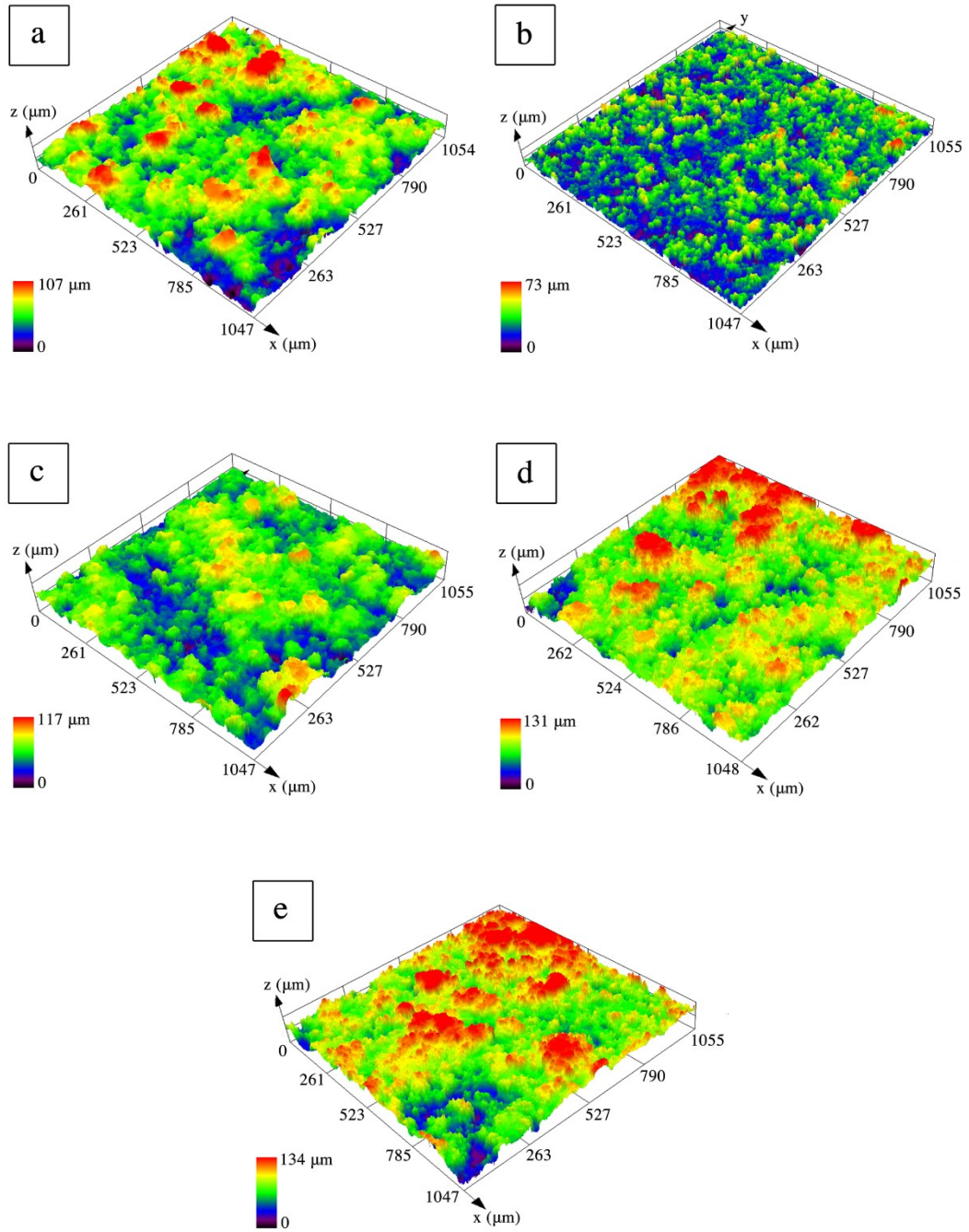
 Figure 3.7- CLSM top surface topography of the coated electrodes: (a) APS, (b) SPS, (c) S3, (d) S6, and (e) S10.

Table 3.2- Surface roughness (S_a) of the Ni electrodes evaluated by CLSM.

	APS	SPS	S3	S6	S10
Surface ratio	4.6	7.3	5.8	7.2	7.6
S_a (µm)	13.4	8.5	12.9	14.4	13.4

3.3.3 Contact angle measurements

The wetting behaviour of water droplets on the coated electrodes is illustrated in Figure 3.8. The smooth nickel surface shows a contact angle of about 100° (Figure. 3.8-a). The contact angle was reduced for the APS coating (Figure. 3.8-b) to about 67° and it was found to be a hydrophilic surface, whereas the SPS coated electrode (Figure. 3.8-c) with a larger contact angle of about 120° exhibited hydrophobic characteristic. For the combined APS-SPS coated electrodes with dual scale morphology (Figures. 3.8-d, 3.8-e, 3.8-f), the water droplets immediately spread out on the surfaces and wet the coatings during the contact angle measurements. They showed superhydrophilic behavior with contact angles well below 10°. Although wetting behaviour of a surface is a complex phenomenon related mainly to the surface topology and chemistry [133], clearly three distinct wetting regimes (hydrophobic, hydrophilic and superhydrophilic) can be identified for APS, SPS, and combined APS-SPS coated electrodes. The wetting behaviour of the electrodes can be explained by a combination of their surface chemistry and topography. However, since it is a very complex phenomenon, further investigation is required to determine the effect of each of these factors, which is beyond the scope of this study.
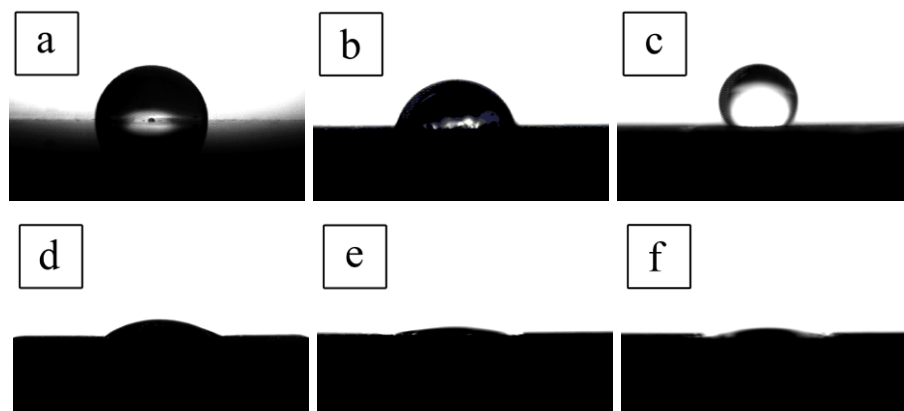
Figure 3.8- Image of water droplets on coated electrode surfaces, (a) smooth nickel surface, (b) APS, (c) SPS, (d) S3, (e) S6, and (f) S10.

3.3.4   Steady-state polarization curves

Steady-state polarization curves were recorded for all coated electrodes and a smooth nickel electrode and are illustrated in Figure 3.9. Corresponding kinetic parameters (Tafel slope b, apparent exchange current density j_0 and overpotential η) of the electrodes are shown in Table 3.3.

All samples showed increased apparent exchange current densities compared to a smooth nickel sample. It was expected for the electrode coated by SPS to show a higher activity compared to the APS coated one due to its enhanced specific surface area (Table 3.2), high level of porosity and ultrafine-structured morphology. Lower j_0 value of this electrode could be related to less accessible electrode/electrolyte interfaces due to the coverage of the inner surface of the pores by hydrogen gas bubbles. It is expected that the hydrophobic surface of this electrode reduces the tendency of the hydrogen bubbles to separate from the electrode surface. This contributes to additional ohmic resistances, and as a result, the overpotential is increased. Accordingly, the largest overpotential value of -570 mV at 250 mA/cm^2 was obtained for this coated electrode.
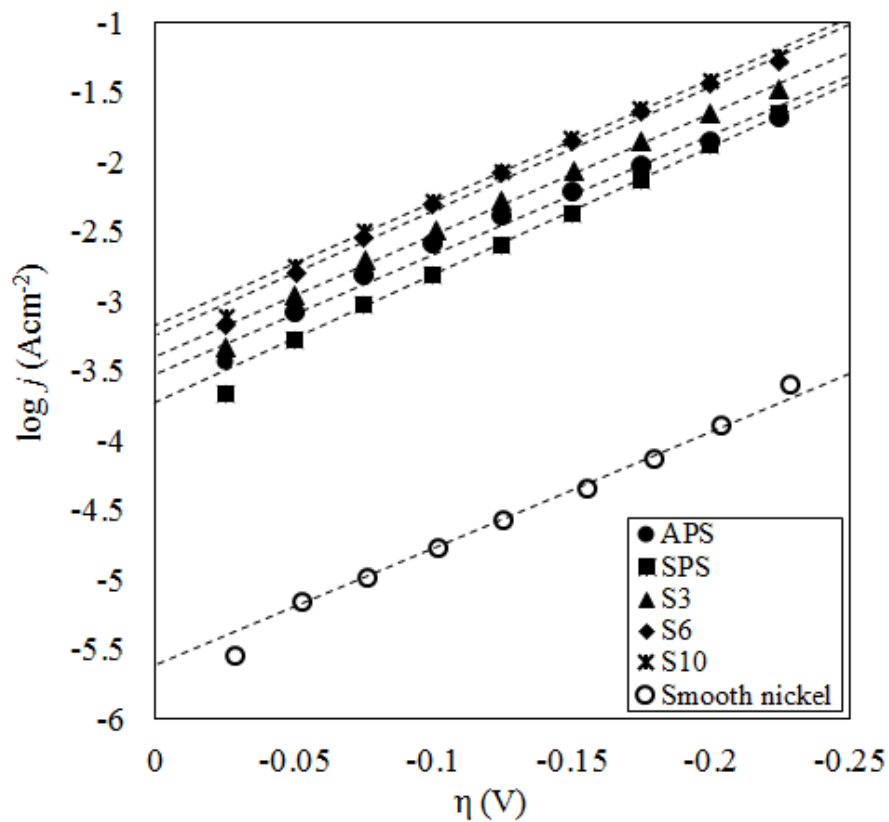
Figure 3.9- Tafel curves obtained for APS, SPS and combined APS-SPS Ni electrodes; j is the apparent current density.

Table 3.3- Kinetic parameters obtained from the steady-state polarization measurements.

Electrode	b (mV/dec)	j_0 (A/cm^2)	η_{250} (mV)
Smooth Ni	101	1.5×10^{-6}	-752
APS	118	3.1×10^{-4}	-451
SPS	108	1.8×10^{-4}	-570
S3	117	4.4×10^{-4}	-439
S6	114	6.2×10^{-4}	-386
S10	114	6.3×10^{-4}	-418

All three electrodes manufactured by the combined APS-SPS coating method demonstrated higher activities compared to those produced by only APS or SPS. Their enhanced activities could be related to their engineered surfaces with multiscale features, and therefore, to their increased surface areas. For these electrode structures, the micron sized features promote the surface accessibility to the electrolyte and lower the surface occlusion by hydrogen bubbles, while the submicron-sized features enhance the surface area of the electrodes. Such structures provide elevated electrode/electrolyte reaction sites, and thus, offer more opportunities for the surface atoms to take part in the HER. It is worth noting that the hydrophilic behaviour of the surfaces is expected to facilitate the bubble ascension as the electrolyte is more likely to replace the gas bubbles. Therefore, improved performances of these electrodes with regard to the hydrogen evolution were obtained.

The largest exchange current densities were obtained for the electrodes S6 and S10 with almost similar values of 6.2×10^{-4} and 6.3×10^{-4}, respectively. As shown in Table 3.3, electrode S10 demonstrated a higher η_{250}, which could be associated with the thickness of the deposited SPS layer. By increasing the thickness of the SPS depositions from 6 to 10 passes, the valleys between the micron sized surface asperities formed previously by APS start to fill up and are replaced by submicron-sized roughness as confirmed by CLSM results in section 3.2. Hence, it would be more difficult for the generated gas bubbles to depart from the electrode surface due to the increased possibility of their entrapment within the fine asperities. As a result, the bubbles screen the pores, limit the electron transfer between the electrode and the electrolyte and contribute to larger energy losses of the electrolysis process. On the other hand, the smallest η_{250} value of -386 mV was obtained for electrode S6, which could be attributed to its surface structure and a larger roughness value that favour easier electron transfer by creating more reaction sites for hydrogen adsorption, and easier escape of hydrogen gas bubbles from the surface. Consequently, this electrode showed the best electrocatalytic activity for the HER.

3.4   Conclusions

Nickel electrode coatings for the HER were deposited by APS, SPS and a combination of both processes. To optimize the number of passes deposited by SPS for maximizing the

efficiency of the HER, 3, 6 and 10 passes were deposited by SPS on top of the APS deposited layers. The results indicated that the combined atmospheric and suspension plasma spray method could be effectively used to develop high performance electrodes for the HER. Using this method, it was shown that the addition of submicron-sized cauliflower-like aggregates by SPS on the rough and porous surface of the APS deposited coatings significantly increases the exchange current density and improves the electrocatalytic activity of the electrodes. The highest electrocatalytic activity was obtained for the electrode that was coated by the combined APS and 6 passes of SPS with the exchange current density and overpotential (η_{250}) values of 6.2×10^{-4} A/cm^2 and -386 mV, respectively. High activity of this electrode was related to the hybrid surface features (submicron/micron), increased surface roughness ($S_a = 14.4$ μm) along with its superhydrophilic behavior (with contact angles below 10°). Within such electrode structure, the hydrogen gas bubbles are expected be easily replaced by the electrolyte and the process energy loss due to the bubble coverage of the surface is expected to be significantly reduced. The combined APS-SPS method could be applied to further increase the efficiency of the electrolysis process by using materials with higher activities such as Raney nickel or nickel molybdenum alloys. The results show that due to the hierarchical structure associated with the combined APS-SPS coatings, the method can be effectively applied to further increase the efficiency of the electrolysis process by using materials with intrinsically higher activities such as Raney nickel. In addition, due to the scalability of this method, this is a promising technology to develop highly electrocatalytic active electrodes for industrial use.

CHAPTER 4

ARTICLE 3: Three-Dimensional Electrode Coatings for Hydrogen Production Formed by Combined Atmospheric and Suspension Plasma Spray

M. Aghasibeig, R. Wuthrich, A. Dolatabadi, C. Moreau

Department of Mechanical and Industrial Engineering, Concordia University
Montreal, QC H3G 1M8, Canada

Abstract

Nickel-based electrode coatings for hydrogen production by alkaline water electrolysis were prepared using atmospheric plasma spraying (APS) and suspension plasma spraying (SPS) methods. To enhance the active surface area of the electrodes and to obtain various levels of surface roughness, three-dimensional fin arrays were fabricated by masking the surface of the substrates with wire mesh screens during APS deposition. Subsequently, SPS top coatings were deposited on the fin-structured electrodes. The coated electrodes were then characterized by studying their surface microstructure, topography, roughness and electrochemical performance. The highest electrocatalytic activity with the exchange current density of 1.8×10^{-3} A/cm^2 and overpotential (η_{250}) of -336 mV was obtained for the

electrode that was coated by the combined APS-SPS method using the mesh screen with the smaller opening size. The high activity of this electrode is mainly attributed to the unique micron/submicron-sized surface structure associated with the deposition of particles through the fine mesh impacting at different angles on the fin geometry, i.e. peaks and valleys.

Keywords: Alkaline water electrolysis, Atmospheric plasma spray, Suspension plasma spray, Surface roughness, Wire mesh screens

4.1 Introduction

High purity hydrogen produced by alkaline water electrolysis is considered to be a promising replacement for fossil derivative fuels [1]. In recent years, water electrolysis has gained wide attention due to the increasing concerns about greenhouse gas emissions and the growing demand for green and renewable energy resources [1, 2]. The produced hydrogen can be stored and used later as an energy carrier in fuel cells or combustion engines [8]. Nonetheless, water electrolysis is still not used for large-scale hydrogen production, as it remains costly due to its high electricity consumption [13, 14]. Therefore, the main challenge is to improve the energy efficiency of the electrolysis process by minimizing the overpotentials of the cathodic (hydrogen evolution) and anodic (oxygen evolution) reactions [13, 16]. One approach to reduce the overpotential of the hydrogen evolution reaction (HER) is employing electrocatalysts with high intrinsic activities [21, 29]. Nickel is widely used as the electrode material for the HER because it is abundant, has high electrocatalytic activity among non-noble metals and is stable in alkaline solutions [20, 28, 134, 135]. Moreover, physical properties of an electrode such as its surface structure have also substantial effect on its catalytic activity. An enhanced electrode surface area provides a larger electrode/electrolyte interface, and thus, more reaction sites for hydrogen adsorption/desorption [13, 27-29, 134]. The surface properties depend substantially on the method used to prepare the electrodes.

Among various thermal spraying methods that have been used to manufacture nickel-based electrodes, atmospheric plasma spray (APS) has shown its capability in development

58

of micron and nano structured active electrode coatings for the HER [72, 98, 125, 136-139]. In this process, the sprayed particles melt and accelerate towards the substrate within the high temperature plasma jet. Subsequently, the deposition layers are formed by impact and flattening of the molten droplets on the substrate at high velocities [81]. Nevertheless, submicron- and nanosized particles cannot be used directly in APS due to the injection difficulties they may impose to the spray system. Suspension plasma spray (SPS) based on the injection of a liquid carrier was developed to overcome this problem. SPS process includes injection of a suspension of solid particles into the plasma jet, atomization and evaporation of the liquid phase, and then melting, acceleration, impact and deposition of the particles on a substrate similar to what was explained for the conventional APS process [84, 85, 140].

In our previous work, it was shown that electrodes with high activities could be developed by combination of the two APS and SPS methods [137, 138]. In this combined method, few SPS layers were deposited on already APS coated electrodes. The superior electrochemical properties of the electrodes were mainly related to their large effective surface areas with unique hierarchical microstructures. The dual micron/submicron-sized surface features enhanced the electrode activity by promoting surface accessibility to the electrolyte, providing more reaction sites for hydrogen adsorption and facilitating hydrogen bubble release from the surface [137, 138].

In the current study, we present a novel approach for further improvement of the electrochemical properties of the electrodes for the HER. In this work, the surfaces of the electrodes were engineered by fabricating different macro- and microscopic levels of surface roughness when applying the combined APS-SPS coatings. For this purpose, the substrates were masked by wire mesh screens during the coating processes and the possibility of forming three-dimensional fin arrays on their top surfaces, through the small openings of the mesh screens, was investigated. Previously, Cormier et al. [141] developed such near net shaped fin arrays by coating aluminum powder through the wire mesh screens using cold spray for manufacturing compact heat exchangers. Similar methodology has also been used by the authors to modify the surface structure of the electrodes for HER using high velocity oxy-fuel (HVOF) process [125]. By producing electrode coatings using the combined APS-SPS method and the mesh screens a considerable improvement in

electrode overpotential is expected, as the developed structural features enhance the electrode/electrolyte contact area at both macro- and microscopic scales. The performance of the electrodes was studied by investigating their microstructural properties and steady-state polarization curves.

4.2 Material and methods

Commercially available powders namely nickel Metco 56C-NS (Oerlikon Metco, USA) and nickel oxide FCM NiO-F (fuelcellmaterials.com, USA) were used to coat Inconel 600 substrate coupons with the surface dimensions of 25×25 mm^2. The particle size distribution of the starting powders was determined to be between 45 to 90 μm with D50 of 69 μm and 100 nm to 11 μm with D50 of 730 nm for nickel and nickel oxide, respectively, using a laser diffraction particle size analyzer (Malvern Instruments Ltd., England) [137].

Nickel electrode coatings were prepared using a 40 kW Sulzer Metco 3MB atmospheric plasma spray gun mounted on a 6-axis robotic arm. The electrodes were coated at two distinct stages. At the first stage, the substrate coupons were masked by plain woven steel wire mesh screens (McMaster-Carr, USA) with two different mesh sizes. The mesh screens were varied in their wire diameter and opening size from one to another. A schematic view of a mesh screen that was used is illustrated in Figure. 4.1. Table 4.1 shows the wire diameter and opening size for each mesh. For both samples, the standoff distance from the mesh to the substrate was fixed at 1 mm. The masked coupons were then coated under similar coating conditions by 40 passes of APS using nickel powder. Figure 4.2 shows a schematic view of the APS process and the developed coating using a mesh screen.
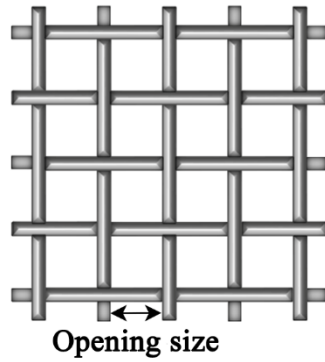
Figure 4.1- A schematic view
of a mesh screen used in the
coating processes.

Table 4.1- Mesh screens dimensions used for masking the substrate coupons in APS.

Mesh name	Opening size (mm)	Open area (%)	Wire diameter (mm)	Number of openings/sample
Coarse mesh	1.91	56	0.64	100
Fine mesh	0.56	51	0.23	1024
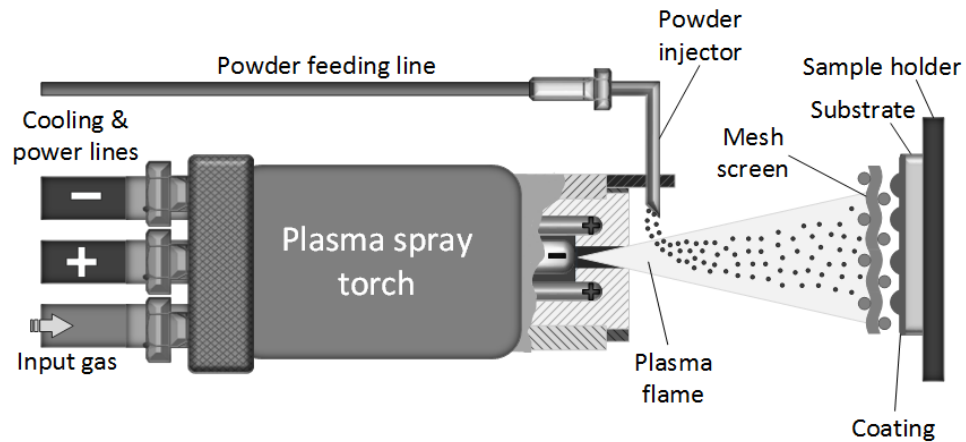
Figure 4.2- Schematic view of the APS process and the developed coating
using a mesh screen.

At the second stage, the mesh screens were removed of the APS coated electrodes from the first stage, and the samples were coated by additional passes of SPS using nickel oxide suspension. The suspension was prepared by mixing 10 wt.% of nickel oxide with 1 wt.% of polyvinylpyrrolidone (PVP) as the dispersing agent in ethanol. The details of suspension preparation and the injection setup for the SPS process is explained in our previous work [136]. Table 4.2 shows the plasma spraying parameters used in APS and SPS coating processes. The parameters were selected based on our previous results [136, 137]. The samples were named according to Table 4.3 throughout this work.

Table 4.2- Spraying parameters used in APS and SPS processes.

Process	Substrate standoff distance (mm)	Powder/suspension feed rate	Plasma gas flow (Ar/H$_2$) (NLPM)	Torch traverse speed (m/s)	Current (A)	Number of passes
APS	80	15 g/min	60/2	0.5	500	40
SPS	60	35 mL/min	50/3	0.5	450	6

Table 4.3- Corresponding reference names for the investigated plasma sprayed coated electrodes.

Ref. name	Description
CM	APS, Coarse mesh screen
FM	APS, Fine mesh screen
CMS	APS-SPS, Coarse mesh screen
FMS	APS-SPS, Fine mesh screen

The velocity and temperature of the inflight particles were measured by a DPV-eVOLUTION particle characterization system (Tecnar Automation Ltd., Canada) for the APS process at the spray distance. The substrate temperature was recorded by an Infrared camera (FLIR A320, FLIR Systems Inc., USA) and a pyrometer (M67S, LumaSense

Technologies, USA) during APS and SPS, respectively. As the coatings were oxidized due to the high flame temperature of APS at atmospheric conditions and deposition of nickel oxide in SPS, the electrodes needed to be reduced. Oxygen reduction of the samples was carried out in a tube furnace by hydrogen gas at 650 ℃ for 1 h, with 2 ℃/min heating and cooling rates.

To study the cross-sections of the coatings, the samples were cut using a precision cut-off machine (Secotom-15, Struers, Denmark), cold mounted in epoxy and then polished by standard metallographic procedures to a final finish of 0.05 μm. An optical microscope was then used to study the cross-sections of the samples. A 3-D Confocal Laser Scanning Microscope (CLSM) (LEXT-OLS4000, Olympus Corporation, Japan) with a Z-axis height resolution of 10 nm and a lateral X-Y resolution of 120 nm was used for three dimensional topography imaging of the coatings and to evaluate the roughness of the sprayed samples. The top surface morphology of the coatings was observed by a scanning electron microscope (SEM) (S-3400N, Hitachi High Technologies America, Inc., USA) operating at 15 kV.

A standard three-electrode cell was used for the electrochemical measurements. In this setup, the coated samples as the working electrode, a platinum wire as the counter electrode and an Hg/HgO reference electrode saturated in 1 M KOH (-0.924 V vs. Hg/HgO) were fixed in a Pyrex cell containing a 1 M NaOH electrolytic solution. The electrolyte was bubbled with nitrogen throughout the whole measurements to remove its oxygen content. All measurements were carried out at room temperature (25 ℃). Before each measurement, surface oxide layers were removed by pre-polarization of the working electrode at -1.6 V vs. Hg/HgO for 1800 s. Tafel polarization curves in the current range of 10 μA to 1 A were obtained using a SRS potentiostat (EC301, Stanford Research Systems, Inc., USA). The kinetic parameters including the Tafel slope, b, and exchange current density, j_0, were determined from extrapolation of the linear part of the Tafel curves to the equilibrium potential. The overpotential of the electrodes was measured at an applied current density of 250 mA/cm^2 in the galvanostatic mode.

4.3 Results and discussion

4.3.1 Microstructural characterization

4.3.1.1 Surface morphology

Figure 4.3 shows SEM overview images of the coatings for electrodes CM and FM. The fins present trapezoidal prism geometry in CM, whereas they are dome shaped in FM. Both coatings present highly porous structures, specifically in the grooves formed under the mesh wires as well as on the slopes of the fins.
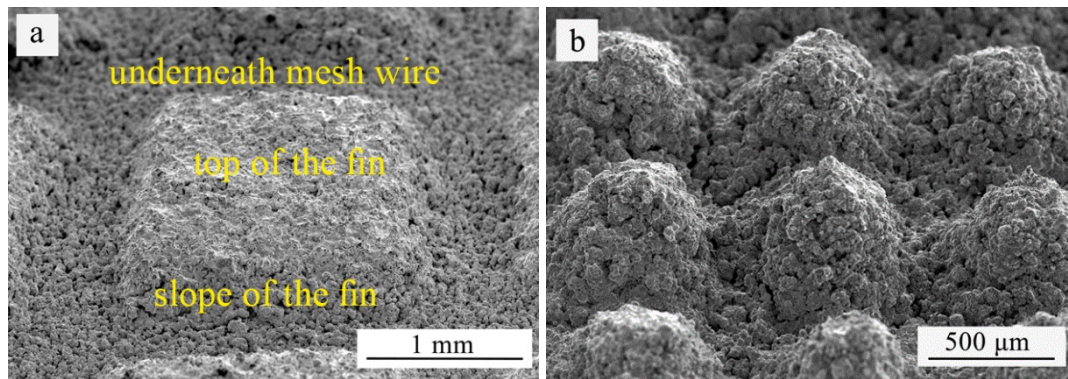
Figure 4.3- SEM overview of the fin arrays deposited by APS (a) CM and (b) FM.

SEM micrographs of the top surfaces of the fins are presented in Figures 4.4-a and b for electrodes CM and FM, respectively. It can be seen that the microstructure of electrode CM is comprised of a combination of flattened splats, fragmented splats and resolidified droplets. The diameter of some of the splats are as large as 100 μm suggesting that the largest particles were fully melted under the spraying conditions. For electrode FM, only few particles are deposited on the top surface of the fins due to smaller size of the wire mesh openings. For this sample, clogging of some of the mesh screen openings by nickel powder was noted after deposition of 40 passes, which could be related to its small opening size compared to the particle size that was used. For both coatings the substrate temperature during the coating process was measured in the range of 90 to 165 °C. Temperature and

velocity of the inflight particles at the point of impact were measured 2145±204 ºC (SD) and 109±28 m/s (SD), respectively. Impingement of the molten particles at high temperature and velocity to the low temperature substrate could have caused the formation of splashed splats on the surfaces of these fins. Figures 4.4-c and d show the SEM images of the depositions underneath the mesh wires for electrodes CM and FM, respectively. The coatings are composed of well-connected fine resolidified splashed droplets and agglomerates with irregular shapes. A high level of porosity can be identified between the agglomerates. The particles that were deposited to form the grooves of electrode CM (≤50 µm) seem to be smaller compared to electrode FM (≤80 µm). This could be due to the greater thickness of the coarse mesh wires, and thus, their higher shadowing effect that allows penetration and deposition of mainly the smaller particles underneath the mesh wires during the coating process.
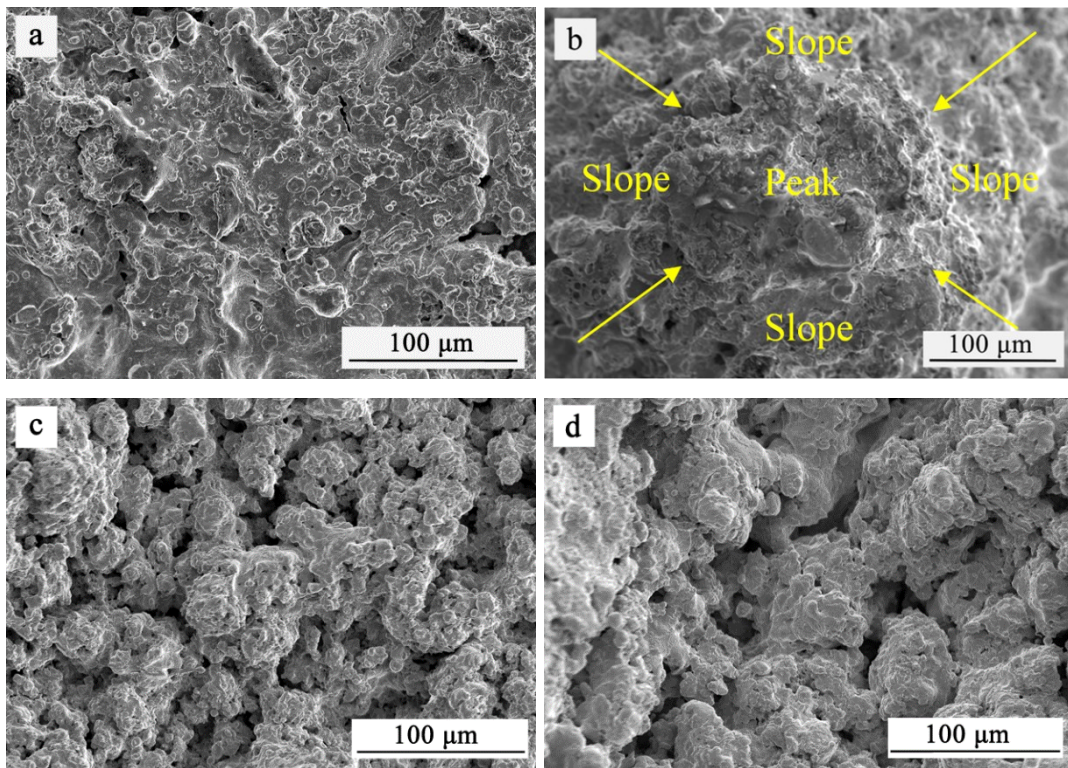
Figure 4.4- SEM images of the coated electrodes deposited by APS (a) top surface of a fin in CM, (b) top surface of a fin in FM, (c) underneath the mesh wire in CM, and (d) underneath the mesh wire in FM.

Figure 4.5-a to d illustrates the SEM images of the samples coated by the combined APS-SPS process. In both electrodes cauliflower like submicron-sized features were added by SPS on top of the micron sized surface asperities coated by APS. As it is expected, the top surface morphology of the fins (Figures. 4.5-a and b) is similar to what was observed before for the flat electrode surface, coated by the combination of APS and 6 passes of SPS [137]. The substrate temperature during the coating process was measured in the range of 200 to 220 °C in the first SPS pass and 390 to 450 °C in the last SPS pass. The relatively low substrate temperature for SPS is due to the large standoff distance (6 cm). At this spray distance, a large fraction of the particles were resolidified prior to the impact due to their small size. Therefore, it is expected for these coated surfaces to display a higher ratio of porosity and roughness values compared to those formed solely by APS. In addition, untreated and poorly treated particles in plasma jet fringes, voltage fluctuations of the plasma jet, different trajectory of the particles due to the wide range of particle size distribution, evaporated particles, stagnation flow on the substrate and reduction of the oxides could also have yielded the highly porous microstructures of these electrodes [107, 130, 131, 137].
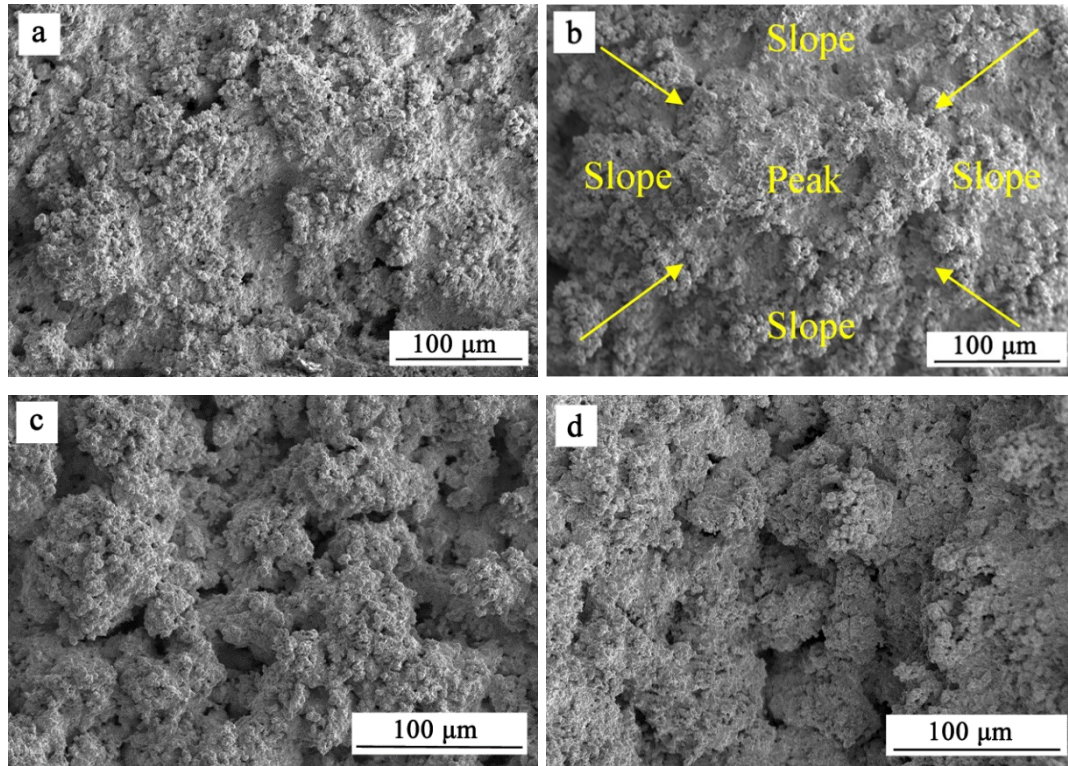
Figure 4.5- SEM images of the coated electrodes deposited by the combined APS-SPS (a) top surface of a fin in CMS, (b) top surface of a fin in FMS, (c) underneath the mesh wire in CMS, and (d) underneath the mesh wire in FMS.

4.3.1.2   Cross-sectional studies

Figure 4.6 shows the cross-sectional images of the coatings deposited by APS and combined APS-SPS. A good adhesion between all the coatings and the substrates was obtained. The thickness of the fins at their peaks is approximately 550 µm for electrodes CM and CMS, and 450 µm for electrodes FM and FMS. A high level of porosity can also be observed in all coatings. Formation of porous structures could be related to the selected spraying conditions. The pores during APS process are mainly formed in splat boundaries and can be attributed to the splashing of the splats at high impact temperatures and velocities. In addition, gas entrapment underneath the splats at low substrate temperatures could also promote splashing of the impinging droplets and the formation of interlamellar pores [128, 129, 137]. It can be seen from the figures that the thickness of the deposits

underneath the mesh wires is approximately 80 µm (Figures. 4.6-a and b) and 200 µm (Figures. 4.6-c and d) when coarse and fine mesh screens were used, respectively. When the coarse mesh screen with larger wire diameter was used, less particles could reach beneath the wires and consequently deposit on the substrate. On the contrary, material flow under the mesh wires was facilitated when fine mesh screen with smaller wire diameter was used. For the coatings formed by APS (Figures. 4.6-a and c) smoother surfaces can be observed, whereas the coating surfaces exhibit higher roughness when submicron sized features were added by SPS (Figures. 4.6-b and d). This can also be clearly seen in the magnified images of the coatings formed using the coarse mesh screen shown in insets in Figures. 4.6-a and b. Since the SPS layers are well-bonded to the beneath APS coatings, no clear boundary could be observed between them.
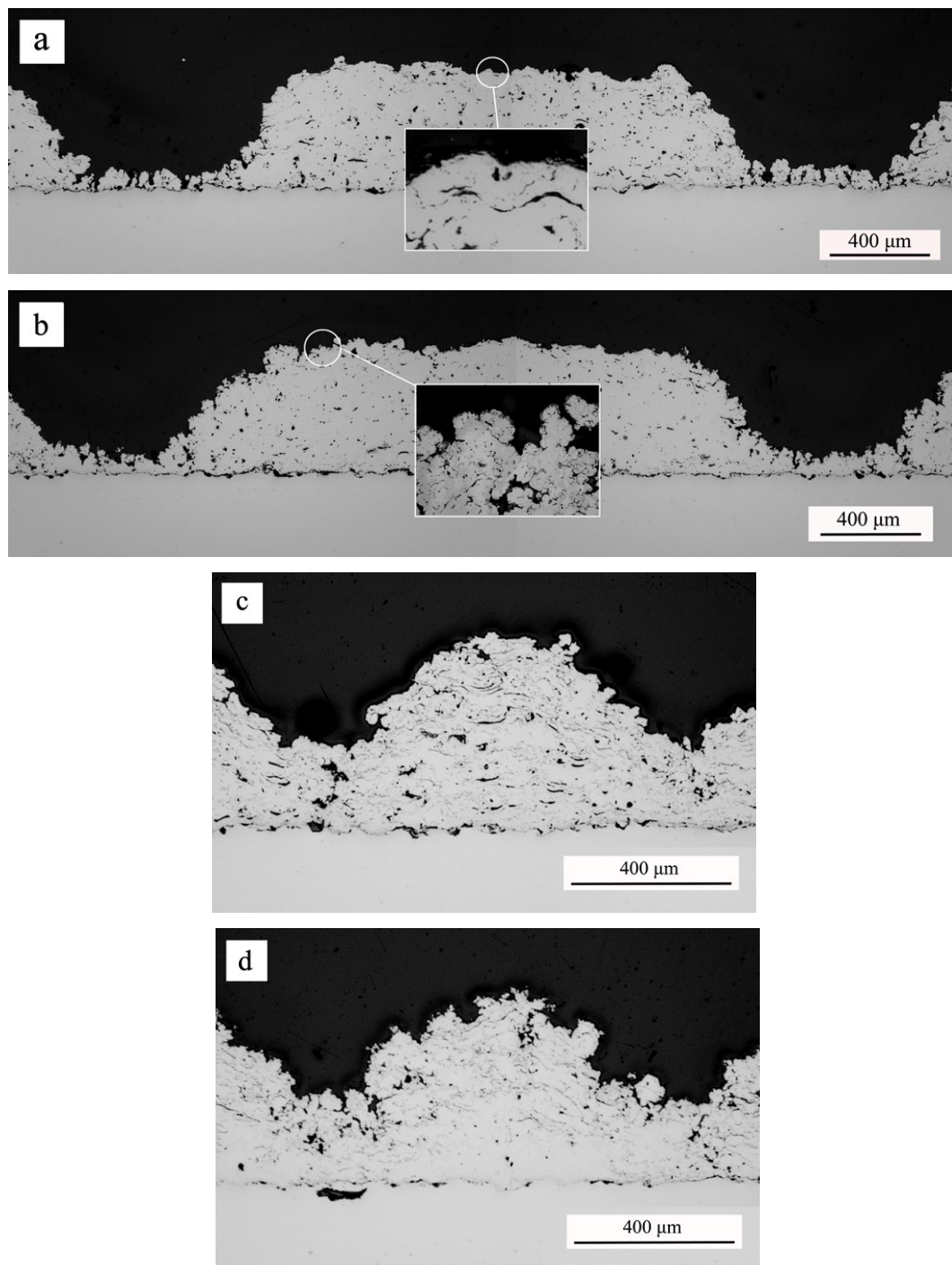
Figure 4.6- Optical microscopy cross-sectional images of electrodes (a) CM, (b) CMS, (c) FM, and (d) FMS. The insets show magnified views.

4.3.2 Surface roughness

Three dimensional surface topographies of the coated electrodes for the scanned surface areas of about 2930×2940 μm^2 are illustrated in Figure 4.7. Table 4.4 presents the average line roughness data (R_a) based on 7 measurements at each area and the surface ratio (specific area/projected area) based on the scanned surfaces of the electrodes. As shown in Table 4.4, a large variation of the surface roughness was obtained for each coating, which could be related to the impact and deposition of the particles at different angles on top of the fins, slopes of the fins and in the grooves due to the different heights and slopes of the previously deposited APS layers. A roughness value of 13.6 μm was obtained on the top surface of the fins for electrode CM, whereas a lower roughness of 8.7 μm was obtained for electrode FM. Contrary to the top surfaces, roughness of the coatings deposited underneath the mesh wires and on the slopes of the fins were lower for CM compared to FM. For these APS coated electrodes, the highest roughness value of 17.6 μm was obtained for the fin slopes of electrode FM. This could also be related to the lower thickness of the fine mesh wires, and therefore, penetration and deposition of larger particles underneath the wires. In addition, the possibility of the inflight particles to impact and deposit on the surface at different angles is expected to be higher for electrode FM due to the larger numbers of fins per unit area, and thus, it contributed to the increased surface roughness values.
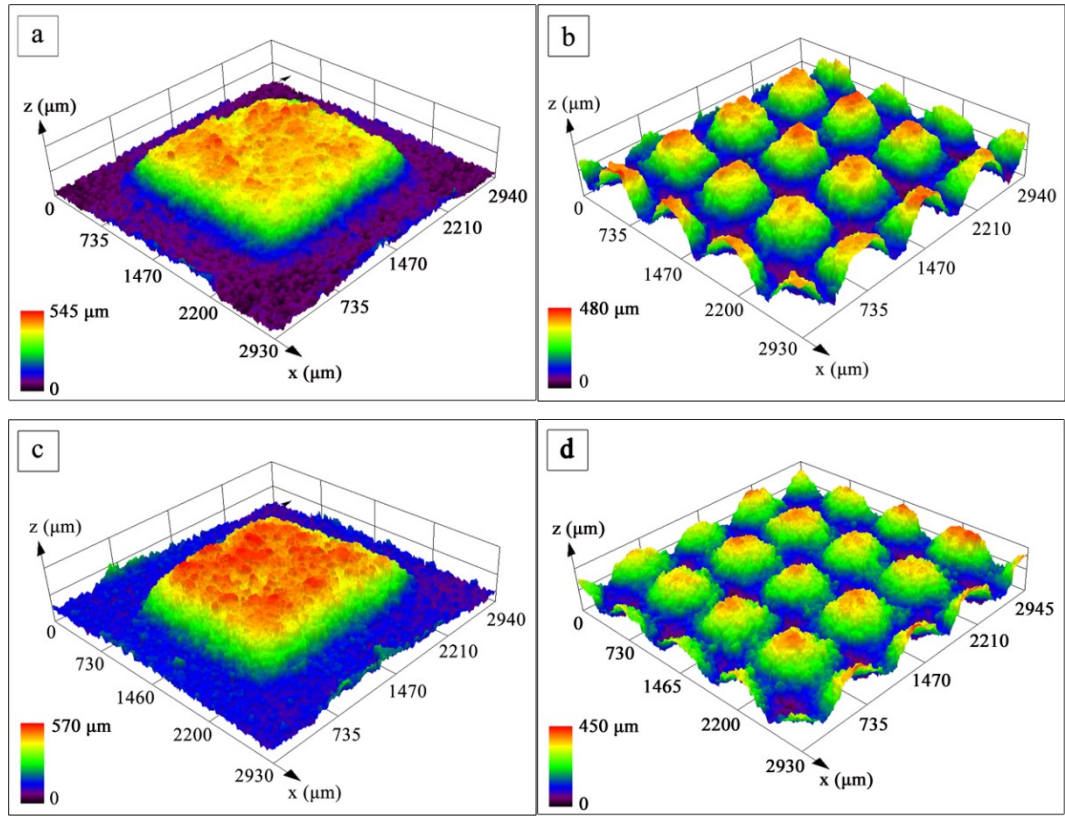
Figure 4.7- CLSM top surface topography of the electrodes: (a) CM, (b) FM, (c) CMS, and (d) FMS.

Table 4.4- Line roughness (R_a) and surface ratio values of the nickel coated electrodes evaluated by CLSM.

Electrode	Top surface of the fins	Under mesh wires	Slopes of the fins	Surface ratio
		R_a (μm)		
CM	13.6	8.9	14.3	5.9
FM	8.7	9.3	17.6	7.1
CMS	15.9	10.8	16.9	6.1
FMS	10.8	10.9	18.3	8.4

For both mesh sizes, the electrode surface roughness and specific surface areas were increased by deposition of the additional SPS layers (Table 4.4). The increased values could be related to the addition of the submicron-sized features on the top surface of these electrodes with micron sized asperities. Following the same trend as in the case of APS coated electrodes, the highest roughness of 18.3 μm was obtained for electrode FMS on the fin slopes. This electrode also showed the highest specific surface area with the surface ratio of 8.4. Higher surface ratio for the electrodes coated using the fine mesh screen are not only induced by the larger number of the fins (macroscopic features) but also by the microscopic surface features produced by deposition of the particles, specifically on the fin slopes. This matter is discussed more in details in the next section (section 3.3).

4.3.3 Electrochemical measurements

Figure 4.8 presents the steady-state polarization curves obtained for the coated electrodes to evaluate the effect of the extended surface area (i.e. fins) as well as deposition of micron/submicron-sized particles on the activity of the electrodes. The apparent values of kinetic parameters in the HER (apparent exchange current density j_0, Tafel slope b and overpotential η) are shown in Table 4.5. These values are calculated considering the projected surface area of the electrodes. The results are then compared to those previously obtained for the electrodes coated by APS and APS-SPS processes without using any mesh screens as well as a nickel electrode with a smooth surface (Table 4.5) [137].
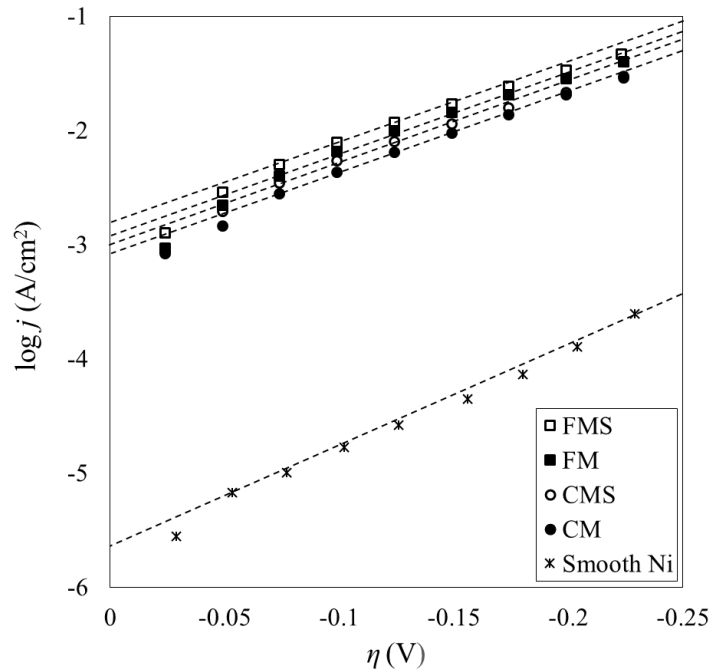
Figure 4.8- Steady-state polarization curves obtained for electrodes CM, FM, CMS, and FMS based on their projected surface area; j is the apparent current density.

Table 4.5- Kinetic parameters obtained from the steady-state polarization measurements based on the electrodes projected surface areas. The values marked by an asterisk (*) are extracted from the previous results [137].

Electrode	b (mV/dec)	j_0 (A/cm^2)	η_{250} (mV)
CM	147	9.1×10^{-4}	-396
CMS	159	1.3×10^{-3}	-350
FM	152	1.4×10^{-3}	-366
FMS	156	1.8×10^{-3}	-336
APS[*]	118	3.1×10^{-4}	-451
APS-SPS[*]	114	6.2×10^{-4}	-386
Smooth Ni[*]	101	1.5×10^{-6}	-752

73

It can be seen that the Tafel slopes of the electrodes coated using mesh screens were increased compared to the smooth surface nickel sample and the electrodes coated using no mesh. However, they showed improved electrocatalytic activities for the HER by demonstrating increased exchange current densities and lower overpotentials. This is probably due to the increased surface areas available for the HER due to the fin geometries, which yielded to superior electrochemical performances for a given surface. The highest j_0 value of 1.8×10^{-3} A/cm^2 and the lowest η_{250} of -336 mV were obtained for electrode FMS. A contribution to this high activity is certainly the large engineered electrode surface area with a high roughness value (Table 4.4) composed of macroscopic fin arrays with micron/submicron-sized features produced by the combined APS-SPS process using the fine mesh screen. Electrode CM was found to be the electrode with the lowest activity among those coated in this work with j_0 value of 9.1×10^{-4} A/cm^2 and η_{250} value of -396 mV. Although this electrode showed a higher exchange current density than the APS-SPS electrode coated without using mesh, it showed a lower catalytic activity for the HER due to its larger Tafel slope and higher η_{250}.

In order to consider the net effect of the microscopic structure and the associated surface roughness on the improved activities, the exchange current densities were corrected by removing the effect of the macroscopic surface. Accordingly, Figure 4.9 and Table 4.6 present the normalized steady-state polarization curves and the exchange current densities, respectively, based on the calculated corrected surfaces.

The results show that j_0 values were reduced slightly in all samples compared to the cases using the projected area (i.e. Table 4.5). However, they are still at least two times higher than their APS and APS-SPS electrode counterparts coated using no mesh. Therefore, it can be concluded that the macroscopic structure of the fins had a minor effect on the catalytic activity of the electrodes for the HER, and the activity was mainly increased due to the microscopic (and possibly nanoscopic) roughness levels and the enhanced surface areas induced by the spraying processes. For these electrodes, various roughness levels were obtained on the top and slopes of the fins as well as underneath the mesh wires owing to the shadowing effect of the mesh wires and the shape of the fins. The produced surface structures are expected to not only provide more reaction sites for hydrogen adsorption and desorption, but also facilitate the detachment of the produced bubbles from

the electrode surface and the pores. This suggests that the surface structure is the main factor determining the rate of the HER and activity of these electrodes.
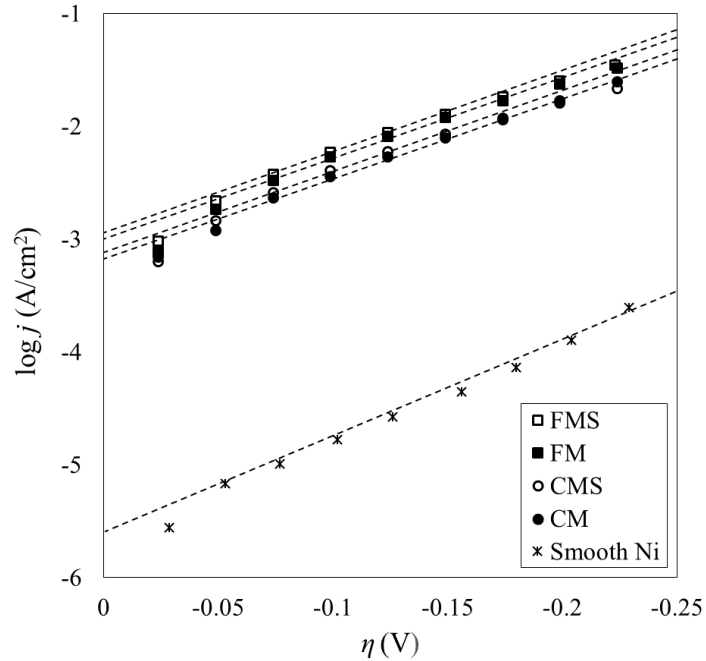
Figure 4.9- Steady-state polarization curves obtained for electrodes CM, FM, CMS, and FMS based on their corrected projected surface areas; j is the apparent current density.

Table 4.6- Kinetic parameters obtained from the steady-state polarization measurements based on the electrodes corrected projected surface areas.

Electrode	CM	CMS	FM	FMS
j_0 (A/cm^2)	7.5×10^{-4}	9.5×10^{-4}	1.1×10^{-3}	1.4×10^{-3}

As it can be seen in Table 4.1 the percentages of the open areas are very close for coarse and fine mesh screens (56% for the coarse mesh vs. 51% for the fine mesh). Therefore, although electrode CM showed a higher roughness on the top surface of the

fins, considering the larger roughness values of the surfaces under the mesh wires and on the fin slopes for electrode FM (see Table 4.4), an elevated total surface roughness is acquired for this electrode. As a result, a higher exchange current density was obtained for electrode FM independent of the macroscopic surface that was added by the fins. In addition, the submicron-sized features added to the surface by SPS further increased the activity for this electrode and FMS with j_0 value of 1.4×10^{-3} A/cm^2 was characterized as the best electrocatalysts for the HER.

4.4 Conclusions

APS and the combined APS-SPS coating processes were used to fabricate nickel electrode coatings with enhanced electrocatalytic activities for the HER. For this purpose, two mesh screens with different wire sizes and mesh densities were used to mask the substrates during APS process. Consequently, different macro- and microscopic levels of surface roughness were created by manufacturing three-dimensional fin arrays. The results showed different roughness values and microstructures on the top of the fins, slopes of the fins and under the mesh wires. The electrode that was coated using the mesh with thinner wire diameter and smaller opening size showed a higher specific surface area, and accordingly, a better electrocatalytic activity with j_0 and η_{250} values of 1.4×10^{-3} A/cm^2 and -366 mV, respectively. The activity of this electrode was further increased by addition of submicron-sized features using SPS process with the highest j_0 and lowest η_{250} values of 1.8×10^{-3} A/cm^2 and -336 mV, respectively. The increased activity was attributed to the enhanced specific surface area with the surface ratio of 8.4 besides the highest roughness values of 18.3 μm and 10.9 μm that were obtained on the fin slopes and under the mesh wires, respectively. This electrode still exhibited the highest electrocatalytic activity with j_0 value of 1.4×10^{-3} A/cm^2, even when the effect of the macroscopic features introduced by the fin geometries was eliminated. The results clearly emphasize that the microscopic surface roughness created by the spraying processes plays the dominant role in determining the activities of the electrodes. Producing electrodes with various roughness levels using the combined APS-SPS method and mesh screens provides an opportunity to considerably improve their performances for the HER not only by enhancing the electrode/electrolyte

interfaces but also by facilitating the hydrogen bubble separation from the electrode surface. This introduced methodology could be applied using nickel-molybdenum or Raney nickel alloys to further increase the intrisic activity of the electrodes besides their apparent activities.

CHAPTER 5

ARTICLE 4: Engineered Three-Dimensional Electrodes by HVOF Process for Hydrogen Production

M. Aghasibeig, C. Moreau, R. Wuthrich, A. Dolatabadi

Department of Mechanical and Industrial Engineering, Concordia University
Montreal, QC H3G 1M8, Canada

Abstract

High velocity oxy-fuel process was used to prepare nickel electrode coatings for hydrogen production by alkaline water electrolysis. To further increase the active surface area of the electrodes, pyramidal fin arrays with two different sizes were deposited on the top surface of the electrodes using mesh screen masks. The surface microstructure, topology and roughness of the coatings were studied using scanning electron microscope, optical microscopy and confocal laser scanning microscopy. Steady-state polarization curves were used to evaluate the electrocatalytic activity of the electrodes. The performance of the electrodes coated using mesh outperformed the electrode deposited without using mesh. In addition, the electrode that was coated using the coarse mesh was characterized with the highest activity with the exchange current density and overpotential values of 9.3×10^{-3} A/cm^2 and -306 mV, respectively. Formation of different roughness levels due to the

combination of normal and off-normal impact of the coating particles on the surface of the fins was identified as the main factor for the increased activity of this electrode towards the hydrogen evolution reaction.

5.1   Introduction

In recent years, hydrogen evolution reaction (HER) has been extensively studied due to the rising demand for replacing fossil fuels with green and renewable energy alternatives [1, 2]. Although water electrolysis is considered to be a sustainable route to obtain high purity hydrogen, it is still not used for large scale hydrogen production in industrial applications. This low market is mainly associated with the high costs of the electrolysers and high energy consumption of the electrolysis process [13, 14]. Therefore, the main challenge for further development of water electrolysis is to reduce the cost of the catalysts and diminish the cell energy losses due to the overpotentials [13, 16]. Platinum group metals represent the highest electrocatalytic activity for the HER, however, they are rare and expensive and need to be replaced by other materials with high catalytic activities [20]. Nickel has been widely investigated as the electrode material since not only it is electrocatalytically active, but also it has high stability in alkaline solutions. It also has much lower costs than the noble metals [13, 20, 24]. Its lower electrocatalytic activity (compared to platinum group metals) could be compensated by increasing its intrinsic activity, for instance by using nickel-based alloys, or by improving its apparent activity by enhancing the ratio of the real to geometric surface area. The real surface area of an electrode could be enlarged by controlling the surface morphology, which depends on the method of fabrication [20, 21, 27-29, 119, 136].

Thermal spraying processes have shown their capability to deposit electrocatalytically active nickel-based electrode coatings for the HER with large surface areas [26, 73, 136, 139, 142]. Among different thermal spraying techniques, high velocity oxy-fuel (HVOF) is expected to be a promising method for producing active electrode

coatings for the HER. In general, HVOF characterized by high particle velocity and relatively low temperatures, allows deposition of surface coatings with low-oxide contents [77]. The microstructure of the coatings could be controlled by interplay of the spraying parameters, specifically by the ratio between the oxy/fuel gases and their flow rates [143].

The present study investigates the possibility to develop active electrode coatings for the HER using HVOF. The spray parameters were selected to ensure deposition of solid state particles on the surface of the electrodes, and to resemble the coatings deposited by the cold spray process, developed in a previous study by the authors [139]. In addition, the surface texture of the electrodes was engineered to create three-dimensional pyramidal fin arrays by masking the substrates, using wire mesh screens during the coating process. It is expected that the manufactured unique electrode structures provide more reaction sites for the HER due to the higher electrode surface areas generated by the masking method and the spraying process, as observed recently in structured plasma sprayed electrode surfaces [144]. The specific morphology and low oxide content of HVOF coatings combined with the formation of three-dimensional fin arrays has the potential to further increase the activity of the electrodes for the HER. The influence of the mesh density on the microstructure and electrocatalytic activity of the coatings was investigated.

5.2 Material and methods

Nickel Metco 56C-NS (Oerlikon Metco, USA) powder with spherical morphology, shown in Figure 5.1-a, was used as the feedstock powder to coat sand blasted Inconel 600 substrate coupons with the dimensions of $25 \times 25 \times 7$ mm^3. The powder size distribution, characterized by a laser diffraction particle size analyzer (Malvern Instruments Ltd., England), was determined to be 45 to 90 μm with the mean particle size (d32) of 67 μm. Figure 5.1-b shows the particle size distribution of the feedstock nickel powder.
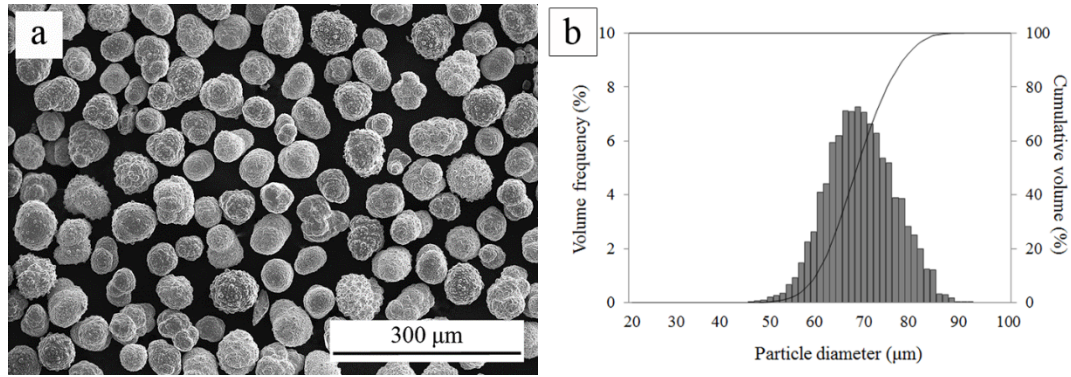
Figure 5.1- (a) SEM morphology and (b) histogram of the particle size distribution of the feedstock powder.

Deposition of the coatings was carried out using a 113 kW Diamond Jet HVOF gun (model 2700DJM, Oerlikon Metco, USA). For all the experiments, oxygen and propylene were used as the oxy-fuel mixture with flow rates of 170 and 50 SLPM, respectively. In addition, the air flow was 320 SLPM. The coatings were deposited at a powder feeding rate of 25 g/min, a constant spray distance of 24 cm with the robot transverse speed of 1 m/s and 3 mm step between each torch passage. The spraying parameters were selected to reduce the temperature of the spray particles for deposition of solid state particles, minimize oxidation and create rough surfaces. A total number of 100 passes were deposited on each sample. In addition to the case of bare substrate, woven steel wire mesh screens (McMaster-Carr, USA) with two mesh densities were placed at a distance of 1 mm from the substrate. Table 5.1 presents the dimensions of the two screens used in this work. A schematic view of the HVOF process and the deposited coating under a mesh screen is shown in Figure 5.2.
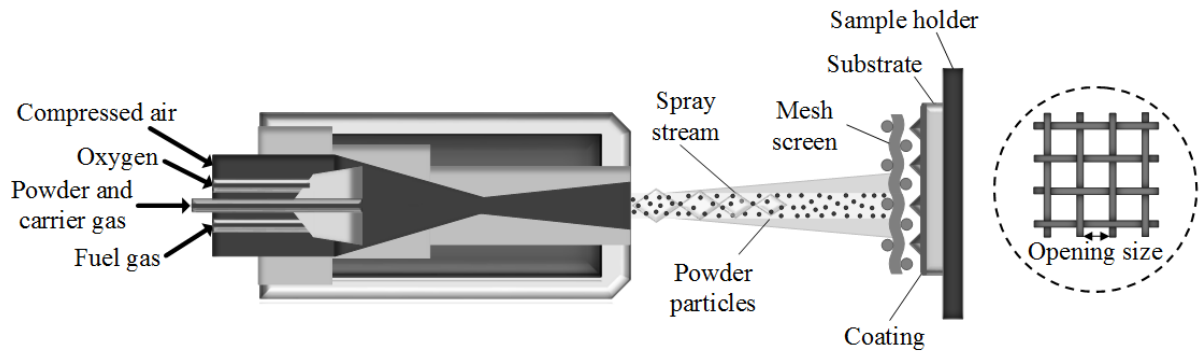
Figure 5.2- Schematic view of the HVOF process and the developed coating using a mesh screen.

Table 5.1- Dimensions of the mesh screens used for masking the substrates in the coating process.

Mesh name	Opening size (mm)	Open area (%)	Wire diameter (mm)	Number of openings per sample
Coarse mesh	1.91	56	0.64	100
Fine mesh	0.56	51	0.23	1024

The substrate temperature was measured during the spraying process, using an Infrared camera (model FLIR A320, FLIR Systems Inc., USA). To characterize the cross-sections of the coatings, they were cut vertically across and cold mounted in epoxy. The samples were then ground and polished to a final finish of 0.05 μm diamond suspension to obtain mirror like surfaces. The cross-sections were studied using an optical microscopy. A scanning electron microscope (SEM) (model S-3400N, Hitachi High Technologies America, Inc., USA) operating at 15 kV was used to study the morphology of the starting powder and the top surface of the coatings. The surface topography and roughness of the electrodes were evaluated using a LEXT three-dimensional confocal laser scanning microscopy (CLSM) (model OLS4000, Olympus Corporation, Japan) with a Z-axis height resolution of 10 nm and a lateral X-Y resolution of 120 nm.

The electrochemical measurements were carried out using a three electrode setup at room temperature (25 °C). The working electrode was the coated sample, the counter electrode a platinum wire and the reference electrode Hg/HgO saturated in 1 M KOH (-0.924 V vs. Hg/HgO). Oxygen was removed from the electrolyte by bubbling nitrogen

throughout the whole measurements. The steady-state measurements were carried out using a SRS potentiostat (model EC301, Stanford Research Systems, Inc., USA) in the current range of 10 μA to 1 A, after the working electrode was pre-polarized at -1.6 V vs. Hg/HgO for 1800 s to remove the surface oxides. The linear part of the polarization curves were extrapolated to the equilibrium potential to evaluate the kinetic parameters including the exchange current density, j_0, and the Tafel slope, b. The electrode overpotentials were measured at an applied current density of 250 mA/cm^2 in the galvanostatic mode.

5.3   Results and discussion

5.3.1   Microstructural studies

Figure 5.3-a shows the top surface SEM image of the coating deposited without using a mesh. The presence of unmelted particles embedded in a matrix of partially and fully molten particles is evident on the top surface of this coating. The final spherical and hemisphere shapes of the deposited particles feature the low temperature and velocity of the inflight particles. This could be attributed to the low gas temperature due to the rather low flow rates of the fuel gas and oxygen (compared to nominal operating conditions of a typical HVOF gun). Considering the size of the deposited particles (Figure 5.3-a), it can be concluded that the particles with diameters larger than 70 μm were those that could not fully melt under the selected spraying conditions.

In the cross-sectional view of this coating shown in Figure 5.3-b, the splat/splat boundaries with few pores between the stacked particles could be clearly discerned. The coating thickness is approximately 650 μm, suggesting a low deposition efficiency for 100 passes considering the size of the spray particles. For the partially melted particles, the molten part spreads well on the surface of the substrate or on the previously deposited layer upon their impact, while the unmelted portion forms a hemisphere [145]. However, if the particle is unmelted, there is a great possibility that it rebounds from the surface, which contributes to a poor intersplat adhesion and low deposition efficiency [145]. The substrate temperature was measured 53 °C for the first pass and 146 °C for the last pass during the deposition process. This relatively low substrate temperature, even when the coating

temperature is increased due to the repeated traverse of the gun, results in less oxidation of the coating because of the rapid cooling rate of the deposited particles. For this coating, oxidation amount is expected to be very low as the particles were not fully melted owing to the low gas temperature, and it could not be detected by XRD as shown in the pattern in Figure 5.4. This coating microstructure is very similar to what was observed before for the electrode coatings formed by deposition of solid state particles using cold spray process [139].
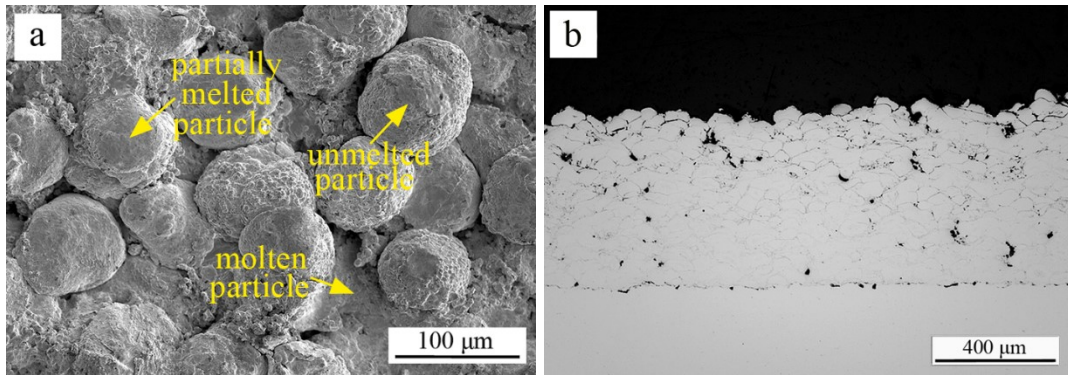
Figure 5.3- Micrographs of the HVOF coated electrode formed without using a mesh, (a) SEM of the top surface and (b) cross-section.
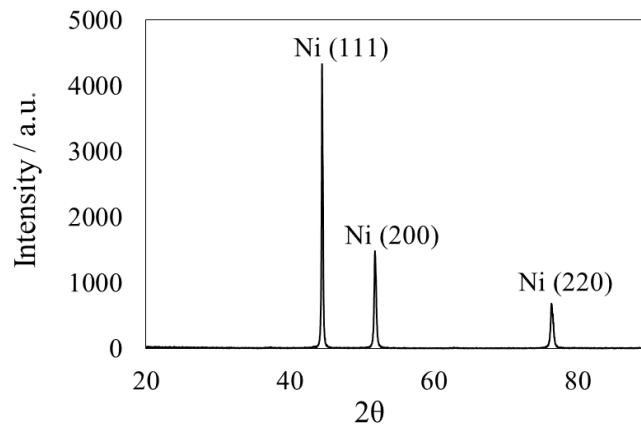
Figure 5.4- XRD pattern of the HVOF coating deposited without using a mesh screen.

SEM overview images of the coatings fabricated using mesh screens are illustrated in Figure 5.5. The generated fins present trapezoidal prism geometry when the coarse mesh (Figure 5.5-a), and pyramidal arrays when the fine mesh (Figure 5.5-b) were used to mask the substrates. Deposition of well-developed pyramids, when the substrate was masked by the fine mesh results from its small opening size. Formation of the pyramidal shapes could be related to the deposition of the solid state particles, which was similarly observed by Cormier et al. [141, 146] when cold spray process was employed to manufacture fin arrays for compact heat exchanger. However, if the particles were fully melted, for instance by using plasma spray [144], the pyramidal shape of the fins could not be obtained. For both samples, the images clearly show that the obtained microstructures were varied on the fins and underneath the mesh wires.
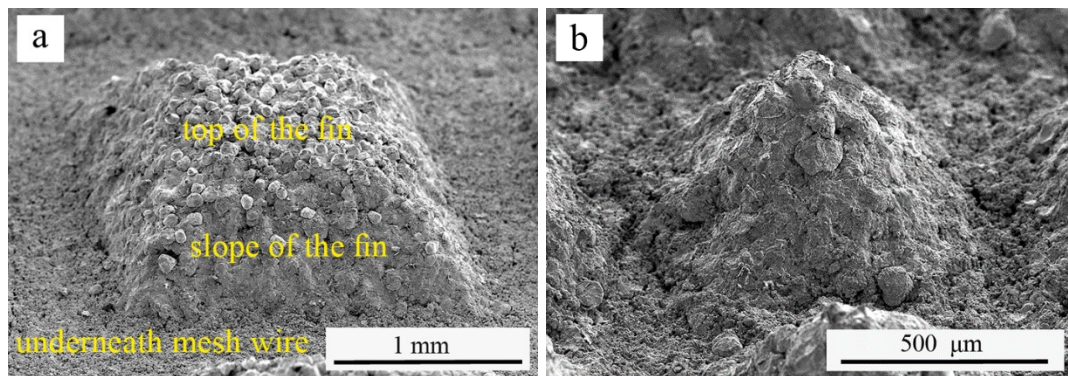
Figure 5.5- SEM overview of the fin arrays developed by HVOF by using (a) coarse and (b) fine mesh screens.

The SEM micrographs of the top surface of the fins and underneath the mesh wires of each sample coated using mesh are shown in Figure 5.6. For the electrode coated using the coarse mesh (Figure 5.6-a), the deposition morphology on the top surface of the fins resembles what was observed before for the sample coated without using a mesh. Due to the small opening size of the fine mesh screen, only few particles were deposited on the top of the fin (Figure 5.6-c). In addition, underneath the mesh wires, smaller molten and fragmented particles could penetrate and deposit, which formed a network of fine

agglomerates with sizes between 5 to 40 μm, encompassing a high level of porosity (Figure 5.6-b and d).
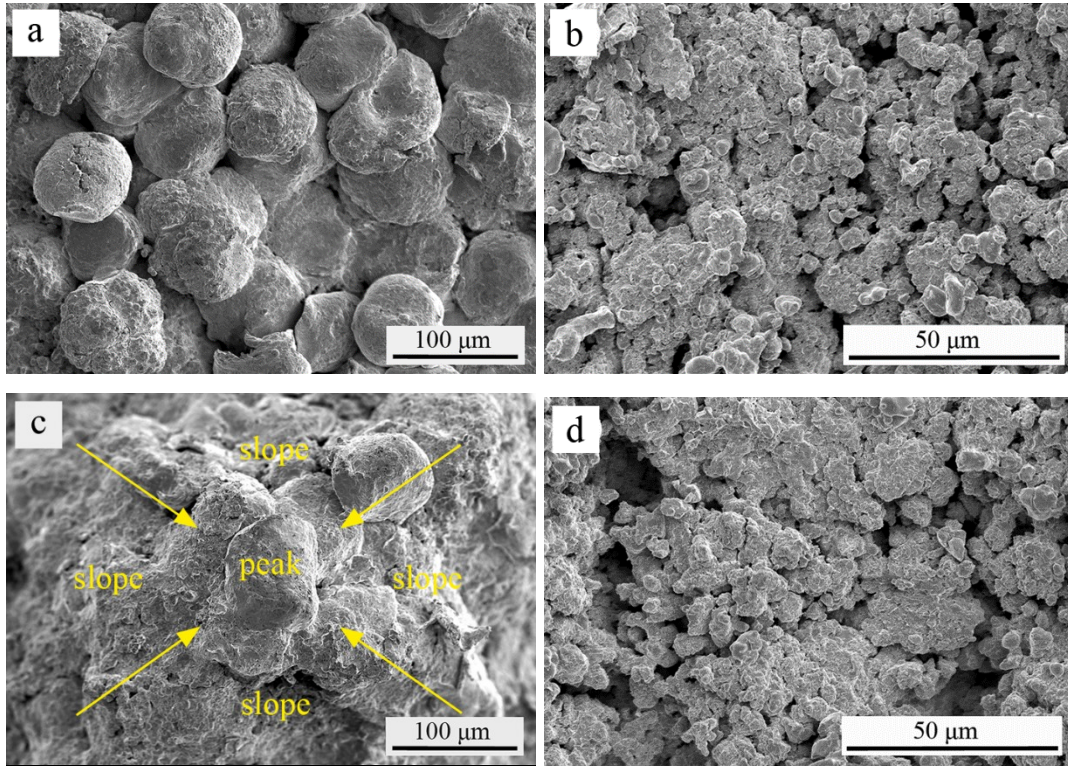
Figure 5.6- SEM images of the electrodes coated by HVOF when mesh screens were used (a) top surface of a fin, coarse mesh, (b) underneath the mesh wire, coarse mesh, (c) top surface of a fin, fine mesh, and (d) underneath the mesh wire, fine mesh.

The cross-sectional images of the coatings, shown in Figure 5.7, exhibit a good bonding between the coatings and the substrate. The fins present a lower level of porosity compared to the coatings deposited underneath the mesh wires, which are highly porous. The fin thickness was measured approximately 800 and 470 μm for the coatings deposited using coarse and fine mesh screens, respectively. The reduced thickness of the coating deposited using the fine mesh (Figure 5.7-b) is related to the higher shadowing effect of the mesh wires due to the higher wire density per unit area. In addition, the coating deposited underneath the wires of the fine mesh (Figure 5.7-b), present a higher thickness of 80 μm, which is associated with the easier material flow beneath the wires with the

smaller diameter, and thus, more deposition of the particles. The coating thickness under coarse mesh wires was measured 50 μm.
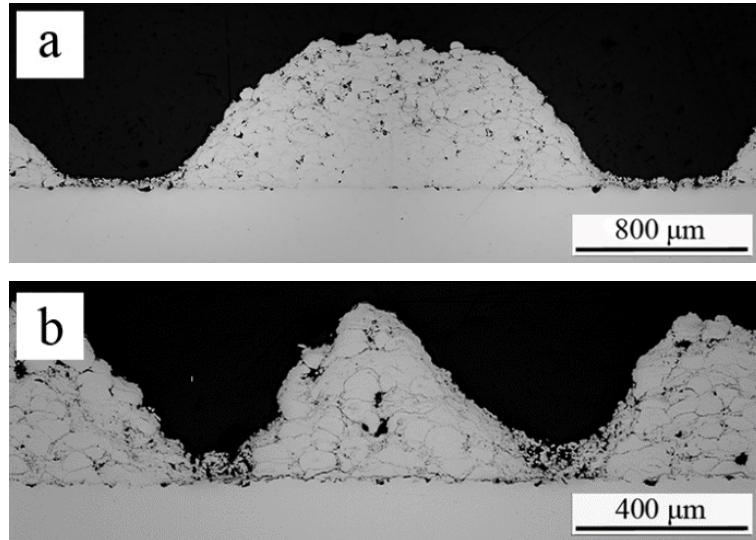
Figure 5.7- Optical microscopy cross-sectional images of electrodes when (a) coarse and (b) fine mesh screens were used.

5.3.2 Surface roughness

Figure 5.8 shows the 3-D surface topographies of the electrodes captured by CLSM for the scanned surface areas of about 3500×3500 μm^2. The average line roughness values (R_a) of the scanned surfaces, including the top of the fins, slope of the fins and underneath the mesh wires for the samples coated using mesh screens, based on 7 measurements, are presented in Table 5.2.
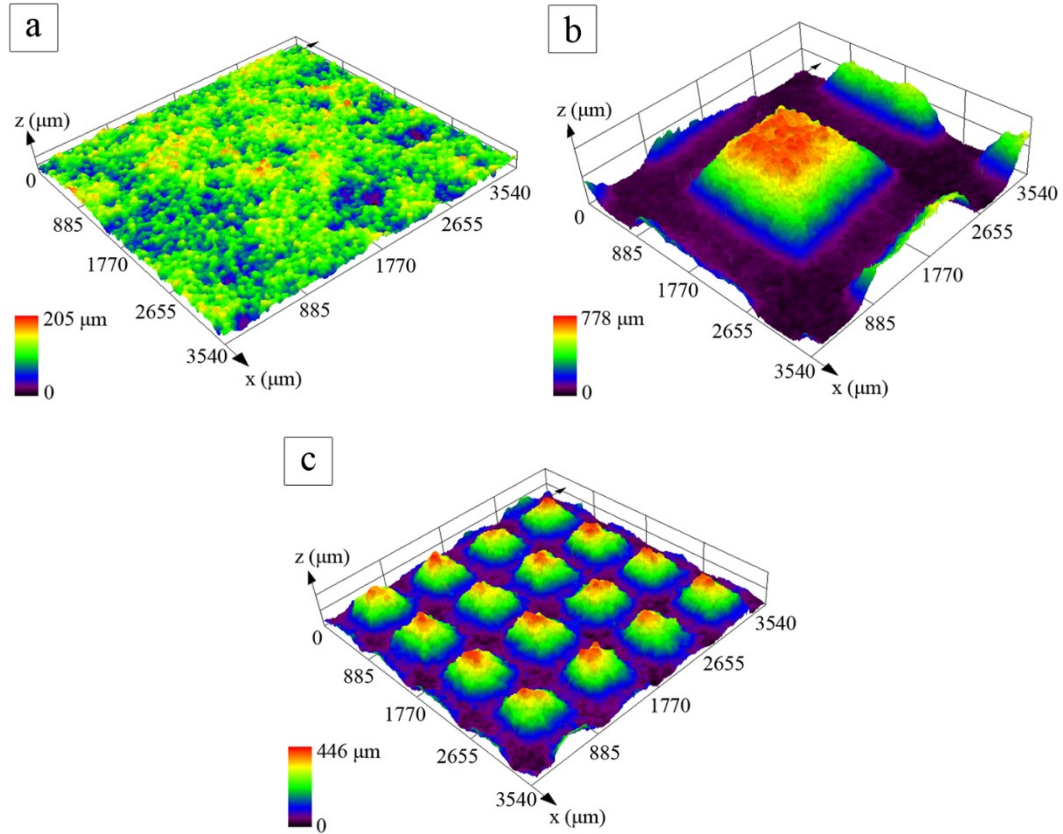
Figure 5.8- CLSM top surface topography of the HVOF coated electrodes using (a) no mesh, (b) coarse mesh, and (c) fine mesh. The average roughness for the sample coated without using mesh was measured 20.2±0.7 μm.

Table 5.2- Line roughness (R_a) values of the HVOF coated electrodes evaluated by CLSM.

Electrode	R_a (μm)		
	Top surface of the fins	Slopes of the fins	Under the mesh wires
Coarse mesh	19.7 ± 1.6	12.7 ± 2.3	6.7 ± 1.0
Fine mesh	-	10.0 ± 0.8	5.7 ± 0.5

The large variation of the surface roughness at different areas of each coating is associated with the impact and deposition of the coating particles at different impingement angles with respect to the substrate due to the formation of the fins. The influence of the spray angle on the deposition characteristics and microstructure have been investigated by

several researchers [147-150]. When no mesh was used, the majority of coating particles impact on the surface perpendicularly to form the deposition. Since a large number of the particles were partially melted or still in the solid state upon impact, the surface roughness mainly replicated the profile of the starting powder. Consequently, this sample showed the highest surface roughness value of 20.2±0.7 μm. The same mechanism applies on the top surface of the fins when coarse mesh screen was used. It is worth noting that the roughness on top of the fins formed by using the fine mesh could not be measured as only a few particles (in some cases only one particle) were deposited on the peaks. Nevertheless, on the slopes of the fins the impact direction did not remain constant and the particles hit the surface at off-normal angles, as a result, a variation of the deposition surface structure was observed. The reduced roughness values at the slopes could be attributed to the erosive effect of the unmelted particles when they impact and rebound at decreased angles on the previously deposited roughness peaks [147, 148]. For both coated samples using mesh screens, the lowest surface roughness was obtained for the area underneath the mesh wires. This could be mainly related to the penetration and deposition of fully molten particles and smaller splats under the mesh wires.

5.3.3 Electrochemical measurements

The steady-state polarization curves obtained for the HVOF coated electrodes are shown in Figure 5.9. Table 5.3 shows the apparent exchange current density, j_0, Tafel slope, b, and overpotential, η, values of the electrodes calculated based on their projected surface areas. Although larger Tafel slopes were attained for the coated electrodes compared a smooth surface nickel electrode, they showed much better catalytic activities for the HER, presented by their higher exchange current densities and smaller overpotentials. The higher activities could be attributed to their enhanced specific surface areas obtained due to the developed microstructures by the spraying process, as well as the macrostructures featured by the fins.
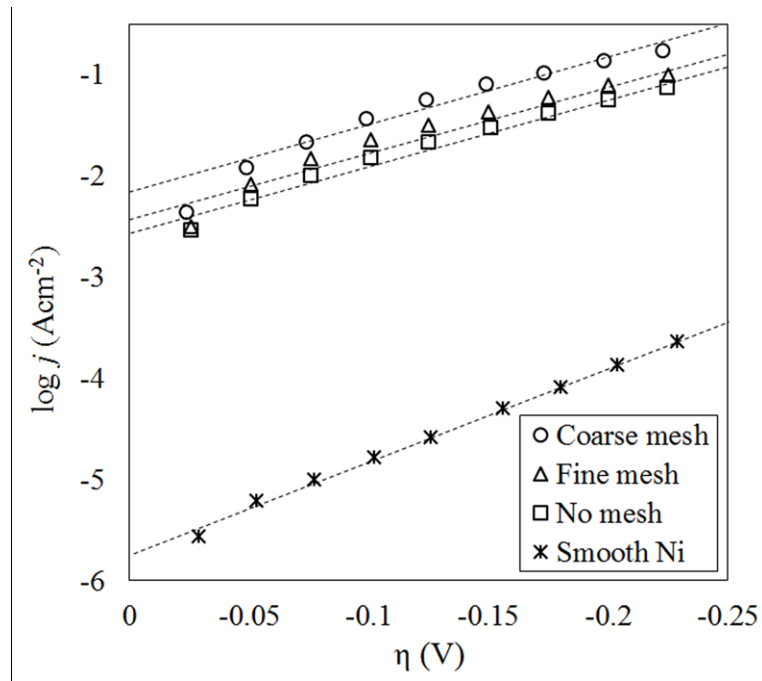
Figure 5.9- Steady-state polarization curves obtained for electrodes coated using no mesh, coarse mesh, fine mesh and a smooth nickel electrode based on their projected surface areas; j is the apparent current density.

Table 5.3- Kinetic parameters obtained from the steady-state polarization measurements based on the projected surface areas of the electrodes.

Electrode	b (mV/dec)	j_0 (A/cm^2)	η_{250} (mV)
Smooth Ni	112	2.0×10^{-6}	-724
No mesh	174	3.9×10^{-3}	-346
Coarse mesh	168	9.3×10^{-3}	-306
Fine mesh	182	6.1×10^{-3}	-354

For the electrode coated using no mesh a j_0 value of 3.9×10^{-3} A/cm^2 was obtained, which is more than three orders of magnitude higher than a smooth nickel surface. This

significant improvement of the exchange current density is related to the high roughness value achieved for this electrode. The results show that the activity was further improved when mesh screens were applied to mask the substrates. It is believed that the three-dimensional deposited surfaces engineered by formation of the fins yielded to the superior electrochemical performances. The activity was raised by increasing the mesh size, and the electrode coated using the coarse mesh was characterized as the electrode with the highest activity with j_0 value of 9.3×10^{-3} A/cm^2 and η_{250} of -306 mV.

To study the net effect of the surface roughness on the electrocatalytic activities (independent of the macroscopic structure), the apparent surfaces were corrected by inclusion of the area added by the fins as only the microscopic surface features exist. Subsequently, the steady state-polarization curves and exchange current densities were calculated for the corrected electrode surfaces, and the results are shown in Figure 5.10.
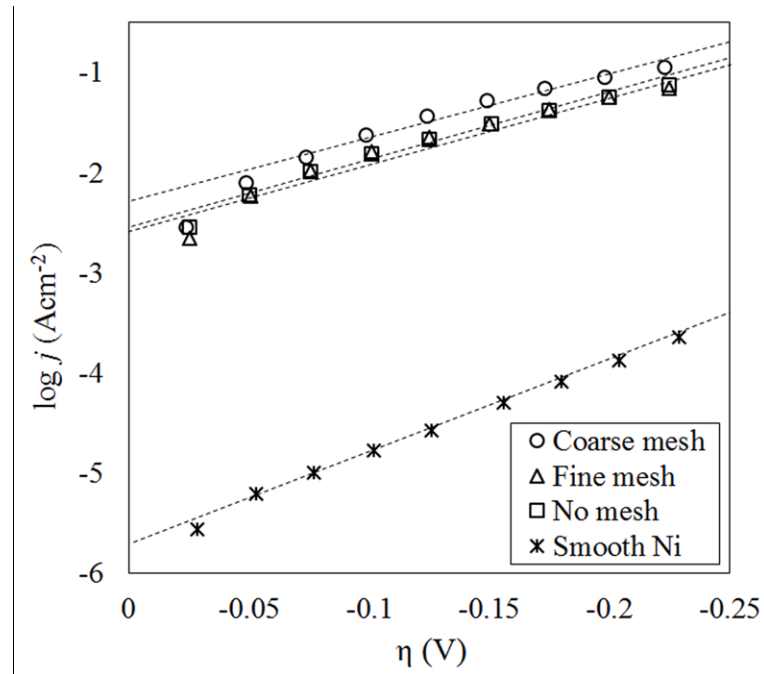
Figure 5.10- Steady-state polarization curves obtained for electrodes coated using no mesh, coarse mesh, fine mesh and a smooth nickel electrode based on their corrected surface areas; j is the apparent current density.

The exchange current densities were evaluated to be 6.7×10^{-3} and 4.1×10^{-3} A/cm^2 for the electrodes deposited using the coarse mesh and fine mesh, respectively. The results indicate that j_0 values were diminished when only the microscopic microstructure was taken into account by using the corrected surface areas for calculation of the apparent exchange current densities. The obtained j_0 values are similar for the electrodes coated using the fine mesh screen and the one coated without using mesh. This leads to the conclusion that the macroscopic surface added by the fins geometry was the main effective parameter that contributed to the enhanced electrocatalytic activity of the sample coated with the fine mesh. In addition, it is expected that the lower roughness value of this sample was compensated by the deposition of the coating particles at different impact angles on the fins, which promotes the bubble release from the surface. As a result, the available surface for hydrogen atom adsorption and desorption is increased, which leads to overall similar active surfaces per unit area for these two electrodes.

This effect is intensified for the electrode coated using the coarse mesh due to the multilevel surface roughness acquired by a combination of normal and off-normal deposition angles, induced by the shadowing effect of the thick mesh wires. Variation of the obtained microstructure for this electrode further enhances the electrocatalytic activity by providing a final larger surface area that contributes to the HER in addition to facilitation of the hydrogen gas bubble detachment from the surface. Therefore, this sample with j_0 value of 6.7×10^{-3} A/cm^2 still showed the highest activity, even when the area added by the fins was not taken into account.

These promising results show the high potential of the HVOF process for fabrication of highly electrocatalytic active electrodes for the HER. The obtained activity values are comparable to the electrode activities reported in the literature when other electrode production techniques and/or nickel alloys were used, as well as the other coating approaches investigated by the authors [27, 73, 119, 139, 142, 144, 151, 152], which further demonstrate the scalability of this process.

5.4 Conclusions

HVOF coating process was employed to manufacture electrocatalytic active nickel electrode coatings for the HER. To further increase the catalytic activity of the electrodes, their specific surface areas were enhanced by the development of three-dimensional fin arrays on their surfaces. Formation of the fin arrays was achieved by means of mesh screens, which were used to mask the surface of the substrate coupons during the coating process. When masking was not used, the deposition of unmelted and partially melted particles on the top surface was observed due to the rather low gas temperature and velocity. For the coatings produced by using mesh screens, a variety of roughness values and microstructures were obtained on the fins and underneath the mesh wires as a result of the impact and deposition of the spray particles at both normal and off-normal angles. The highest electrocatalytic activity was obtained for the electrode developed using the coarse mesh, with the apparent j_0 and η_{250} values of 9.3×10^{-3} A/cm^2 and -306 mV, respectively. This electrode still exhibited the highest activity even when the apparent surfaces were corrected by inclusion of the area added by the fins, and only the effect of the microscopic surface roughness was considered. Therefore, the high performance of this electrode was attributed to the unique microstructure with various roughness levels that were formed. Such coating structure is expected to increase the rate of the HER by providing a larger active surface area, while facilitating the detachment of the hydrogen bubbles from the surface. The obtained results indicate that the HVOF coated electrodes provide the highest electrocatalytic activity compared to other thermal spraying approaches investigated by the authors [119, 139, 144, 152].

CHAPTER 6

ARTICLE 5: Cold Spray as a Novel Method for Development of Nickel Electrode Coatings for Hydrogen Production

Maniya Aghasibeig[a], Hossein Monajatizadeh[b, 1], Philippe Bocher[b, 2], Ali Dolatabadi[a], Rolf Wuthrich[a], Christian Moreau[a]

[a]*Department of Mechanical and Industrial Engineering, Concordia University*
Montreal, QC H3G 1M8, Canada

[b]*Department of Mechanical Engineering, Ecole de Technologie Superieure*
Montreal, QC H3C 1K3, Canada

Abstract

Cold spraying process was employed as a novel method to prepare electrocatalysts for hydrogen evolution by the water electrolysis process. Three electrode coatings were developed by cold spraying of nickel powder on aluminum substrates employing different coating parameters. The effect of the electrodes surface topography, microstructure,

---

[1] Dr. Monajatizadeh assisted with the EBSD measurements and analysis of the EBSD results.

[2] Prof. Bocher assisted with the analysis of the EBSD results.

residual stress and surface strain on the electrocatalytic activity of the coatings was investigated using steady state polarization curves and electrochemical impedance spectroscopy. The results revealed that the largest electrocatalytic activity was obtained for the electrode with the lowest deposition efficiency that experienced the highest strain accumulation and compressive residual stress. It is expected that the large densities of dislocations along with a more favorable electronic structure of this coating caused by the peening effect encountered by the bounced-off particles were responsible for the higher activity of this electrode.

Keywords: Cold spray; Hydrogen evolution reaction; Peening effect; Severe plastic deformation; Electron backscattered diffraction; Residual stress

6.1 Introduction

High purity hydrogen produced by alkaline water electrolysis can be used as a green and renewable energy resource with no emissions other than water vapour when used as a fuel [1, 2]. In a basic water electrolysis process, a direct current passes through cathode and anode electrodes placed in a conductive electrolytic solution and decomposes water into hydrogen and oxygen [1]. Hydrogen evolution reaction (HER) starts with the discharge of a water molecule (Volmer step, Eq. 6.1) followed by either electrochemical desorption (Heyrovsky step, Eq. 6.2) or chemical recombination (Tafel step, Eq. 6.3) depending on the hydrogen-metal bond strength:
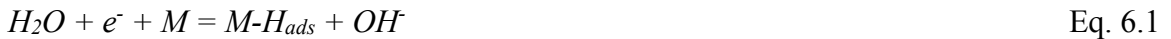
$H_2O + e^- + M = M\text{-}H_{ads} + OH^-$ Eq. 6.1

$M\text{-}H_{ads} + H_2O + e^- = H_2 + OH^- + M$ Eq. 6.2

$2M\text{-}H_{ads} = H_2 + 2M$ Eq. 6.3

High energy consumption of the electrolysis process has made large scale hydrogen production by this method economically unattractive [1-4]. However, the energy efficiency of water electrolysis can be improved by reducing the hydrogen and oxygen evolution overpotentials that contribute significantly to cell energy losses [3-6].

Using highly intrinsically active electrode materials reduces the internal voltage losses and increases the efficiency of the HER [6-9]. Nickel is one of them and is widely used as the electrode material for alkaline water electrolysis due to its high electrocatalytic activity, availability, stability in alkaline solutions, and relatively low cost [8-12]. Apart from material selection, the physical morphology of an electrode has also a significant influence on the overpotential, and thus, on its electrocatalytical performance. A larger effective electrode surface adds to the reaction area by providing more electrode-electrolyte interface, reducing the operating current density, and contributing to a higher electrocatalytic activity [9, 13, 14]. The surface area can be enhanced by increasing the electrode surface asperities, such as surface roughness and porosity.

Furthermore, surface crystallography of an electrode substantially affects its electrocatalytic behaviour. Enhanced performance of nanocrystalline catalysts for the HER as a result of high volume fraction of surface defects has been extensively discussed in the literature [15-20]. Improved electrocatalytic activities of nanostructured materials could be attributed to their favourable electronic structure generated due to the increased amounts of atoms located at interfaces between adjacent grains, which are likely to be out of equilibrium [18, 20]. These surface properties depend strongly on the technique used to prepare the electrode surface. The possibility to deposit coatings with minimal oxidation and ultrafine microstructures due to severe plastic deformation makes cold spraying a promising technique for producing active electrode coatings for electrochemical processes in general and alkaline water electrolysis in particular.

Cold spray, invented in the mid-1980s, has been the object of intensive development over the last 20 years. This thermal spraying technique permits deposition of coatings in an all-solid-state process [21, 22]. In a cold spray process, solid powder particles (typically 1 to 50 μm in diameter) are accelerated toward a substrate at high velocities by a supersonic jet of compressed gas that has been cooled down to temperatures close to room temperature, well below their melting point. The compressed gas is generally nitrogen, air, or helium flowing through a converging-diverging nozzle. Consequently, upon impact, the particles experience plastic deformation and shear instability at the interface with the substrate or the already deposited layers. This also causes disruption and removal of the oxide films from the surfaces of both substrate and particles, and promotes the bonding by

providing an intimate contact between them. Finally, they mechanically bond to the substrate and form a three-dimensional coating having a good bond and cohesion strength [21, 23-25]. For the particles to deposit on the substrate, their velocity upon impact needs to be higher than a so-called critical velocity, which depends on the material, size and morphology of the particles. Generally, the particle impact velocity increases by increasing the temperature and pressure of the propellant gas and by reducing the particle diameter [22, 26-29].

Since the gas temperature decreases rapidly upon acceleration, the temperature of the spray particle stays relatively constant close to room temperature, and neither oxidation nor phase transformation occur in the in-flight particles [26, 30]. As-sprayed coatings are generally in compression due to the impingement of the spraying particles on the surface at high velocities inducing peening effect [30]. A schematic view of a cold spray system is depicted in Figure 6.1.
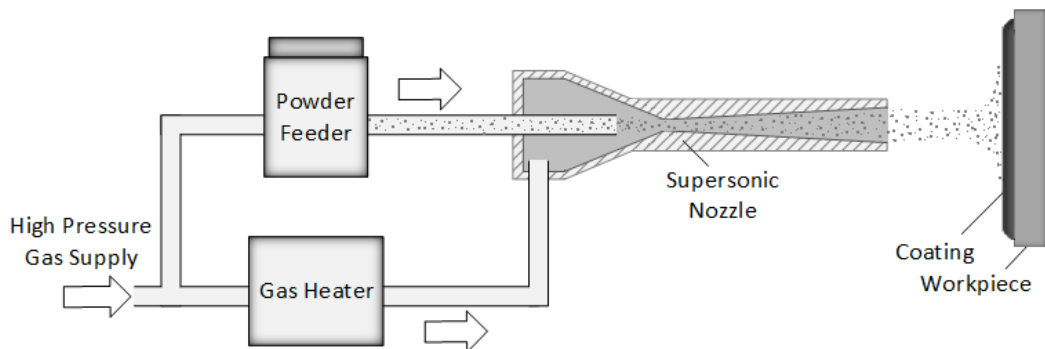
Figure 6.1- Schematic view of a cold spray system.

The present study investigates the possibility of developing electrocatalytically active electrode coatings by cold spray and studies the electrochemical properties of the produced electrodes. The effect of cold spraying parameters on microstructure and electrochemical activity of the developed electrodes was studied. Steady state polarization curves and electrochemical impedance spectroscopy (EIS) measurements were used to examine the electrocatalytic activity of the coated nickel electrodes towards HER. The best

coating conditions were determined for development of the electrode with the highest electrocatalytic activity.

6.2 Material and methods

6.2.1 Cold spray process

Commercially available gas atomized nickel powder (Metco 56C-NS) was used as feedstock powder to produce cathode electrode coatings on aluminum (Al 6061) substrates. The particle size distribution of the powder was measured with a laser diffraction particle analyzer (Malvern Instrument's Spraytec) using a 300 mm lens. Figure 6.2 illustrates the measured particle size distribution that ranges from 45 to 95 μm. The distribution widths of D10, D50, and D90 were measured to be 54, 66, and 78 μm, respectively.
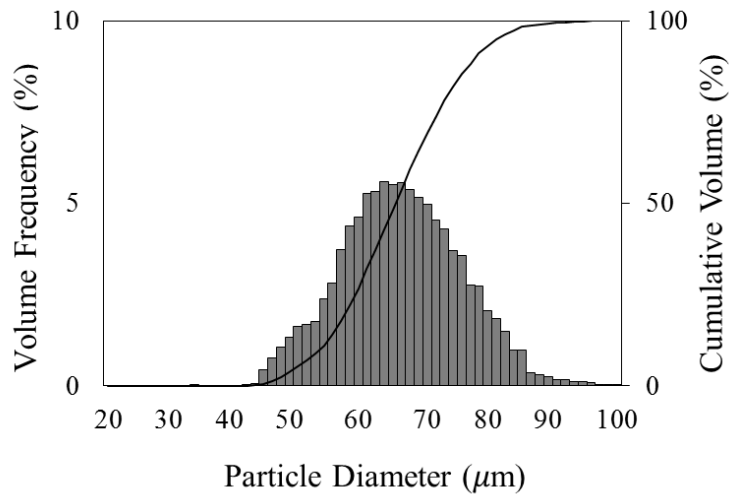
Figure 6.2- Particle size distribution of the Metco 56C-NS nickel powder used for cold spraying.

The as-received morphology and cross-sectional SEM images of the atomized nickel powder are shown in Figure 6.3-a and b, respectively. As shown in the figures, the powder particles were spherical with a dense structure containing nearly no porosity. Table 6.1

provided by the powder manufacturer shows the nominal chemical composition of the powder determined using an Inductively Coupled Plasma (ICP) system.
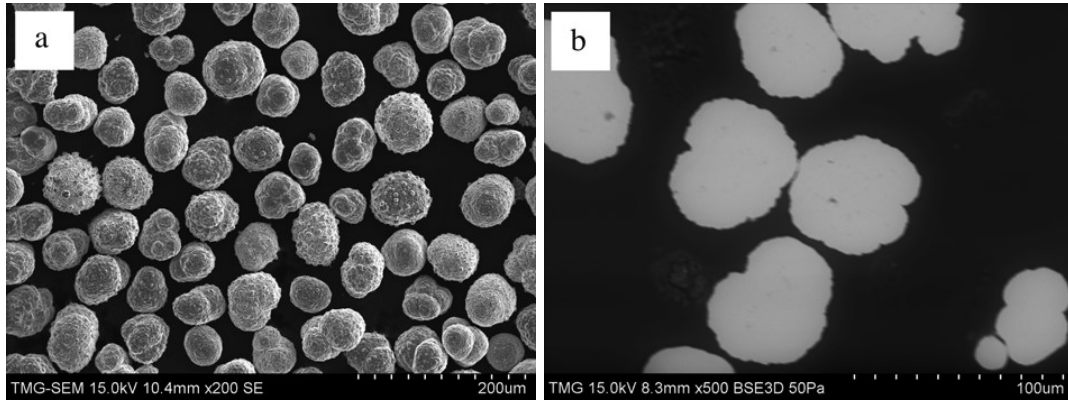
Figure 6.3- SEM images of the Ni powder (a) morphology, and (b) cross-section.

Table 6.1- Chemical composition of Metco 56C-NS nickel powder (wt. %).

B	C	Co	Cu	Fe	Ni	S
0.01	0.04	0.06	<0.01	<0.01	99.9	0.02

To study the effect of the temperature and pressure of the propellant gas on the structure and electrocatalytic activity of the electrodes, three cold sprayed samples were deposited according to the spray conditions displayed in Table 6.2. Coatings were produced by Plasma Giken (Webster Massachusetts, USA) with their Model PCS-1000 cold spray system. In all experiments, two passes were deposited using nitrogen as the propellant gas, at 25 mm standoff distance, 50 g/min powder feeding rate, and 300 mm/s gun traverse speed.

Table 6.2- Propellant gas temperatures and pressures used in the cold spraying experiments.

Electrodes	Propellant gas Temperature (°C)	Propellant gas Pressure (MPa)
C1	800	5
C2	1000	5
C3	1000	3

6.2.2 Coating characterization

For metallographic studies, as-sprayed samples were sectioned perpendicular to the coating surface using a low speed precision cut-off machine and then cold mounted. Subsequently, the samples were ground and polished according to the conventional metallographic procedures up to 0.05 μm diamond suspension surface finish. The cross-section of the samples was then studied by optical microscopy. A Hitachi S-3400N scanning electron microscope (SEM) operating at 15 kV was used to evaluate the top surface morphology of the coatings as well as the morphology of the feedstock powder. Three-dimensional surface topography, surface roughness and specific surface area of the electrodes were evaluated by a 3D Confocal Laser Scanning Microscope (CLSM) (Olympus, LEXT-OLS4000) with a resolution of 10 nm in the z direction and 120 nm in the xy plane.

Residual stress measurements were performed at 7 different points on the top surface of the coatings, using a PULSTEC X-ray machine specified for residual stress measurement through Cosα method [31] operated with Cr Kα radiation, at 2θ value of 156 degrees, and wavelength of 0.2291 nm.

In order to characterize the microstructure of the deposited layers near the top surface of the coatings, electron backscattered diffraction (EBSD) technique was used. The sample surfaces for EBSD were produced by vibratory polishing of the metallographically prepared sections for 24 h using colloidal silica suspension. The EBSD observations were performed at 9 different areas of the cross-section near the top surface of each coating using

a SU-70 Hitachi FE-SEM equipped with a HKL® camera and software for EBSD operated at an accelerating voltage of 15 kV.

Phase analysis of the powder and the coated electrodes was performed by X-ray diffraction (XRD, X'Pert Pro; PANalytical) with Cu Kα radiation and 2θ values ranging from 10° to 90°. In order to analyze the detected patterns the Pearson's Crystal Data (PCD)-crystal structure database for inorganic compounds was used.

6.2.3   Electrochemical characterization

Electrochemical characterization of the electrodes was carried out using a three compartment Pyrex glass cell and a Stanford Research Systems potentiostat (Model EC301). In this setup, the cold sprayed samples were used as the working electrode, a Pt wire as the counter electrode and a saturated Hg/HgO electrode (-0.924 V vs. Hg/HgO) as the reference electrode. All measurements were performed in a 1 M NaOH electrolytic solution bubbled with nitrogen at 22 °C. Tafel curves were registered at a scan rate of 50 mV/s in the current range of 10 μA to 100 mA after 1800 s pre-polarization at -1.6 V vs. Hg/HgO. The electrocatalytic activity of the electrodes, evaluated from the corresponding kinetic parameters (apparent exchange current density j_0 and Tafel slope b) was derived from extrapolation of the linear part of the Tafel curve to the equilibrium potential.

Electrochemical Impedance Spectroscopy (EIS) measurements were performed in the frequency range of 50 mHz to 5 kHz using an Autolab potentiostat/ galvanostat/ frequency response analyzer (FRA) (model PGSTAT30) controlled by Autolab General Purpose Electrochemical System (GPES) and FRA software packages. Same as the Tafel measurements, the surface nickel oxides present on the coatings were removed by pre-polarization of the electrodes at -1.6 V vs. Hg/HgO for 1800 s. Subsequently, the EIS measurements were conducted at four different electrode potentials of -1.1, -1.05, -1, and -0.95 V. To analyze the impedance data, a simplified one-constant phase element (CPE) electrical model, shown in Figure 6.4, was used as the equivalent circuit to fit the experimental impedance data. In this model, a solution resistance, R_s, is in series with the parallel connection between a CPE and a charge transfer resistance, R_{ct}. This model is often used when only one semicircle is experimentally observed on the complex plane plots of

the nickel-based electrodes [32-36]. The theory of the HER and detailed definition of the circuit elements can be found in the provided references [33, 35, 37].
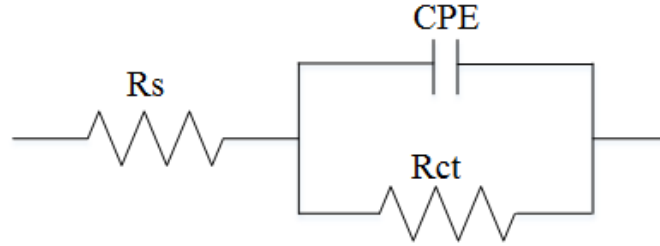
Figure 6.4- 1-CPE equivalent circuit used for the HER.

The CPE is generally used as a replacement to the double layer capacitance to explain the results obtained for solid electrodes. Impedance of the CPE is described by Eq. 6.4 [38].

$$Z_{CPE} = \frac{1}{T \, (j\omega)^\phi} \qquad\qquad \text{Eq. 6.4}$$

where ω represents the angular frequency, T is a capacitive parameter related to the double layer capacitance, and ϕ with a value between 0 and 1 describes the phase angle of the CPE. Double layer capacitances (C_{dl}) of the electrodes were then calculated according to Eq. 6.5, using the EIS results [38].

$$T = C_{dl}^\varphi \, (R_s^{-1} + R_{ct}^{-1})^{1-\varphi} \qquad\qquad \text{Eq. 6.5}$$

6.3 Results and discussion

6.3.1 Morphological study of the coatings

Figure 6.5 displays the cross-sectional micrographs of the three cold sprayed samples. Comparison of the coatings shows the thickness varies from one coating condition to the next. The average thickness of C1 coating was measured to be 200 μm. C2 with about 450

μm, and C3 with approximately 70 μm exhibited the highest and the lowest coating thicknesses, respectively.
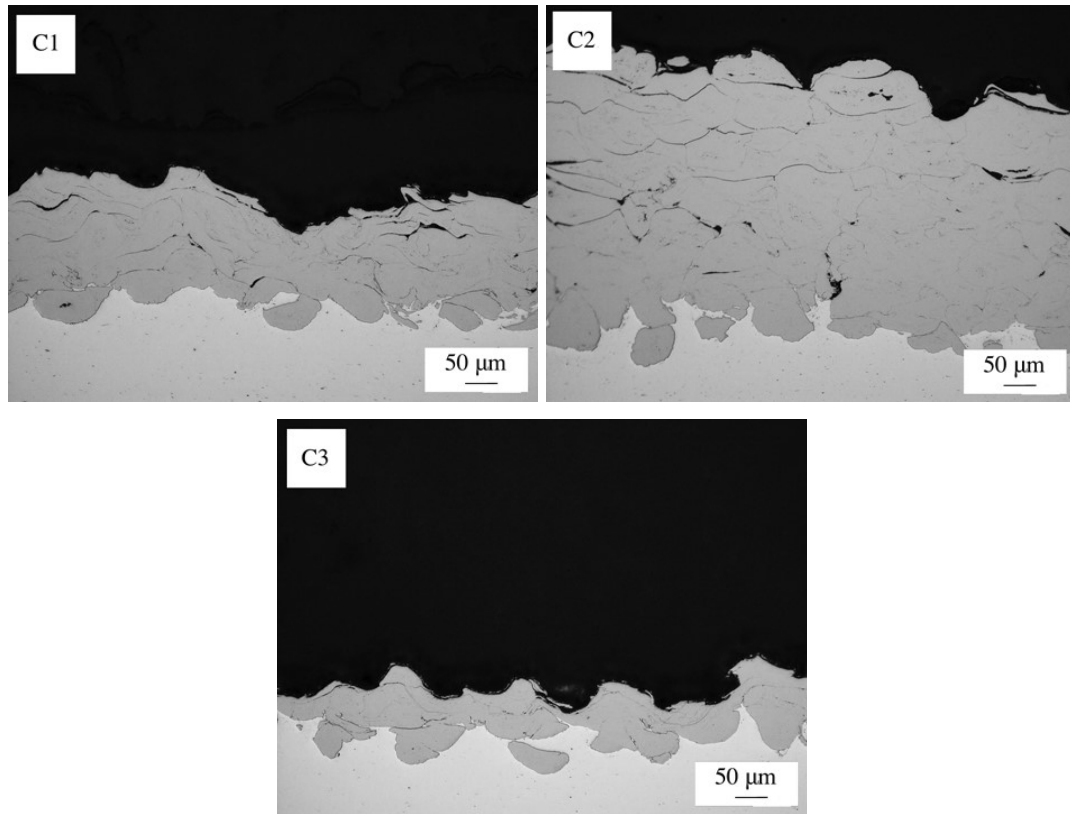
Figure 6.5- Cross-sectional SEM images of C1, C2, and C3 electrode coatings.

The variation of the coating thickness can be explained by the impact particle velocity. Higher thickness of C2 coating can be related to the maximum temperature and pressure that were used during spraying (1000 °C and 5 MPa). For this coating, the particles experienced a higher velocity, underwent larger plastic deformation upon impact on the substrate and formed a better bonding with the adjacent particles and the substrate. Decreasing the propellant gas temperature to 800 °C in C1 coating led to a reduced particle impact velocity, and thus, a lower deposition efficiency and thickness were obtained. The lowest coating thickness was achieved for electrode C3 (about 10 μm in some regions) and it may be attributed to the lower particle deformation and lack of bonding between the

103

adjacent nickel particles due to lower particle velocities obtained when the gas pressure was reduced to 3 MPa.

Study of the coating/substrate interfacial regions in the figure suggests that the initial bonding mechanism for forming the first coating layer was due to mechanical interlocking of the impinging particles and the substrate. Since the hardness of nickel particles was much higher than the aluminum substrate, it can be assumed that the initial bonding has been achieved by ploughing the colliding precursor particles into the substrate. Once the first coating layer was deposited, the substrate properties eventually evolved from soft Al to harder Ni. Thus, the built up mechanism of the subsequent coating layers was based on the kinetic energy of the particles and their severe plastic deformation upon impact. As a result, it was more difficult for the subsequent coating layers to deposit when particles stroke on the deposited material with a higher hardness.

For electrode C3, it is expected that the velocity of the subsequent particles colliding on the first deposited nickel layer was below the critical velocity needed for bonding. Consequently, the impinging particles rebounded and did not contribute to the deposition. Nevertheless, the bounced-off particles abraded the contact surface, while they introduced high values of plastic deformation on the deposited particles when impacting on the surface. This mechanism can be regarded as the peening effect introduced by the bounced-off nickel particles at low-pressure condition.

Top surface SEM images of the coatings shown in Figure 6.6 confirm the aforementioned hypothesis: most of the particles deposited on the top surface of electrode C2 retained the granular morphology of the starting powder, whereas the majority of particles were severely deformed and craters were formed on the top surface of C3 coating as a result of the peening effect. For C1 coating, a combination of granular particles and craters could be observed on the top surface.
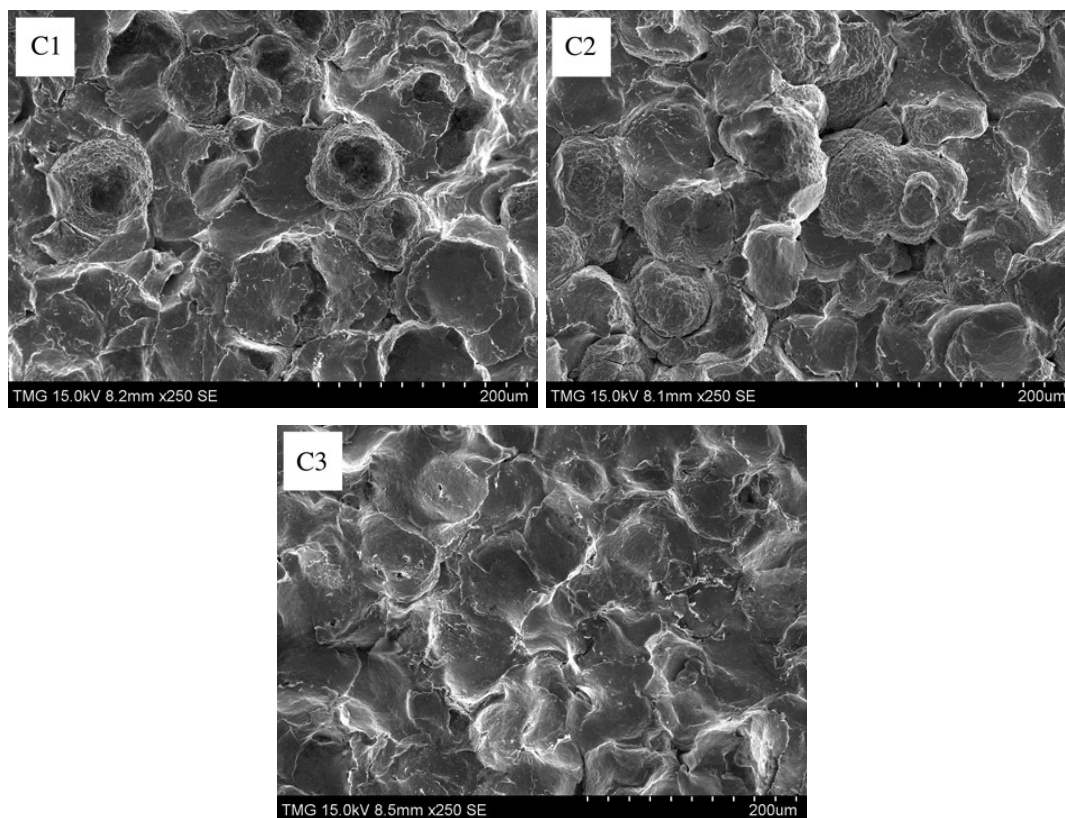
Figure 6.6- Top surface SEM image of C1, C2, and C3 electrode coatings.

6.3.2 Surface roughness measurements

3D surface topographies of the coated electrodes captured by CLSM for scanned surface areas of 2100*2100 μm^2 are illustrated in Figure 6.7. The average surface roughness data (S_a) based on the scanned 3D surfaces of the corresponding electrode coatings are presented in Table 6.3. The results indicate that C1 had a roughness value of 18.1 μm, while C2 with 22.3 μm had the largest, and C3 with 14.2 μm had the smallest roughness values.

Surface ratio of the electrodes, which is the ratio between the specific and the projected surface areas, is also shown in Table 6.3. Electrodes C2 and C3 with surface ratios of 4.83 and 2.93 exhibit the largest and the smallest specific surface areas, respectively. A direct correlation between the specific surface areas, surface roughness values and the deposition efficiencies can be observed. As shown in the SEM images in Figure 6.6, most of the particles deposited on the surface of electrode C2 retained the granular morphology of the precursor powder, and the roughness of the surface reproduced

105

mainly the profile of the starting powder particles. Thus this sample exhibited the highest specific surface area and surface roughness values. For C3 coating, the impacting particles could not bond to the first deposited layer due to the low pressure. Instead, each individual impact shot-peened the surface and the bounced-off particles caused more flattening, plastic deformation and densification of the deposited layer, hence lower surface roughness and specific area were achieved. For C1 electrode coating, it seems that the smaller particles could accelerate due to their lower inertia and bonded to the surface while the particles with larger diameters could not reach the sufficient velocity required to promote their bonding upon impact. Therefore, the surface of this coating was comprised of a combination of rough granular protrusions and flattened particles, as shown in Figure 6.6. Accordingly, intermediate surface area and roughness values were obtained for this sample.
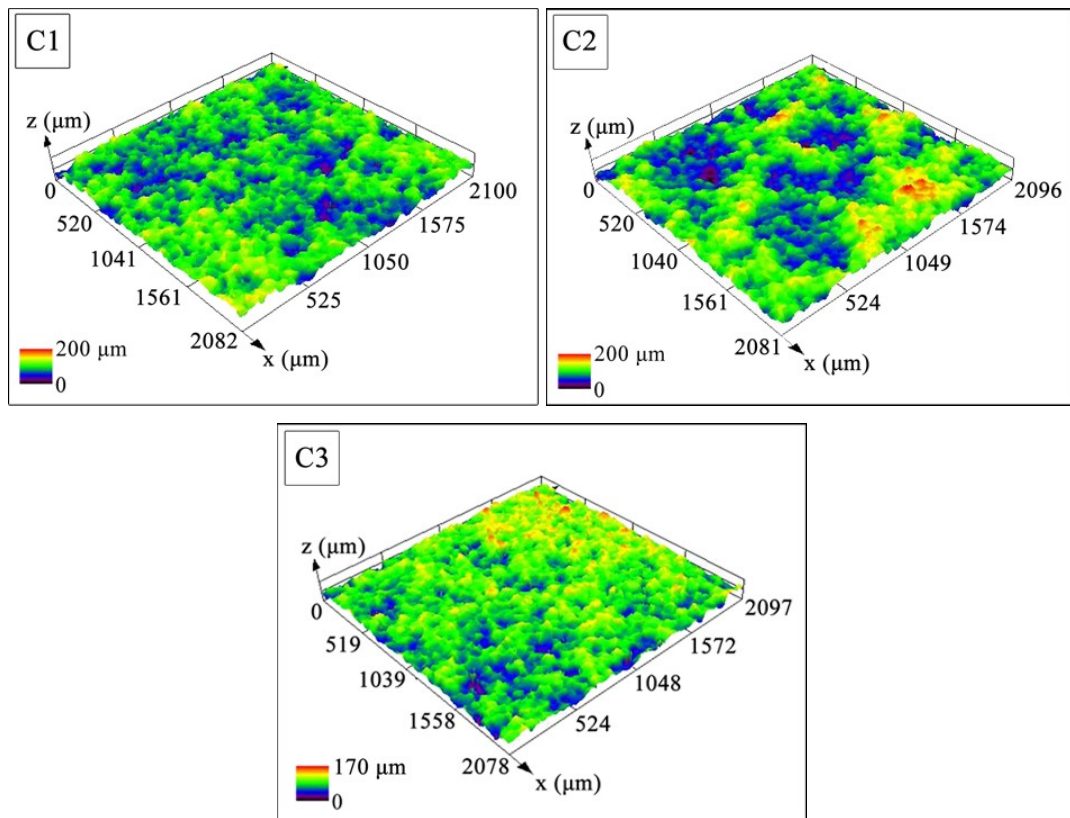
Figure 6.7- CLSM top surface topography of electrodes C1, C2, and C3.

Table 6.3- Surface roughness (S_a) of electrodes C1, C2, and C3 evaluated by CLSM.

	C1	C2	C3
S_a (µm)	18.10	22.31	14.21
Surface ratio	3.14	4.83	2.93

6.3.3   Residual stress measurements

Residual stresses were evaluated parallel to the substrate and the results are shown in Figure 6.8. It is worthy to mention that as the X-ray wavelength used to measure the residual stress was relatively long, the penetration depth of X-ray was expected to stay in the range of few microns. Therefore, the values of the residual stresses represent mainly the top surface of the coatings. The results are the average of 7 measurements on each sample and the error bars show their standard deviations.

It can be seen that all the stress values are negative or compressive induced by the impacting particles. The maximum residual stress was observed in C3 and the minimum in C2 at -175±10 MPa, and -121±6 MPa, respectively. The magnitude of the stress values could be related to the coating thickness (Figure 6.5) and plastic deformation (Figure 6.6): the lower the coating thickness, the higher the plastic deformation and the residual stress. This could be explained by the peening effect of the impinging particles on the final deposited ones on the surface of each coating. As all specimens experienced almost the same spray time and number of spray particles during the coating process (same powder feed rate, number of passes and torch speed), it is rational to imagine that the lower thickness coatings were more significantly affected by the constant peening effect although they had a smaller coverage density. This effect led to a more intense deformation, and thus, a greater residual stress was obtained in the finer coating layers for a given deposition time.
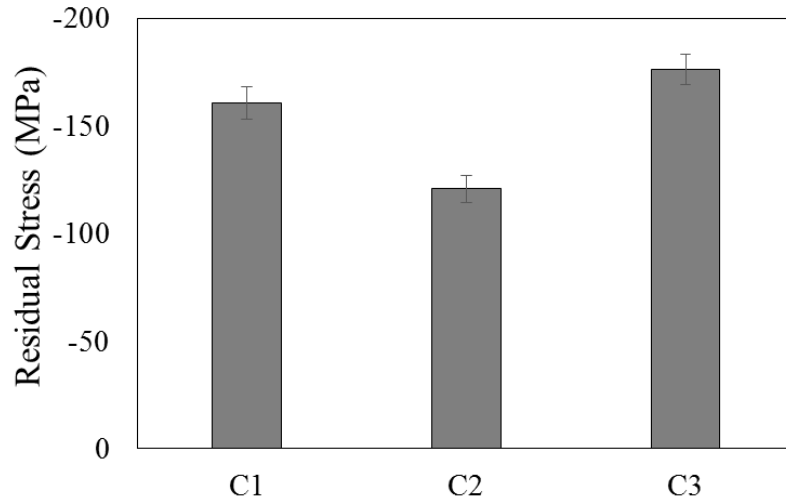
Figure 6.8- Compressive residual stress evaluated from 7 measurements on each C1, C2, and C3 cold sprayed coatings, and the error bars show their standard deviations.

6.3.4 EBSD measurements

Electron back scattered diffraction orientation maps were measured on vibro-polished cross-sectional surfaces for each sample. Graphical results are shown in Figures 9-a to c. The maps present the size of the grains near the top surface of the coatings, measured using a step size of 20 nm. Size of the grains in the precursor powder was also measured by EBSD at the step size of 50 nm, and it is presented in Figure 6.9-d. The colors in the maps, which are coded according to the color key legend, show the crystallographic orientation of each area relative to the normal direction of the coatings surface. High angle grain boundaries (>10) are shown by thick black lines, while low angle grain boundaries (2<X<10) are shown by the thin lines.

A crystalline structure composed of a large number of sub-micron and ultrafine grains can be observed in all coating layers. The grains interiors seem to be relatively clean with a low density of sub-grain boundaries compared to the precursor powder, as shown in Figure 6.9. This small fraction of sub-boundaries could be related to the ultra-fine sizes of the grains, which could be the result of dynamic and/or metadynamic recrystallization process. In all coated samples, grains with sizes as small as 20 nm could be detected.
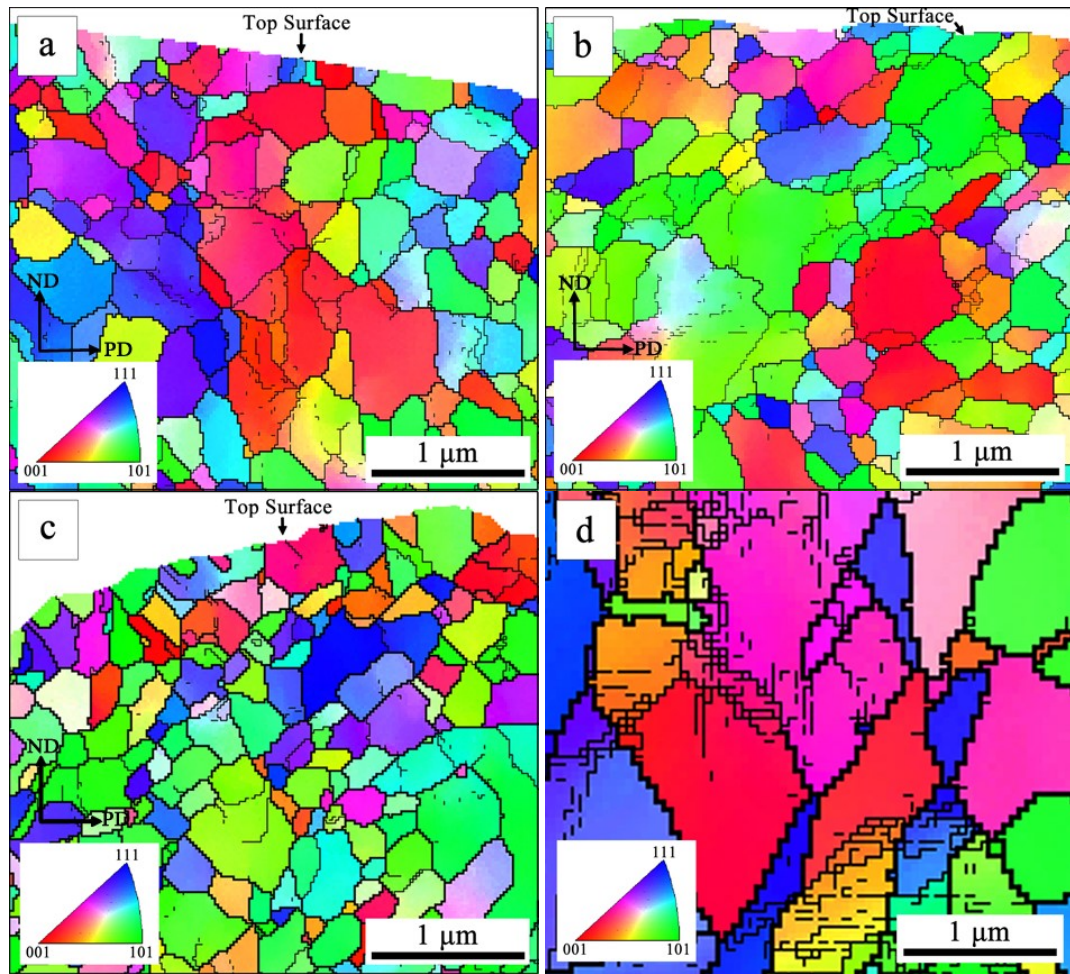
Figure 6.9- EBSD characterization of the cross-sections close to the top surface of the as-sprayed (a) C1, (b) C2, and (c) C3 coatings at the step size of 20 nm; and (d) precursor powder at the step size of 50 nm, (ND: normal to the peening direction, and PD: perpendicular to the peening direction).

By EBSD analysis of a larger fraction of the coating surfaces, the average grain size at the very last 1 μm depth near the top surface of C1, C2, and C3 coatings was evaluated to be 259±4, 300±8, and 242±6 nm (standard error), respectively. For the same scanned areas, the density of the grain boundaries was measured to be 254±6, 246±5, and 268±4 pixels $μm^{-2}$ (standard error) for C1, C2 and C3 coatings, respectively. Formation of sub-micron and ultrafine grains at the top surface of the coatings can be explained by peening effect of the bounced-off particles during the cold spraying process. It is believed that impingement of nickel particles, imposed intensive plastic deformation and introduced a large density of dislocations to the grains at the top surface of the coatings. This led to the formation of non-equilibrium grain boundaries, excessive grain refinement and creation of

109

sub-micron/ultrafine grain structures [39, 40]. Formation of the fine grains as a results of the peening effect and high strain rate deformation can generally be seen at impacting particle/particle interface in cold sprayed coatings [41-44].

To examine any possible effect of crystallographic orientation on the electrocatalytic activity, pole figures and inverse pole figures obtained from different areas of top surfaces of the coatings were investigated. The results proved that there is no preferred orientation as the inverse pole figures had a low intensity factor (2.05, 1.40, and 1.49 for the electrodes C1, C2, and C3, respectively).

6.3.5   X-ray diffraction

Prior to the electrocatalytic measurements, XRD patterns of the as-sprayed coatings were obtained from several areas of each sample. The patterns were then compared to the pattern of the starting powder to ensure that the aluminum substrate was fully coated by the nickel powder without any bare areas that might affect the electrochemical results, specifically for electrode C3, which had a very thin coating layer. As shown in Figure 6.10, similar nickel patterns were obtained for all coatings and no aluminum peaks could be detected.
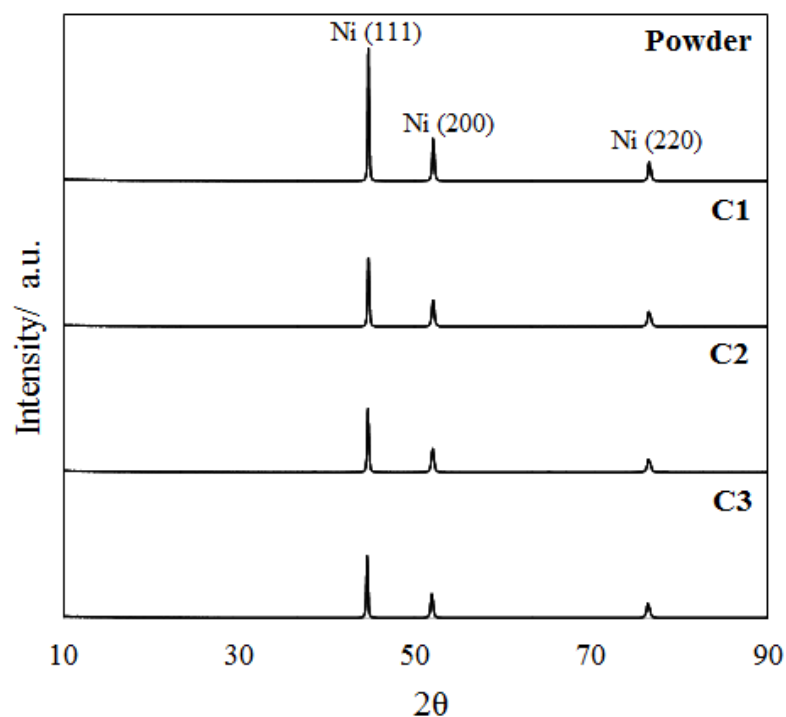
Figure 6.10- XRD pattern of the cold sprayed coatings and the precursor nickel powder.

6.3.6 Electrochemical characterization

6.3.6.1 Tafel plots

Figure 6.11 shows the steady state polarization curves normalized to the geometrical surface area of the cold sprayed electrodes compared to a smooth nickel wire. The apparent exchange current density j_0 and Tafel slope b, derived from the linear part of the Tafel plots, are summarized in Table 6.4.

Higher activity of the cold sprayed samples is indicated by their higher apparent exchange current densities. The results show that the apparent exchange current density of all samples was greatly increased compared to a smooth nickel sample. Electrode C3 appears to be the best overall electrocatalyst with a j_0 value of 3.41×10^{-4} A cm^{-2}. The corresponding values were 1.36×10^{-4} A cm^{-2}, and 1.06×10^{-4} A cm^{-2} for electrodes C1 and C2, respectively.

111
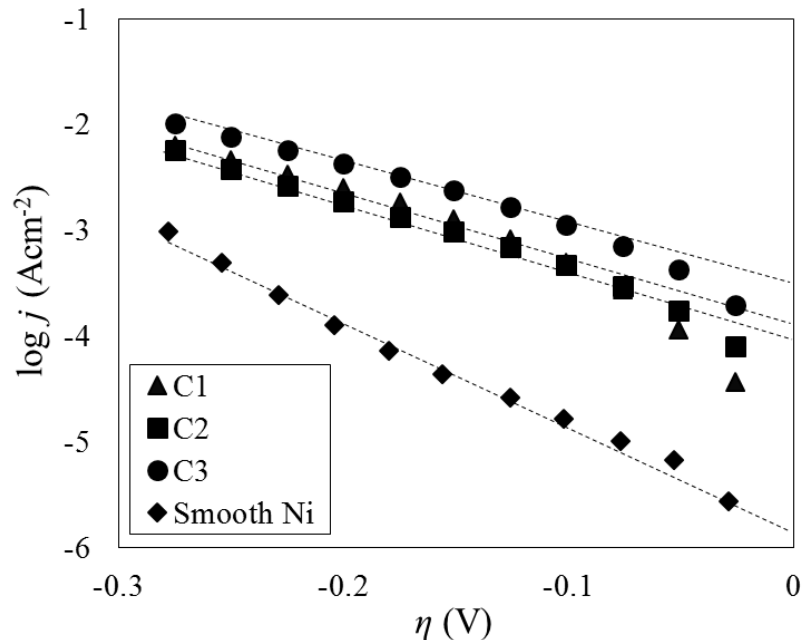
Figure 6.11- Steady-state polarization curves of the cold sprayed C1 to C3 samples, and a smooth nickel wire obtained in 1M NaOH.

Table 6.4- Kinetic parameters of the C1 to C3 cold sprayed samples, and smooth nickel wire for the HER in 1M NaOH solution.

Electrode	b (mV dec^{-1})	j_0 (A cm^{-2})
C1	166	1.36×10^{-4}
C2	159	1.06×10^{-4}
C3	186	3.41×10^{-4}
Smooth Ni	101	1.48×10^{-6}

As mentioned earlier, the electrocatalytic activity of an electrode is highly related to its active surface area. Based on the specific surface area and surface roughness values obtained by CLSM (Table 6.3), it was expected for the electrode C2, with the largest specific surface area, to have the best electrocatalytic activity for the HER. However, the results indicated that there was a reverse correlation between the surface area and the electrocatalytic activity of these electrodes.

112

Since almost similar average grain sizes and grain boundary densities could be detected in all three coatings, as illustrated earlier in EBSD results, other features need to be regarded as the main factors that explain this disagreement, and cause the different activities between the electrodes. Here, the density of dislocations could be considered as one of the factors that explains the variation of activities. For electrode C3 that experienced more severe plastic straining, a larger density of dislocations that are randomly arranged inside the grain interiors with sizes larger than 100 nm could be expected [45].

In addition, higher activity of electrode C3 could also be attributed to the change of its electronic structure, and modification of reactivity induced by the compressive stress. Chemisorption energies for surface reactions considerably change in strained surfaces, caused by shifting of the position of the center of metal d bands, and modification of the band width [46, 47]. It is possible that the larger strain in C3 coating significantly shifted the d states on the surface atoms relative to the Fermi level, and thus, the ability of this surface to form bonds to the adsorbed hydrogen atoms.

6.3.6.2   Electrochemical impedance spectroscopy (EIS)

EIS data of the cold sprayed electrodes were also acquired to corroborate the Tafel results for the electrocatalytic activity measurements, and their complex plane plots and phase-angle Bode plots obtained at different overpotentials are displayed in Figure 6.12. Table 6.5 shows the values of the circuit elements obtained by 1-CPE model (Figure 6.4) for each electrode.

The results in Figure 6.12 show that only one semicircle was present at each overpotential for the whole frequency range of all electrodes. It is shown in the literature that this behaviour represents the electrode coatings containing shallow and wide pores [32, 48]. The fitted data in this figure also shows that good approximations to the experimental data were attained when the 1-CPE model presented in Figure 6.4 was used.
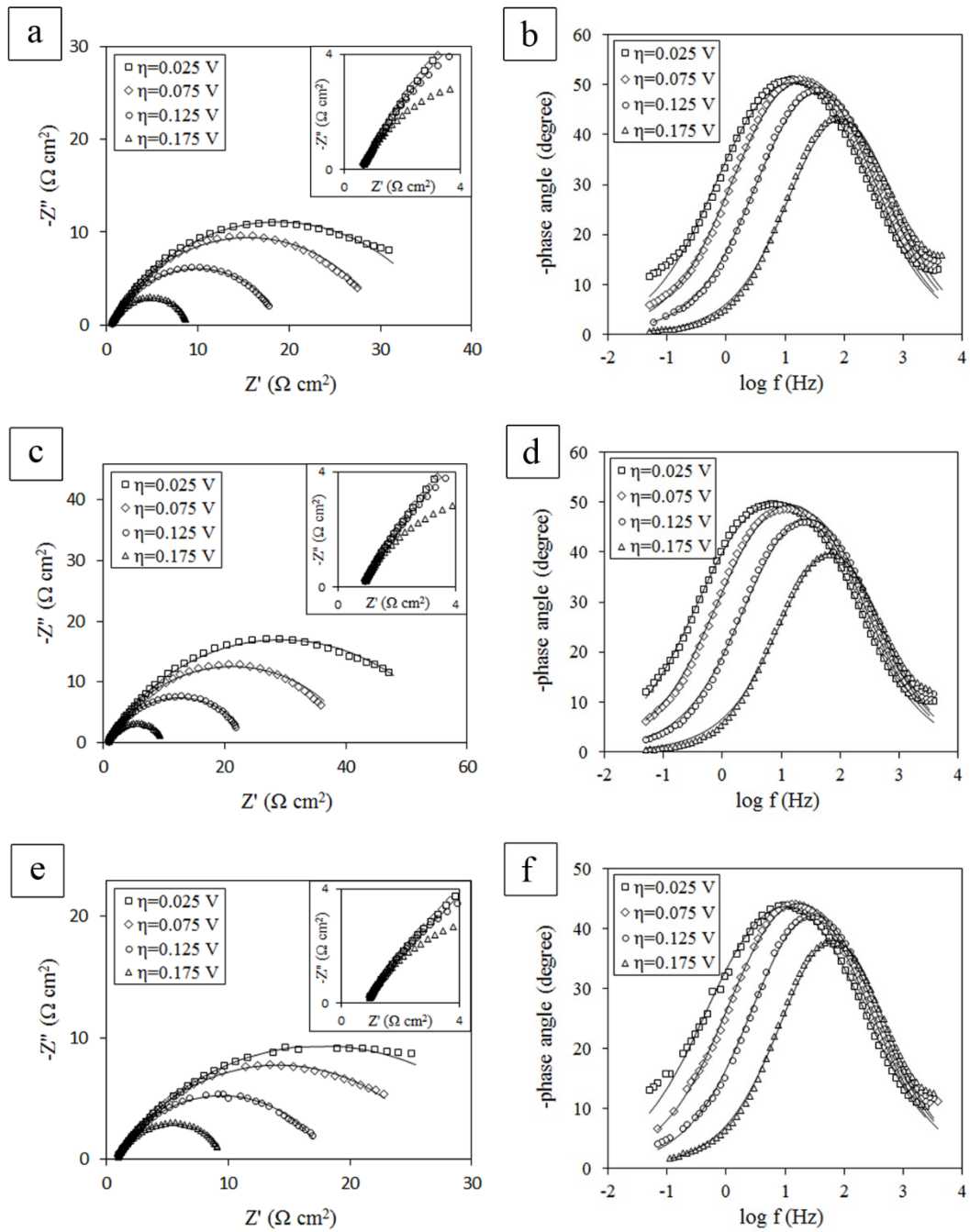
Figure 6.12- Experimental complex plane plots and phase-angle Bode plots obtained for the cold sprayed samples in 1 M NaOH: (a and b) C1, (c and d) C2, and (e and f) C3. The insets show the high frequency regions.

Table 6.5- Values of the circuit elements and their standard errors obtained by 1-CPE model for electrodes C1, C2, and C3 at 0.025, 0.075, 0.125, 0.175 V overpotentials in 1 M NaOH.

η (V)	R_s (Ω cm^2)	R_{ct} (Ω cm^2)	T (F cm^{-2} s$^{\phi-1}$)	ϕ	C_{dl} (F cm^{-2})	R_f	χ^2
C1							
0.025	0.61 ± 0.01	36.20 ± 0.01	0.010	0.70	8.60×10^{-3}	430	1.50×10^{-2}
0.075	0.61 ± 0.01	29.81 ± 0.01	0.008	0.72	6.93×10^{-3}	347	3.42×10^{-2}
0.125	0.62 ± 0.01	18.69 ± 0.01	0.006	0.74	5.30×10^{-3}	265	2.39×10^{-2}
0.175	0.62 ± 0.01	8.58 ± 0.01	0.004	0.77	3.52×10^{-3}	176	2.54×10^{-2}
C2							
0.025	0.85 ± 0.01	56.80 ± 0.01	0.009	0.68	8.50×10^{-3}	425	1.13×10^{-2}
0.075	0.84 ± 0.01	40.90 ± 0.01	0.007	0.70	6.60×10^{-3}	330	1.80×10^{-2}
0.125	0.85 ± 0.01	23.44 ± 0.01	0.005	0.72	4.73×10^{-3}	237	1.57×10^{-2}
0.175	0.86 ± 0.01	9.45 ± 0.01	0.003	0.74	3.21×10^{-3}	161	7.38×10^{-3}
C3							
0.025	0.86 ± 0.01	33.60 ± 0.01	0.013	0.65	1.22×10^{-2}	610	9.06×10^{-3}
0.075	0.87 ± 0.01	26.51 ± 0.01	0.009	0.67	8.50×10^{-3}	425	7.72×10^{-3}
0.125	0.89 ± 0.01	17.20 ± 0.01	0.007	0.69	6.65×10^{-3}	333	1.11×10^{-2}
0.175	0.89 ± 0.01	8.03 ± 0.01	0.005	0.73	4.01×10^{-3}	201	7.76×10^{-3}

Table 6.5 shows that the charge transfer resistance R_{ct} of the electrodes is directly related to their exchange current densities. Electrode C3 with a higher strain accumulation and improved electronic properties exhibited enhanced exchange current density, and hence, a lower charge transfer resistance. As shown in Eq. 6.4 parameter ϕ is one of the parameters that is used to determine the impedance of the CPE and it is related to the chemical and physical surface inhomogeneities [49]. Therefore, deviation of this parameter from unity at all overpotentials shows its divergence from purely capacitive impedance due

to the energetically inhomogeneous surfaces formed by the peening effect (Table 6.5). Double layer capacitance (C_{dl}) of the electrodes, shown in Table 6.5, was also calculated according to Eq. 6.5, and its dependence on the overpotential is shown in Figure 6.13. C_{dl} values also confirm that C3 had the largest and C2 had the smallest active electrode surfaces. The results are in agreement with those obtained from the Tafel measurements. Decreased double layer capacitance values at higher overpotentials of each electrode could be related to the change of the electrochemically active surface area by intensification of the HER and occlusion of fractions of the active surfaces by H_2 gas bubbles.
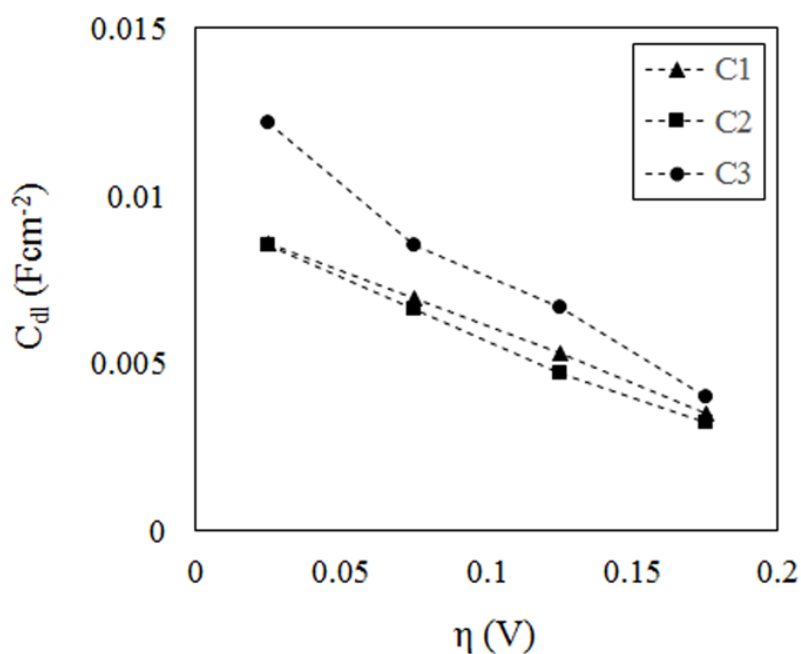
Figure 6.13- Dependence of the electrocatalytic double layer capacitance on the overpotential for different cold sprayed samples.

The roughness factor (R_f) of the electrodes was evaluated as the ratio of the C_{dl} of the electrodes to a smooth nickel surface with the value of 20 μF cm^{-2} [50], and the results are presented in Table 6.5. The results indicate that electrode C3 had the highest roughness values at all overpotentials. It is worth noting that the electrochemical roughness includes the atomic scale roughness in addition to the micro- and macroscopic roughness. The atomic scale roughness is affected by the presence of surface energetic inhomogeneities

116

such as dislocations [51]. Therefore, the larger roughness factor of electrode C3 could be related to its higher compressive stress induced by more intense peening of its surface compared to electrodes C1 and C2, even though it had a lower microscopic roughness (Table 6.3).

The intrinsic activity of the electrodes was then calculated by dividing the apparent exchange current density of each electrode by the roughness factor at a chosen overpotential of 175 mV, using the data provided in Tables 6.4 and 6.5. For electrodes C1, C2 and C3, the intrinsic activity was evaluated 7.73×10^{-7}, 6.58×10^{-7} and 1.69×10^{-6} A cm^{-2}, respectively. These values confirm that electrode C3 yields the highest electrocatalytic activity, which not only is related to its enhanced real electrochemically active surface area but also to its increased intrinsic activity due to the improved electronic properties caused by the peening effect.

It is important to mention that the obtained apparent and real electrocatalytic activities are comparable to those achieved using other electrode production methods such as plasma spray [52], arc spray [37], electrodeposition [53, 54], and mechanical alloying [55] even when nickel alloys and Raney nickel were used. This shows the capability of cold spray for fabrication of active electrodes for the HER and it needs to be further investigated using nickel alloys and Raney nickel.

6.4 Conclusions

The effect of cold spraying parameters including pressure and temperature of the propellant gas on the electrocatalytic activity of three nickel coated electrodes was investigated. The coating created at the lowest particle impact velocity caused by reduced propellant gas pressure demonstrated the highest apparent and real activity, measured by steady state polarization curves and EIS. Since almost similar grain boundary densities were detected on the top surfaces of all three electrodes, higher activity of this electrode was related to the expected higher density of dislocations in grain interiors and more favorable adsorption energies of atomic hydrogen on the electrode surface induced by strain accumulation. It is assumed that the particles that could not contribute to deposition and bounced-off the surface shot peened the coating and introduced a higher intense plastic deformation. This

hypothesis was confirmed by larger residual stress, formation of severely deformed particles and craters at the top surface as well as the lowest specific surface area and roughness values that were obtained.

The results imply that the electrodes manufactured by cold spraying and shot peening of their surfaces could be effectively used for hydrogen evolution by water electrolysis process. Minimal oxidation of the cold sprayed electrodes along with the formation of ultrafine microstructures due to the severe plastic deformation of their shot peened surfaces, attributes to higher electrocatalytic activities, and thus, increased efficiency of the electrolysis process. Application of this technique using more active electrocatalysts, such as Raney nickel, needs to be investigated, where a larger surface area contributes to further enhancement in efficiency of the HER.

CHAPTER 7

CONCLUSIONS, CONTRIBUTIONS AND RECOMMENDATIONS

7.1 Summary and conclusions

Different thermal spraying methods including atmospheric plasma spray, suspension plasma spray, high velocity oxy-fuel and cold spray were used to produce nickel cathode electrodes for hydrogen production by alkaline water electrolysis. The apparent and intrinsic electrocatalytic activities of the manufactured electrodes were improved for the HER by enhancing their real surface areas and increasing their defect densities.

For the electrodes that were produced using atmospheric and suspension plasma spray, the spraying parameters were optimized to maximize their real surface area. The top surfaces of the coatings were composed of large splats with splashed droplets and dispersed cauliflower-like aggregates when APS and SPS were used, respectively. Both coatings exhibited high levels of porosity. The two coating techniques were then combined by addition of SPS layers on top of the APS deposited ones. As a result, electrode surfaces with hybrid (nano/micron) surface asperities and increased specific surface areas were obtained. Such electrode structures provide larger active surface areas for the HER, where the micron sized features promote departure of the bubbles, and the nanostructured features favor easier electron transfer by providing more reaction sites. In addition, these electrodes exhibited superhydrophilic behavior with contact angles well below 10°, which further facilitate the bubble separation from the surface as the electrolyte is more likely to replace

the gas bubbles. The number of passes added by SPS was also optimized to enhance the active sites for hydrogen evolution while preventing screening a portion of the surface by hydrogen bubbles due to the excessive size reduction of the pores. Consequently, the electrode with optimized surface morphology and roughness showed the largest specific surface area and demonstrated the highest electrochemical performance for hydrogen evolution.

To further enhance the active surface area, and thus improve the electrocatalytic activity of the electrodes, their surfaces were engineered by deposition of three-dimensional fin arrays. For this purpose, the substrates were masked by wire mesh screens with different mesh densities during APS process. Subsequently the mesh screens were removed and the electrodes were coated by additional SPS layers. Similar masking approach was also taken when HVOF was used for the coating process. In this case, the coating parameters were selected to decrease the temperature of the oxy-fuel gas, prevent complete melting of the coating particles and reduce oxidation. For these electrodes that were coated by the combination of mesh screens and either plasma spray or HVOF processes, the electrochemical activities were significantly increased compared to those coated without using a mesh. The improved activities were associated with the engineered surfaces composed of a variety of macro- and microscopic surface roughness levels and structures. The unique microstructures were developed due to the impact of the particles at normal and off-normal angles on the produced fins and underneath the mesh wires. Such coating structures with hierarchical roughness values and surface asperities increase the rate of the HER by providing a larger active electrode surface area alongside facilitating the detachment of the hydrogen bubbles from the surface. It was shown that the activity was mainly affected by the developed microstructures, where the macroscopic surface added by the fins had a minor effect on it. Nonetheless, the plasma sprayed electrode showed a better activity when the screen with a higher mesh density was used for masking, whereas for the HVOF sprayed electrode a higher electrocatalytic activity was obtained when the screen with lower mesh density was used. This contradiction could be explained by the nature of the coating processes, where the particles were fully melted when plasma spray was used due to the high temperature of the plasma jet, whereas the particles were partially- or unmelted when HVOF was used due to the selected parameters to reduce the

oxy-fuel gas temperature. Therefore, the coatings were composed of flattened splats when plasma spray and unmelted particles when HVOF were employed for the deposition process. As a result, different surface microstructures and roughness levels were obtained on each part of the electrodes, depending on the spraying process that was used.

Cold spray was also used to manufacture electrodes by deposition of the particles at near room temperatures. The oxidation level was minimized as the particles deposited in solid state. The coatings were formed by severe deformation of the particles upon impact at high velocities. The electrode manufactured at the lowest particle impact velocity caused by the reduced pressure of the propellant gas demonstrated the highest apparent and real electrocatalytic activities, measured by steady state polarization curves and EIS. For this electrode, the impinging particles that could not deposit at low impact velocities, rebound from the surface, introduced intensive plastic deformation on the deposited layers, and caused the formation of severely deformed particles and craters on the top surface. In addition, the peening of the surface by the bounced-off particles contributed to the creation of a large density of dislocations, formation of non-equilibrium grain boundaries, and sub-micron/ultrafine grain structures. This high density of surface defects alongside with the compressive residual stress is expected to cause improved electronic properties and favorable hydrogen adsorption energies. Consequently, a higher electrocatalytic activity was obtained for this electrode.

As it was shown, highly electrocatalytic active nickel electrodes could be manufactured by modification of the surface of the electrodes using different thermal spraying techniques. The best results obtained for each coating condition are summarized in Figure 7.1 and Table 7.1. The results indicate that for all the thermally sprayed electrodes, the exchange current density was significantly improved by more than two order of magnitude compared to a nickel electrode with a smooth surface. The highest exchange current density of 9.3×10^{-3} A/cm^2 was obtained for the electrode coated using a combination of HVOF and mesh screens, which is more than three order of magnitude higher than a smooth nickel surface. This electrode also showed the lowest overpotential of -306 mV, and it was characterized as the best electrocatalyst among all the thermally sprayed electrodes in this work. The obtained electrocatalytic activities are comparable to those reported in the literature, using different electrode production methods such as

plasma spray [52], arc spray [37], electrodeposition [53, 54], and mechanical alloying [55], where the main focus was mainly on enhancing the activities by using nickel alloys, such as Raney nickel and nickel-molybdenum. Therefore, considering that in this study the activities were mainly improved by surface modification of the electrodes, the obtained results show the high potential of the introduced methodologies to further promote the catalytic activities (intrinsic and apparent) when nickel alloys are employed.
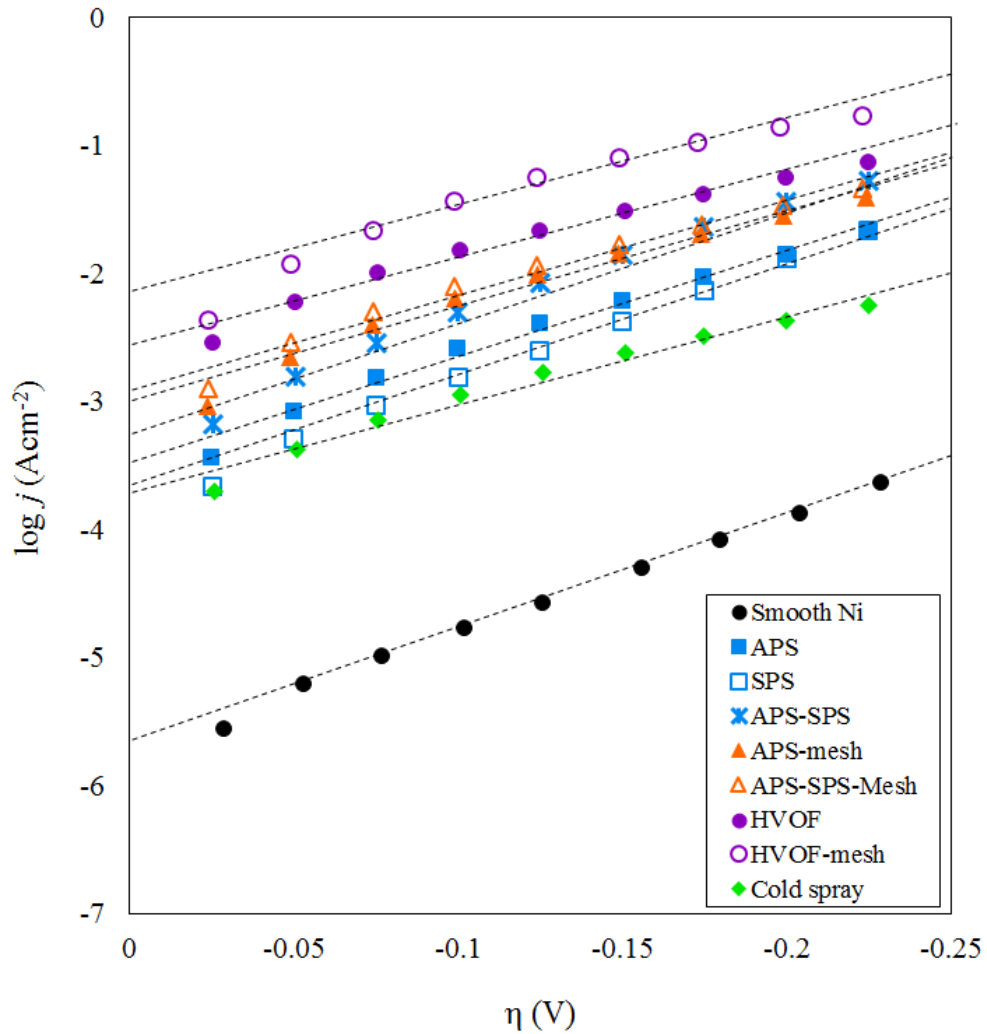
Figure 7.1- Steady-state polarization curves of the electrodes produced by various thermal spray processes, and a smooth nickel surface obtained in 1M NaOH.

Table 7.1- Kinetic parameters of the thermal sprayed electrodes, and smooth nickel surface for the HER in 1M NaOH solution.

Electrode	b (mV/dec)	j_0 (A/cm^2)	η_{250} (mV)
Smooth Ni	101	1.5×10^{-6}	-752
APS	118	3.1×10^{-4}	-451
SPS	108	1.8×10^{-4}	-570
APS-SPS	114	6.2×10^{-4}	-386
APS-mesh	152	1.4×10^{-3}	-366
APS-SPS mesh	156	1.8×10^{-3}	-336
HVOF	174	3.9×10^{-3}	-346
HVOF-mesh	168	9.3×10^{-3}	-306
Cold spray	186	3.41×10^{-4}	-

7.2 Contributions

As it was shown, highly electrocatalytic active nickel electrodes could be manufactured by modification of the surface of the electrodes, using different thermal spraying techniques. The main contributions of this research are summarized in the following.

- A detailed study was conducted to optimize the coating parameters used in atmospheric and suspension plasma spray and a combination of both methods to produce electrodes with large effective surface areas and enhanced electrocatalytic activities for the HER.

- Suspension plasma spray was used for the first time to manufacture electrodes for the HER by deposition of submicron- and nanosized particles.

- A combination of atmospheric and suspension plasma spray processes was introduced and effectively used as a novel method to develop multiscale (micron and nano) electrode surface structures for improved electrode performances for the HER.

- High velocity oxy-fuel and cold spray were used as newly emerged technologies for manufacturing nickel-based cathode electrodes for the HER by deposition of semi-solid and solid particles on the electrodes surfaces.

- Three-dimensional surface textures with remarkable morphologies were engineered by deposition of fin arrays on the electrodes using a combination of mesh screens and either plasma spray or HVOF processes.

- Peening of the electrode surface by the solid-state nickel particles during the cold spray deposition process contributed to enhanced electrocatalytic activities by increasing the surface defects and possibly changing the electronic structure of the electrodes.

7.3 Recommendation for future work

The work presented in this research identified several methodologies for producing highly electrocatalytic active electrode coatings for the HER. For further improvements for enhancing the electrocatalytic activity of the electrodes and a better understanding of the processes, some suggestions for the future research work is listed in this section.

- The reason for higher activity of the HVOF coated electrode compared to the electrodes coated with other thermal spray methods, all coated without using mesh screens, specifically cold sprayed electrodes needs to be investigated. Although a low level of oxidation is expected for both coatings deposited using HVOF and cold spray and they showed nearly similar top surface structures, a

significantly higher electrocatalytic activity was obtained for the HVOF coated electrode. Therefore, the microstructure and surface chemistry of the coatings need to be studied.

- Further optimization of the cold spray and HVOF parameters is subject to improvements towards increasing the activity of the developed coatings. In addition, deposition of submicron and nanosized particles by suspension plasma spray on HVOF and cold sprayed coatings need to be investigated. Moreover, the effect of formation of three dimensional fin arrays using mesh screens and cold spray should be investigated.

- The number of suspension plasma sprayed layers when mesh screens were used to develop three dimensional coatings need to be optimized for further enhancement of the activity. Furthermore, the effect of mesh distance from the substrate on the morphology, roughness and activity of the coatings needs to be studied.

- The intrinsic activity of the electrodes may be increased and optimized alongside the enhancement of the real surface area of the electrodes. Therefore, manufacturing electrodes using the thermal sprayed coatings by deposition of Raney nickel and nickel-molybdenum alloys need to be investigated using the optimum coating conditions of each process. Addition of pore forming materials during the coating processes to enhance the electrode real surface area is also suggested to be examined.

- Life cycle assessment of the employed thermal spray processes and the deposited electrodes in the context of green manufacturing is suggested to be carried out.

- Long-term stability of the developed electrodes for the HER needs to be investigated.

References

[1] A. Ursua, L.M. Gandia, P. Sanchis, Hydrogen production from water electrolysis: current status and future trends, Proceedings of the IEEE, 100 (2012) 410-426.

[2] W. Hu, Electrocatalytic properties of new electrocatalysts for hydrogen evolution in alkaline water electrolysis, International Journal of Hydrogen Energy, 25 (2000) 111-118.

[3] http://cleanenergycanada.org/, 2015.

[4] http://www.nrcan.gc.ca/home, DOI (2015).

[5] M.I. Hoffert, K. Caldeira, G. Benford, D.R. Criswell, C. Green, H. Herzog, A.K. Jain, H.S. Kheshgi, K.S. Lackner, J.S. Lewis, Advanced technology paths to global climate stability: energy for a greenhouse planet, science, 298 (2002) 981-987.

[6] T.B. Johansson, Renewable energy: sources for fuels and electricity, Island press1993.

[7] F. Barbir, PEM electrolysis for production of hydrogen from renewable energy sources, Solar energy, 78 (2005) 661-669.

[8] L. Schlapbach, A. Züttel, Hydrogen-storage materials for mobile applications, Nature, 414 (2001) 353-358.

[9] J.D. Holladay, J. Hu, D.L. King, Y. Wang, An overview of hydrogen production technologies, Catalysis Today, 139 (2009) 244-260.

[10] E. Zoulias, E. Varkaraki, N. Lymberopoulos, C.N. Christodoulou, G.N. Karagiorgis, A review on water electrolysis, TCJST, 4 (2004) 41-71.

[11] D.M. Santos, C.A. Sequeira, J.L. Figueiredo, Hydrogen production by alkaline water electrolysis, Química Nova, 36 (2013) 1176-1193.

[12] J. Turner, G. Sverdrup, M.K. Mann, P.C. Maness, B. Kroposki, M. Ghirardi, R.J. Evans, D. Blake, Renewable hydrogen production, International Journal of Energy Research, 32 (2008) 379-407.

[13] K. Zeng, D. Zhang, Recent progress in alkaline water electrolysis for hydrogen production and applications, Progress in Energy and Combustion Science, 36 (2010) 307-326.

[14] D.L. Stojić, M.P. Marčeta, S.P. Sovilj, Š.S. Miljanić, Hydrogen generation from water electrolysis—possibilities of energy saving, Journal of Power Sources, 118 (2003) 315-319.

[15] C. Fan, D. Piron, Electrodeposition as a means of producing large-surface electrodes required in water electrolysis, Surface and Coatings Technology, 73 (1995) 91-97.

[16] C. Fan, D. Piron, A. Sleb, P. Paradis, Study of Electrodeposited Nickel-Molybdenum, Nickel-Tungsten, Cobalt-Molybdenum, and Cobalt-Tungsten as Hydrogen Electrodes in Alkaline Water Electrolysis, Journal of the Electrochemical Society, 141 (1994) 382-387.

[17] J.B. Allen, R.F. Larry, Electrochemical methods: fundamentals and applications, 2nd ed ed., Wiley, New York2001.

[18] A. Lasia, A. Rami, Kinetics of hydrogen evolution on nickel electrodes, Journal of electroanalytical chemistry and interfacial electrochemistry, 294 (1990) 123-141.

[19] S. Trasatti, W. O'Grady, H. Gerischer, C. Tobias, Advances in electrochemistry and electrochemical engineering, Vol. 10Wiley, New York, DOI (1977) 213.

[20] H. Suffredini, J. Cerne, F. Crnkovic, S. Machado, L. Avaca, Recent developments in electrode materials for water electrolysis, International Journal of Hydrogen Energy, 25 (2000) 415-423.

[21] B. Conway, G. Jerkiewicz, Relation of energies and coverages of underpotential and overpotential deposited H at Pt and other metals to the 'volcano curve'for cathodic H 2 evolution kinetics, Electrochimica Acta, 45 (2000) 4075-4083.

[22] A. Nidola, Water electrolysis in alkaline solutions. New electrode materials, International journal of hydrogen energy, 9 (1984) 367-375.

[23] M. Wang, Z. Wang, X. Gong, Z. Guo, The intensification technologies to water electrolysis for hydrogen production–A review, Renewable and Sustainable Energy Reviews, 29 (2014) 573-588.

[24] M. Janjua, R. Le Roy, Electrocatalyst performance in industrial water electrolysers, International Journal of Hydrogen Energy, 10 (1985) 11-19.

[25] D. Soares, O. Teschke, I. Torriani, Hydride effect on the kinetics of the hydrogen evolution reaction on nickel cathodes in alkaline media, Journal of The Electrochemical Society, 139 (1992) 98-105.

[26] L. Birry, A. Lasia, Studies of the hydrogen evolution reaction on Raney nickel—molybdenum electrodes, Journal of applied electrochemistry, 34 (2004) 735-749.

[27] B. Łosiewicz, A. Budniok, E. Rówiński, E. Łągiewka, A. Lasia, The structure, morphology and electrochemical impedance study of the hydrogen evolution reaction on the modified nickel electrodes, International Journal of Hydrogen Energy, 29 (2004) 145-157.

[28] F. Crnkovic, S. Machado, L. Avaca, Electrochemical and morphological studies of electrodeposited Ni–Fe–Mo–Zn alloys tailored for water electrolysis, International Journal of Hydrogen Energy, 29 (2004) 249-254.

[29] I. Herraiz-Cardona, E. Ortega, J.G. Antón, V. Pérez-Herranz, Assessment of the roughness factor effect and the intrinsic catalytic activity for hydrogen evolution reaction on Ni-based electrodeposits, international journal of hydrogen energy, 36 (2011) 9428-9438.

[30] I.A. Raj, K. Vasu, Transition metal-based hydrogen electrodes in alkaline solution—electrocatalysis on nickel based binary alloy coatings, Journal of applied electrochemistry, 20 (1990) 32-38.

[31] D. Brown, M. Mahmood, M. Man, A. Turner, Preparation and characterization of low overvoltage transition metal alloy electrocatalysts for hydrogen evolution in alkaline solutions, Electrochimica Acta, 29 (1984) 1551-1556.

[32] E. Navarro-Flores, Z. Chong, S. Omanovic, Characterization of Ni, NiMo, NiW and NiFe electroactive coatings as electrocatalysts for hydrogen evolution in an acidic medium, Journal of Molecular Catalysis A: Chemical, 226 (2005) 179-197.

[33] N. Krstajić, V. Jović, L. Gajić-Krstajić, B. Jović, A. Antozzi, G. Martelli, Electrodeposition of Ni–Mo alloy coatings and their characterization as cathodes for hydrogen evolution in sodium hydroxide solution, International Journal of Hydrogen Energy, 33 (2008) 3676-3687.

[34] M.G. de Chialvo, A. Chialvo, Hydrogen evolution reaction on smooth Ni $(1-x)+$ Mo (x) alloys $(0 \le x \le 0.25)$, Journal of Electroanalytical Chemistry, 448 (1998) 87-93.

[35] M. Jakšić, Electrocatalysis of hydrogen evolution in the light of the brewer—engel theory for bonding in metals and intermetallic phases, Electrochimica Acta, 29 (1984) 1539-1550.

[36] M.M. Jaksic, Interionic nature of synergism in catalysis and electrocatalysis, Solid State Ionics, 136 (2000) 733-746.

[37] H. Ezaki, M. Morinaga, S. Watanabe, Hydrogen overpotential for transition metals and alloys, and its interpretation using an electronic model, Electrochimica acta, 38 (1993) 557-564.

[38] S. Marini, P. Salvi, P. Nelli, R. Pesenti, M. Villa, M. Berrettoni, G. Zangari, Y. Kiros, Advanced alkaline water electrolysis, Electrochimica Acta, 82 (2012) 384-391.

[39] G. Schiller, R. Henne, V. Borck, Vacuum plasma spraying of high-performance electrodes for alkaline water electrolysis, Journal of Thermal Spray Technology, 4 (1995) 185-194.

[40] D. Miousse, A. Lasia, V. Borck, Hydrogen evolution reaction on Ni-Al-Mo and Ni-Al electrodes prepared by low pressure plasma spraying, Journal of applied electrochemistry, 25 (1995) 592-602.

[41] R. Mishra, R. Balasubramaniam, Effect of nanocrystalline grain size on the electrochemical and corrosion behavior of nickel, Corrosion Science, 46 (2004) 3019-3029.

[42] X. Zhao, Y. Ding, L. Ma, X. Shen, S. Xu, Structure, morphology and electrocatalytic characteristics of nickel powders treated by mechanical milling, international journal of hydrogen energy, 33 (2008) 6351-6356.

[43] N. Jiang, H.-M. Meng, L.-J. Song, H.-Y. Yu, Study on Ni–Fe–C cathode for hydrogen evolution from seawater electrolysis, international journal of hydrogen energy, 35 (2010) 8056-8062.

[44] W. Mingyong, W. Zhi, G. Xuzhong, G. Zhancheng, The Intensification Technologies to Water Electrolysis for Hydrogen Production - A Review, Renewable and Sustainable Energy Reviews, 29 (2014) 573-588.

[45] C. Bocca, A. Barbucci, G. Cerisola, Influence of Surface Finishing on the Electrocatalytic Properties of Nickel for the Oxygen Evolution Reaction (OER) in Alkaline Solution, International Journal of Hydrogen Energy, 23 (1998) 247-252.

[46] F.C. Crnkovic, S.A.S. Machadao, L.A. Avaca, Electrochemical and Morphological Studies of Electrodeposited Ni-Fe-Mo-Zn Alloys Tailored for Water Electrolysis, International Journal of Hydrogen Energy, 29 (2004) 249-254.

[47] A. Kellenberger, N. Vaszilcsin, W. Brandl, Roughness factor evaluation of thermal arc sprayed skeleton nickel electrodes, Journal of Solid State Electrochemistry, 11 (2007) 84-89.

[48] L. Chen, A. Lasia, Study of the Kinetics of Hydrogen Evolution Reaction on Nickel-Zinc Alloy Electrodes, Journal of The Electrochemical Society, 138 (1991) 3321-3328.

[49] T. Boruciński, S. Rausch, H. Wendt, Raney nickel activated H2-cathodes Part II: Correlation of morphology and effective catalytic activity of Raney-nickel coated cathodes, Journal of applied electrochemistry, 22 (1992) 1031-1038.

[50] Y. Kiros, S. Schwartz, Long-term hydrogen oxidation catalysts in alkaline fuel cells, Journal of power sources, 87 (2000) 101-105.

[51] J. Divisek, H. Schmitz, J. Balej, Ni and Mo coatings as hydrogen cathodes, Journal of applied electrochemistry, 19 (1989) 519-530.

[52] M. Al-Saleh, S. Kareemuddin, A. Al-Zakri, Novel methods of stabilization of Raney-Nickel catalyst for fuel-cell electrodes, Journal of power sources, 72 (1998) 159-164.

[53] C.B. Rodella, G. Kellermann, M.S.P. Francisco, M.H. Jordao, D. Zanchet, Textural and structural analyses of industrial Raney nickel catalyst, Industrial & Engineering Chemistry Research, 47 (2008) 8612-8618.

[54] H. Wendt, G. Kreysa, Electrochemical engineering: science and technology in chemical and other industries, Springer Science & Business Media1999.

[55] L.-H. Chien, R.L. Webb, Measurement of bubble dynamics on an enhanced boiling surface, Experimental Thermal and Fluid Science, 16 (1998) 177-186.

[56] S.H. Ahn, I. Choi, H.-Y. Park, S.J. Hwang, S.J. Yoo, E. Cho, H.-J. Kim, D. Henkensmeier, S.W. Nam, S.-K. Kim, Effect of morphology of electrodeposited Ni catalysts on the behavior of bubbles generated during the oxygen evolution reaction in alkaline water electrolysis, Chemical Communications, 49 (2013) 9323-9325.

[57] J. Xu, R. Miao, T. Zhao, J. Wu, X. Wang, A novel catalyst layer with hydrophilic–hydrophobic meshwork and pore structure for solid polymer electrolyte water electrolysis, Electrochemistry Communications, 13 (2011) 437-439.

[58] J. Chattopadhyay, H.R. Kim, S.B. Moon, D. Pak, Performance of tin doped titania hollow spheres as electrocatalysts for hydrogen and oxygen production in water electrolysis, International Journal of hydrogen energy, 33 (2008) 3270-3280.

[59] A.R. Kucernak, V.N.N. Sundaram, Nickel phosphide: the effect of phosphorus content on hydrogen evolution activity and corrosion resistance in acidic medium, Journal of Materials Chemistry A, 2 (2014) 17435-17445.

[60] E. Fabbri, A. Habereder, K. Waltar, R. Kötz, T. Schmidt, Developments and perspectives of oxide-based catalysts for the oxygen evolution reaction, Catalysis Science & Technology, 4 (2014) 3800-3821.

[61] R. Šimpraga, G. Tremiliosi-Filho, S. Qian, B. Conway, In situ determination of the 'real are factor'in H 2 evolution electrocatalysis at porous Ni☐ Fe composite electrodes, Journal of Electroanalytical Chemistry, 424 (1997) 141-151.

[62] R.K. Shervedani, A. Lasia, Evaluation of the surface roughness of microporous Ni–Zn–P electrodes by in situ methods, Journal of applied electrochemistry, 29 (1999) 979-986.

[63] A. Banerjee, M. Pai, S. Meena, A. Tripathi, S. Bharadwaj, Catalytic activities of cobalt, nickel and copper ferrospinels for sulfuric acid decomposition: The high temperature step in the sulfur based thermochemical water splitting cycles, international journal of hydrogen energy, 36 (2011) 4768-4780.

[64] J. Podesta, R. Piatti, A. Arvia, P. Ekdunge, K. Jüttner, G. Kreysa, The behaviour of Ni☐ Co☐ P base amorphous alloys for water electrolysis in strongly alkaline solutions prepared through electroless deposition, International journal of hydrogen energy, 17 (1992) 9-22.

[65] S. Sotiropoulos, I. Brown, G. Akay, E. Lester, Nickel incorporation into a hollow fibre microporous polymer: a preparation route for novel high surface area nickel structures, Materials Letters, 35 (1998) 383-391.

[66] P. Kedzierzawski, D. Oleszak, M. Janik-Czachor, Hydrogen evolution on hot and cold consolidated Ni–Mo alloys produced by mechanical alloying, Materials Science and Engineering: A, 300 (2001) 105-112.

[67] P. Los, A. Rami, A. Lasia, Hydrogen evolution reaction on Ni-Al electrodes, Journal of applied electrochemistry, 23 (1993) 135-140.

[68] M. Domínguez-Crespo, A. Torres-Huerta, B. Brachetti-Sibaja, A. Flores-Vela, Electrochemical performance of Ni–RE (RE= rare earth) as electrode material for hydrogen evolution reaction in alkaline medium, International Journal of Hydrogen Energy, 36 (2011) 135-151.

[69] J. Borodzinski, A. Lasia, Electrocatalytic properties of doped nickel boride based electrodes for the hydrogen evolution reaction, Journal of applied electrochemistry, 24 (1994) 1267-1275.

[70] S. Rausch, H. Wendt, Morphology and Utilization of Smooth Hydrogen-Evolving Raney Nickel Cathode Coatings and Porous Sintered-Nickel Cathodes, Journal of The Electrochemical Society, 143 (1996) 2852-2862.

[71] W.-F. Chen, C.-H. Wang, K. Sasaki, N. Marinkovic, W. Xu, J. Muckerman, Y. Zhu, R. Adzic, Highly active and durable nanostructured molybdenum carbide electrocatalysts for hydrogen production, Energy & Environmental Science, 6 (2013) 943-951.

[72] D. Chade, L. Berlouis, D. Infield, A. Cruden, P.T. Nielsen, T. Mathiesen, Evaluation of Raney nickel electrodes prepared by atmospheric plasma spraying for alkaline water electrolysers, International Journal of Hydrogen Energy, 38 (2013) 14380-14390.

[73] A. Kellenberger, N. Vaszilcsin, W. Brandl, N. Duteanu, Kinetics of hydrogen evolution reaction on skeleton nickel and nickel–titanium electrodes obtained by thermal arc spraying technique, International Journal of Hydrogen Energy, 32 (2007) 3258-3265.

[74] J.R. Davis, Handbook of thermal spray technology, ASM international2004.

[75] H. Herman, S. Sampath, R. McCune, Thermal spray: current status and future trends, Mrs Bulletin, 25 (2000) 17-25.

[76] L. Pawlowski, The science and engineering of thermal spray coatings, John Wiley & Sons2008.

[77] M. Oksa, E. Turunen, T. Suhonen, T. Varis, S.-P. Hannula, Optimization and characterization of high velocity oxy-fuel sprayed coatings: techniques, materials, and applications, Coatings, 1 (2011) 17-52.

[78] P. Fauchais, Understanding plasma spraying, Journal of Physics D: Applied Physics, 37 (2004) R86.

[79] T. Schmidt, F. Gärtner, H. Assadi, H. Kreye, Development of a generalized parameter window for cold spray deposition, Acta materialia, 54 (2006) 729-742.

[80] http://www.asminternational.org/web/tss/technical/white-paper.

[81] E. Pfender, Fundamental studies associated with the plasma spray process, Surface and Coatings Technology, 34 (1988) 1-14.

[82] T. Burchardt, V. Hansen, T. Våland, Microstructure and catalytic activity towards the hydrogen evolution reaction of electrodeposited NiP x alloys, Electrochimica Acta, 46 (2001) 2761-2766.

[83] F. Gitzhofer, E. Bouyer, M.I. Boulos, Suspension plasma spray Google Patents, 1997.

[84] P. Fauchais, R. Etchart-Salas, V. Rat, J.-F. Coudert, N. Caron, K. Wittmann-Ténèze, Parameters controlling liquid plasma spraying: Solutions, sols, or suspensions, Journal of Thermal Spray Technology, 17 (2008) 31-59.

[85] P. Fauchais, G. Montavon, R. Lima, B. Marple, Engineering a new class of thermal spray nano-based microstructures from agglomerated nanostructured particles, suspensions and solutions: an invited review, Journal of Physics D: Applied Physics, 44 (2011) 093001.

[86] P. Fauchais, G. Montavon, M. Vardelle, J. Cedelle, Developments in direct current plasma spraying, Surface and Coatings Technology, 201 (2006) 1908-1921.

[87] E. Irissou, J.G. Legoux, A. Ryabinin, B. Jodoin, C. Moreau, Review on Cold Spray Process and Technology. Part I. Intellectual Property, Journal of Thermal Spray Technology, 17 (2008) 495-516.

[88] J.V. Heberlein, P. Fauchais, M.I. Boulos, Thermal Spray Fundamentals: From Powder to Part, Springer US, 2014.

[89] P. Richer, A. Zuniga, M. Yandouzi, B. Jodoin, CoNiCrAlY Microstructural Changes Induced During Cold Gas Dynamic Spraying, Surface and Coatings Technology, 203 (2008) 364-371.

[90] D.L. Gilmore, R.C. Dykhuizen, R.A. Neiser, T.J. Roemer, M.F. Smith, Particle Velocity and Deposition Efficiency in the Cold Spray Process, Journal of Thermal Spray Technology, 8 (1999) 576-582.

[91] T. Stoltenhoff, H. Kreye, H.J. Richter, HCl An Analysis of the Cold Spray Process and Its Coatings, Journal of Thermal Spray Technology, 11 (2002) 542-550.

[92] F. Raletz, M. Vardelle, G. Ezo'o, Critical Particle Velocity Under Cold Spray Conditions, Surface & Coatings Technology, 201 (2006) 1942-1947.

[93] R.S. Lima, J. Karthikeyan, C.M. Kay, J. Lindemann, C.C. Berndt, Microstructural Characteristics of Cold-Sprayed Nanostructured WC-Co Coatings, Thin Solid Films, 416 (2002) 129-135.

[94] M. Grujicic, J.R. Saylor, D.E. Beasley, W.S. DeRosset, D. Helfritch, Computational Analysis of the Interfacial Bonding Between Feed-Powder Particles and the Substrate in the Cold-Gas Dynamic-Spray Process, Applied Surface Science, 219 (2003) 211-227.

[95] M. Grujicic, C.L. Zhao, W.S. De Rosset, D. Helfritch, Adiabatic Shear Instability Based Mechanism for Particles/Substrate Bonding in the Cold-Gas Dynamic-Spray Process, Materials & Design, 25 (2004) 681-688.

[96] T.G. Coker, S.D. Argade, Sprayed cathodes, Google Patents, 1977.

[97] J. Fournier, D. Miousse, J.-G. Legoux, Wire-arc sprayed nickel based coating for hydrogen evolution reaction in alkaline solutions, International journal of hydrogen energy, 24 (1999) 519-528.

[98] D. Hall, Plasma-sprayed nickel cathode coatings for hydrogen evolution in alkaline electrolytes, Journal of applied electrochemistry, 14 (1984) 107-115.

[99] R. Henne, Solid oxide fuel cells: a challenge for plasma deposition processes, Journal of Thermal Spray Technology, 16 (2007) 381-403.

[100] R.F. De Souza, G. Loget, J.C. Padilha, E.M. Martini, M.O. De Souza, Molybdenum electrodes for hydrogen production by water electrolysis using ionic liquid electrolytes, Electrochemistry Communications, 10 (2008) 1673-1675.

[101] R. Henne, W. Schnurnberger, W. Weber, Low pressure plasma spraying-properties and potential for manufacturing improved electrolysers, Thin solid films, 119 (1984) 141-152.

[102] V. Jović, U. Lačnjevac, B. Jović, N. Krstajić, Service life test of non-noble metal composite cathodes for hydrogen evolution in sodium hydroxide solution, Electrochimica Acta, 63 (2012) 124-130.

[103] X. Fei, Y. Niu, H. Ji, L. Huang, X. Zheng, A comparative study of MoSi 2 coatings manufactured by atmospheric and vacuum plasma spray processes, Ceramics International, 37 (2011) 813-817.

[104] E. Irissou, M. Blouin, L. Roué, J. Huot, R. Schulz, D. Guay, Plasma-sprayed nanocrystalline Ti–Ru–Fe–O coatings for the electrocatalysis of hydrogen evolution reaction, Journal of alloys and compounds, 345 (2002) 228-237.

[105] O. Marchand, E. Saoutieff, P. Bertrand, M.-P. Planche, O. Tingaud, G. Bertrand, Suspension Plasma Spraying to Manufacture Electrodes for Solid Oxide Fuel Cell (SOFC) and Solid Oxide Electrolysis Cell (SOEC), ECS Transactions, 25 (2009) 585-594.

[106] P. Michaux, G. Montavon, A. Grimaud, A. Denoirjean, P. Fauchais, Elaboration of porous NiO/8YSZ layers by several SPS and SPPS routes, Journal of thermal spray technology, 19 (2010) 317-327.

[107] P. Fauchais, R. Etchart-Salas, C. Delbos, M. Tognonvi, V. Rat, J.-F. Coudert, T. Chartier, Suspension and solution plasma spraying of finely structured layers: potential application to SOFCs, Journal of Physics D: Applied Physics, 40 (2007) 2394.

[108] F. Jabbari, M. Jadidi, R. Wuthrich, A. Dolatabadi, A Numerical Study of Suspension Injection in Plasma-Spraying Process, Journal of Thermal Spray Technology, 23 (2014) 3-13.

[109] C.M. Douglas, Design and analysis of experiments, John Wiley and sons, DOI (2001).

[110] D. Chen, E.H. Jordan, M. Gell, The solution precursor plasma spray coatings: influence of solvent type, Plasma Chemistry and Plasma Processing, 30 (2010) 111-119.

[111] Y. Shen, V.A.B. Almeida, F. Gitzhofer, Preparation of nanocomposite GDC/LSCF cathode material for IT-SOFC by induction plasma spraying, Journal of thermal spray technology, 20 (2011) 145-153.

[112] A. Ansar, D. Soysal, G. Schiller, Nanostructured functional layers for solid oxide fuel cells, International Journal of Energy Research, 33 (2009) 1191-1202.

[113] F. Tarasi, M. Medraj, A. Dolatabadi, J. Oberste-Berghaus, C. Moreau, Effective parameters in axial injection suspension plasma spray process of alumina-zirconia ceramics, Journal of Thermal Spray Technology, 17 (2008) 685-691.

[114] C. Bocca, A. Barbucci, G. Cerisola, The influence of surface finishing on the electrocatalytic properties of nickel for the oxygen evolution reaction (OER) in alkaline solution, International journal of hydrogen energy, 23 (1998) 247-252.

[115] D. Pletcher, Electrocatalysis: present and future, J Appl Electrochem, 14 (1984) 403-415.

[116] H. Wendt, H. Hofmann, V. Plzak, Materials research and development of electrocatalysts for alkaline water electrolysis, Materials chemistry and physics, 22 (1989) 27-49.

[117] R. Hui, Z. Wang, O. Kesler, L. Rose, J. Jankovic, S. Yick, R. Maric, D. Ghosh, Thermal plasma spraying for SOFCs: Applications, potential advantages, and challenges, Journal of Power Sources, 170 (2007) 308-323.

[118] M. Aghasibeig, M. Mousavi, F. Ben Ettouill, C. Moreau, R. Wuthrich, A. Dolatabadi, Electrocatalytically Active Nickel-Based Electrode Coatings Formed by Atmospheric and Suspension Plasma Spraying, J Therm Spray Tech, 23 (2014) 220-226.

[119] M. Aghasibeig, R. Wuthrich, C. Moreau, A. Dolatabadi, Electrocatalytic Behaviour of Nickel Coatings Formed by APS and SPS Processes, International Thermal Spray Conference and Exposition, ASM International, Barcelona, Spain, 2014, pp. 739-744.

[120] O. Cherstiouk, A. Gavrilov, L. Plyasova, I.Y. Molina, G. Tsirlina, E. Savinova, Influence of structural defects on the electrocatalytic activity of platinum, Journal of Solid State Electrochemistry, 12 (2008) 497-509.

[121] F. Gitzhofer, E. Bouyer, M.I. Boulos, Suspension plasma spray deposition, Google Patents, 1996.

[122] S. Rausch, H. Wendt, Raney-nickel activated H2-cathodes Part I: Modelling the current/voltage behaviour of flat Raney-nickel coated microporous electrodes, J Appl Electrochem, 22 (1992) 1025-1030.

[123] C. Marozzi, A. Chialvo, Development of electrode morphologies of interest in electrocatalysis: part 2: hydrogen evolution reaction on macroporous nickel electrodes, Electrochimica acta, 46 (2001) 861-866.

[124] A.F. Stalder, T. Melchior, M. Müller, D. Sage, T. Blu, M. Unser, Low-bond axisymmetric drop shape analysis for surface tension and contact angle measurements of sessile drops, Colloids and Surfaces A: Physicochemical and Engineering Aspects, 364 (2010) 72-81.

[125] M. Aghasibeig, C. Moreau, R. Wuthrich, A. Dolatabadi, Engineered Three-Dimensional Electrode Surfaces by HVOF Process for Hydrogen Production, To be submitted to Journal of thermal spray technology.

138

[126] S. Sampath, X. Jiang, J. Matejicek, A. Leger, A. Vardelle, Substrate temperature effects on splat formation, microstructure development and properties of plasma sprayed coatings Part I: Case study for partially stabilized zirconia, Materials Science and Engineering: A, 272 (1999) 181-188.

[127] M. Friis, C. Persson, J. Wigren, Influence of particle in-flight characteristics on the microstructure of atmospheric plasma sprayed yttria stabilized ZrO 2, Surface and coatings technology, 141 (2001) 115-127.

[128] S. Kuroda, T. Dendo, S. Kitahara, Quenching stress in plasma sprayed coatings and its correlation with the deposit microstructure, Journal of Thermal Spray Technology, 4 (1995) 75-84.

[129] A. McDonald, M. Lamontagne, C. Moreau, S. Chandra, Impact of plasma-sprayed metal particles on hot and cold glass surfaces, Thin Solid Films, 514 (2006) 212-222.

[130] J.O. Berghaus, J.-G. Legoux, C. Moreau, F. Tarasi, T. Chraska, Mechanical and thermal transport properties of suspension thermal-sprayed alumina-zirconia composite coatings, Journal of thermal spray technology, 17 (2008) 91-104.

[131] K. VanEvery, M.J. Krane, R.W. Trice, H. Wang, W. Porter, M. Besser, D. Sordelet, J. Ilavsky, J. Almer, Column formation in suspension plasma-sprayed coatings and resultant thermal properties, Journal of thermal spray technology, 20 (2011) 817-828.

[132] J. Ilavsky, A.J. Allen, G.G. Long, S. Krueger, C.C. Berndt, H. Herman, Influence of spray angle on the pore and crack microstructure of plasma-sprayed deposits, J. Am. Ceram. Soc., 80 (1997) 733-742.

[133] B. Bhushan, Y.C. Jung, Natural and biomimetic artificial surfaces for superhydrophobicity, self-cleaning, low adhesion, and drag reduction, Progress in Materials Science, 56 (2011) 1-108.

[134] M. Giz, S. Bento, E. Gonzalez, NiFeZn codeposit as a cathode material for the production of hydrogen by water electrolysis, International journal of hydrogen energy, 25 (2000) 621-626.

[135] S. Machado, J. Tiengo, P.D.L. Neto, L. Avaca, A novel procedure in the galvanic deposition of Zn alloys for the preparation of large area Ni and Ni-Co surfaces, Journal of applied Electrochemistry, 26 (1996) 431-437.

[136] M. Aghasibeig, M. Mousavi, F.B. Ettouill, C. Moreau, R. Wuthrich, A. Dolatabadi, Electrocatalytically Active Nickel-Based Electrode Coatings Formed by Atmospheric and Suspension Plasma Spraying, Journal of thermal spray technology, 23 (2014) 220-226.

[137] M. Aghasibeig, C. Moreau, A. Dolatabadi, R. Wuthrich, Fabrication of Nickel Electrode Coatings by Combination of Atmospheric and Suspension Plasma Spray Processes, Submitted to Surface and Coatings Technology.

[138] M. Aghasibeig, R. Wuthrich, C. Moreau, A. Dolatabadi, Electrocatalytic Behaviour of Nickel Coatings Formed by APS and SPS Processes International Thermal Spray Conference and Exposition, ASM International, Barcelona, Spain, 2014, pp. 739-744.

[139] M. Aghasibeig, H. Monajatizadeh, P. Bocher, A. Dolatabadi, R. Wuthrich, C. Moreau, Cold Spray as a Novel Method for Development of Nickel Electrode Coatings for Hydrogen Production, Accepted for publication in International Journal of Hydrogen Energy, DOI 10.1016/j.ijhydene.2015.09.123.

[140] F. Gitzhofer, E. Bouyer, M.I. Boulos, Atomized into droplets, injection into plasma discharge, vaporization and agglomeration into partially melted drops, Google Patents, 1997.

[141] Y. Cormier, P. Dupuis, B. Jodoin, A. Corbeil, Net shape fins for compact heat exchanger produced by cold spray, Journal of thermal spray technology, 22 (2013) 1210-1221.

[142] M. Aghasibeig, C. Moreau, A. Dolatabadi, R. Wuthrich, Fabrication of Nickel Electrode Coatings by Combination of Atmospheric and Suspension Plasma Spray Processes, Surface and Coating Technology, DOI (2015).

[143] C. Lyphout, P. Nylén, L. Östergren, Relationships Between Process Parameters, Microstructure, and Adhesion Strength of HVOF Sprayed IN718 Coatings, Journal of thermal spray technology, 20 (2011) 76-82.

[144] M. Aghasibeig, A. Dolatabadi, R. Wuthrich, C. Moreau, Three-Dimensional Electrode Coatings for Hydrogen Production Fabricated by Combined Atmospheric and Suspension Plasma Spray, To be submitted to Materials science and engineering: B.

[145] M. Li, P.D. Christofides, Modeling and Control of High-Velocity Oxygen-Fuel (HVOF) Thermal Spray: A Tutorial Review, Journal of thermal spray technology, 18 (2009) 753-768.

[146] Y. Cormier, P. Dupuis, B. Jodoin, A. Corbeil, Pyramidal Fin Arrays Performance Using Streamwise Anisotropic Materials by Cold Spray Additive Manufacturing, Journal of Thermal Spray Technology, DOI (2015) 1-13.

[147] W. Tillmann, I. Baumann, P. Hollingsworth, I.-A. Laemmerhirt, Influence of the Spray Angle on the Properties of HVOF Sprayed WC–Co Coatings Using (− 10+ 2 μm) Fine Powders, Journal of thermal spray technology, 22 (2013) 272-279.

[148] Š. Houdková, M. Kašparová, F. Zahálka, The influence of spraying angle on properties of HVOF sprayed hardmetal coatings, Journal of thermal spray technology, 19 (2010) 893-901.

[149] C. Li, W. Li, Y. Wang, H. Fukanuma, Effect of spray angle on deposition characteristics in cold spraying, May, 2003, pp. 5-8.

[150] P. Fauchais, A. Vardelle, M. Vardelle, M. Fukumoto, Knowledge concerning splat formation: an invited review, Journal of Thermal Spray Technology, 13 (2004) 337-360.

[151] B. Łosiewicz, A. Budniok, E. Rówiński, E. Łągiewka, A. Lasia, Effect of Heat-Treatment on the Mechanism and Kinetics of the Hydrogen Evolution Reaction on Ni—P+ TiO2+ Ti Electrodes, Journal of applied electrochemistry, 34 (2004) 507-516.

[152] M. Aghasibeig, C. Moreau, A. Dolatabadi, R. Wuthrich, Fabrication of Nickel Electrode Coatings by Combination of Atmospheric and Suspension Plasma Spray Processes, Submitted to Surface and Coating Technology.

ARTICLE: Electrocatalytic Behaviour of Nickel Coatings Formed by APS and SPS Processes

M. Aghasibeig, R. Wuthrich, C. Moreau, A. Dolatabadi

Department of Mechanical and Industrial Engineering, Concordia University
Montreal, QC H3G 1M8, Canada

Abstract

Atmospheric (APS), Suspension Plasma Spraying (SPS) and combination of both methods were used to fabricate porous nickel electrode coatings on Inconel 600 substrates. The morphology of the coatings, studied by SEM, revealed porous microstructures with large surface areas. Steady-state polarization curves were used to study the electrocatalytic activity of the reduced electrodes for hydrogen evolution reaction (HER). The electrode fabricated by a combination of APS and SPS techniques demonstrated the highest activity for HER. For this electrode, the kinetic parameters of apparent exchange current density and overpotential at 250 mA/cm^2 were measured to be 6.5×10^{-4} A/cm^2 and 636 mV respectively. The increased activity of the APS-SPS coated electrode was related to its

enhanced surface area with a good accessible triple phase boundaries formed by a combination of micron and nanosized features.

A.1 Introduction

Hydrogen produced by alkaline water electrolysis can be used as a renewable and clean energy carrier to replace conventional fuels. Hydrogen as a fuel can greatly reduce damaging effects of climate change by mitigating greenhouse gas emissions. However, high-energy consumption of the electrolysis process has made large-scale hydrogen production by this method economically unattractive [1, 2]. An approach to improve the energy efficiency of the electrolysis process is to reduce cell voltages at a given current by decreasing hydrogen production overpotentials and diminishing large voltage ohmic losses. Using intrinsically active electrodes with large porous surface areas lower the overpotentials and increase the efficiency of the process [3-5].

In recent years, nickel has been widely used as a cathode electrode material in HER, since it has relatively high electrocatalytic activity and much lower costs compared to noble metals, such as platinum [6, 7]. It has been shown that manufacturing porous nickel electrodes by using ulrafine powders greatly increases the surface area of the electrode that participates in HER by diminishing the grain size, and thus, it significantly enhances the electrocatalytic activity [7, 8]. In addition, nanocrytalline coatings have shown high stability in long-term and intermittent electrolysis conditions [9].

Various surface modification techniques have been used to manufacture porous nickel based electrodes for HER, including electrodeposition, sintering, vacuum deposition, pressing and rolling. Nonetheless, most of these processes exhibit considerable disadvantages, such as undesired decompositions and phase transformations due to high temperatures and long processing times, low mechanical stability of the coatings due to limitations of the coating thickness, multi-step production processes and environmental problems [10-14]. Among all electrode surface coating production techniques, plasma spraying overcomes some difficulties of other methods and is a fast and economical process to deposit coatings [1]. The porosity and surface area achieved by plasma spraying can be

controlled by interplay of process parameters [15]. Electrodes produced by this technique exhibit three-dimensional surfaces with a high surface roughness factor [16].

To take advantage of both process and material, plasma spraying of nano-sized nickel-based powder particles is considered to be a promising method for production of electrocatalytic active surface coatings. SPS, based on injection of a liquid feed stock, is a plasma spraying method developed for spraying sub-micron and nanosized particles. Although deposition of nano-structured porous coatings highly enhances the real surface area of the electrodes, excessive size reduction of pores may decrease the rate of mass transport, which reduces the electrocatalytic activity [17]. For a highly electrocatalytic active electrode, a large surface area with a good accessibility for diffusive mass transport of the reactants and their products inside the porous structure is required. At very small pore diameters high concentrations of dissolved hydrogen increases hydrogen pressure inside the pores. Additionally hydrogen bubbles blanket the inner surface of the pores, which causes loss of a fraction of the surface area that is efficiently used [18].

In this study, a combination of APS and SPS processes was used to manufacture electrodes with multi-scale porosity. It is expected that the nanosized structure provides the enhanced surface area while the microporous structure facilitates the mass transport and overcomes the hydrogen bubble blockage within the pores. Electrode's activity was measured towards HER, and it was compared to the electrodes produced by only APS and SPS coating processes.

A.2 Materials and methods

A.2.1 Materials and spray conditions

Nickel based electrodes were prepared by atmospheric and suspension plasma spraying techniques using a Sulzer Metco 3MB atmospheric plasma spraying gun mounted on a six-axis computer-controlled robotic arm. Precursor powders included nickel with the nominal particle size in the range of –75 to +45 μm (Metco 56C-NS) and nickel oxide with the nominal particle size in the range of –5 μm to +500 nm (FCM NiO-F) for APS and SPS coating processes, respectively, Figure A.1.
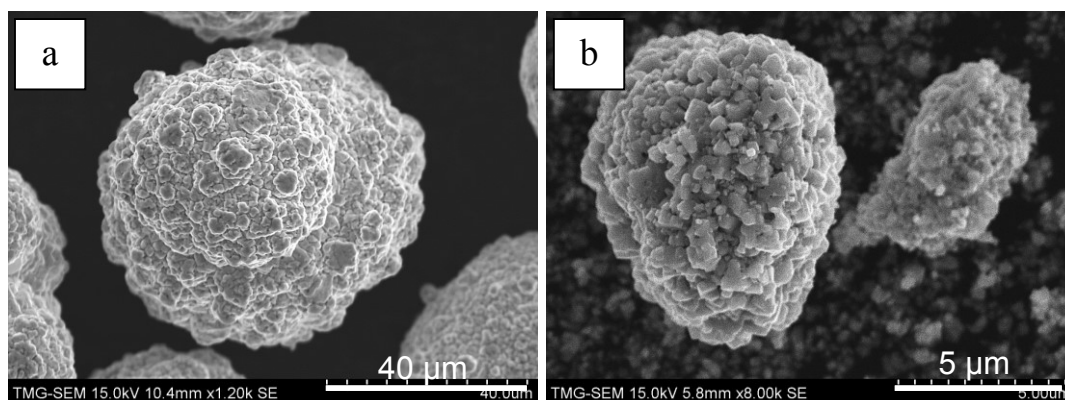
Figure A.1- SEM morphology of precursor powders: (a) Ni and (b) NiO powder.

The coatings were deposited on rectangular gritblasted Inconel 600 coupons with a surface area of 645 mm^2. Prior to spraying, the substrate coupons were grit blasted using 80 grit alumina with an air pressure of 70 psi (483 kPa) followed by ultrasonic cleaning in acetone. One electrode was also produced by deposition of a thin layer of SPS coating on the top surface of an APS coated electrode.

The spraying parameters used in the APS and SPS processes were obtained by optimization of a set of parameters towards maximizing the surface area of the coatings while having a good adhesion to the substrate, Table A.1 [19]. For both APS and SPS processes, the current was set at 500 A. 10, 20 and 10/10 over-layers were deposited to create APS, SPS and APS-SPS coated electrodes respectively.

Table A.1- Spraying parameters used in APS and SPS processes.

Process	Standoff distance (mm)	Feeding rate (g/min)	Plasma gas flow (Ar/H2) (NLPM)	Torch traverse speed (m/s)
APS	80	14	60/2	0.5
SPS	60	31.2	50/3	1

For the SPS process, a suspension containing 10 wt.% of NiO powder in ethanol as the solvent and 1 wt.% of polyvinylpyrrolidone (PVP) as the dispersing agent was

prepared. A 200-μm internal-diameter nozzle was used to inject the suspension into the plasma jet. The injection set-up for the SPS process is described in Reference 19.

To have a better understanding of the deposit build-up in APS, temperature and velocity of the inflight particles were measured at the point of impact, using a DPV-2000 system (TECNAR, Canada). DPV-2000 system is an online diagnostic system used to determine the characteristics of inflight particles based on their thermal radiation emission. However, it cannot be used in SPS due to the smaller size of the particles in the sprayed suspension. Temperature of the substrate during the APS coating process was monitored by an infrared (IR) camera (FLIR A320).

Since oxidation of the coatings is inevitable due to the high spraying temperatures in atmospheric environment and NiO powder was used in the SPS process as the precursor material, the coatings needed to be reduced to resume the activity of the electrodes. After deposition, the electrodes were reduced to Ni in a tube furnace at 650 °C in 4 vol.% H_2 balanced with N_2 atmosphere for 50 h.

To assess the extent of reduction of the electrodes, phase analysis of the electrodes was carried out by X-ray diffraction (XRD, X'Pert Pro; PANalytical, Almelo, The Netherlands) with Cu Ka radiation. Morphology of precursor powders and top surfaces of the coated electrodes was observed by a Hitachi S-3400N scanning electron microscope (SEM) before and after reduction.

A.2.2 Electrochemical characteristics

A three-electrode Pyrex cell was used to carry out the electrochemical measurements. A Pt wire was used as the counter electrode and an Hg/HgO electrode saturated in 1 M KOH as the reference electrode in a 1 M NaOH electrolytic solution. The electrolyte was bubbled with nitrogen gas during the measurements to remove the oxygen from the solution. All the measurements were performed at 22 °C. The value of the equilibrium potential for the hydrogen evolution reaction is -0.924 V versus Hg/HgO.

Tafel plots were obtained at a scan rate of 50 mV/s and in the current range of 10 μA to 100 mA using Princeton Applied Research potentiostat (Model 273A). Prior to each measurement, the working electrode was pre-polarized for 1800 s at -1.6 V vs. Hg/HgO.

A.3 Results and discussion

A.3.1 Composition and surface morphology

Top surface SEM image of the APS coated electrode shows that it is composed of fine 10-50 μm fragmented splats and semi-molten particles, Figure A.2. Presence of pores is evident in the top surface microstructure.
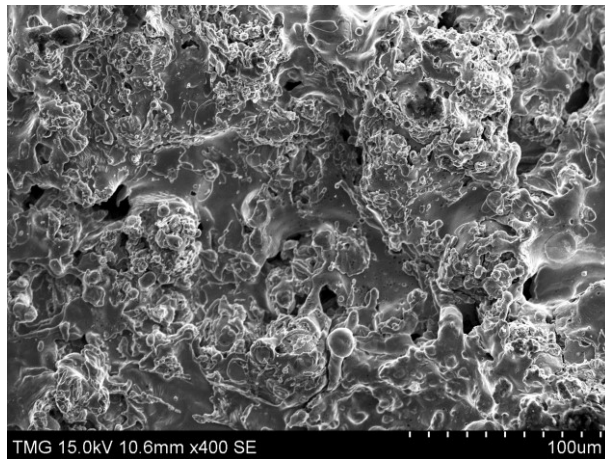

Figure A.2- SEM top surface micrograph of an APS
coated electrode.

It has been shown that the morphology of the splats and consequently the microstructure of the plasma sprayed coatings depend on numerous spraying factors. Substrate temperature and particle temperature and velocity at impact are demonstrated as the most influential factors controlling the deposit formation during the spraying process [20, 21]. For the APS coated electrode, the substrate's temperature was measured in the range of 90-150 °C during the coating process. Formation of small particles and splashed morphology as a product of fragmented splats on the coating can be related to the low temperature substrate, which results in a more porous structure. At lower substrate temperatures, the chance of gas entrapment in air pockets underneath the splats increases, which leads to higher splashing of the melted droplets and formation of larger pores and higher surface roughness after solidification of the splats [20, 22].

In order to achieve consistent and reproducible coatings, velocity and temperature of inflight particles were monitored during APS. During the spraying process, particles velocity and temperature are known to control the microstructure of the coatings to a large extend. Higher particle temperature and velocity result in higher particle flattening after impact to the substrate [21]. Temperature and velocity of the particles were measured $2451\pm119\ °C$ and 103 ± 18 m/s, respectively for more than 18,000 detected particles at the substrate standoff distance for the APS coated electrode. Therefore, besides substrate temperature, high temperature gradients of the impacted particles can also be responsible for the rough and porous surface structure of this electrode. The advantage of porous structure fabricated by APS is to provide more active sites for electrode/electrolyte interactions and an increased efficiency of the water electrolysis process.

Top surface SEM micrograph of the SPS coated electrode exhibits a fine porous microstructure composed of small unmelted and partially melted particles embedded in a structure of melted agglomerates with size of few tens of micrometres, Figure A.3. The coating exhibits a high level of pores, which can be linked to the presence of fine, untreated or poorly treated particles [23].
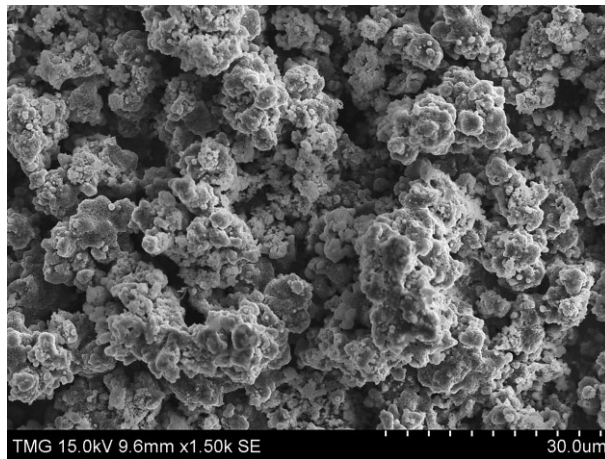

Figure A.3- SEM surface micrograph of a SPS coated electrode.

In SPS process, selection of the spraying conditions is more complicated compared to the conventional spraying methods. This complexity can be attributed to the demand of proper suspension penetration into the hot plasma jet, which strongly affects the degree of particle melting and porosity of the deposit. For the SPS coated electrode, the melted particles are those that penetrated into the core of the plasma jet, while unmelted and semi molten particles are those that passed through the periphery of the plasma jet with lower temperatures. Fauchais et al. [24] have shown that high instabilities and voltage fluctuations of the plasma jet (especially for Ar and H_2 plasma) in SPS process are responsible for non-uniform penetration and fragmentation of the particles at different zones of the plasma jet, which leads to the formation of porous microstructures. The nanostructured features along with a high level of porosity of the SPS coating, is advantageous for electrolysis applications. Such structure provides enhanced triple phase boundaries and offers more opportunity for the surface atoms to take part in the HER.

The electrode manufactured by SPS deposited on top surface of an APS coated sample reveals a microstructure with high roughness and porosity, Figure A.4. The microstructure is composed of nano and submicron-sized particles deposited by SPS on the surface of a porous structured coating with micron-sized features fabricated by APS.
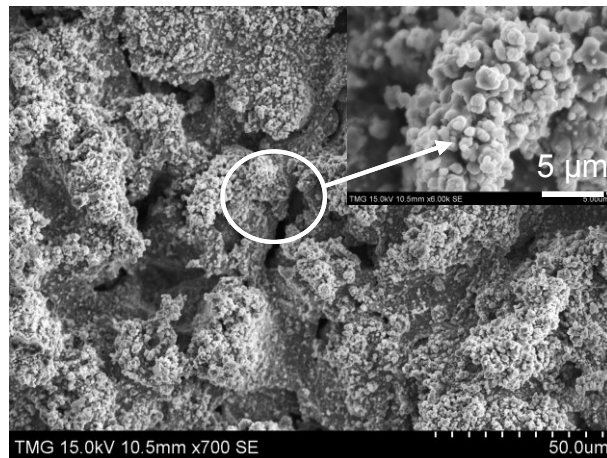

Figure A.4- SEM top surface micrograph of the electrode coated by SPS on the top surface of an APS coated substrate.

Porosity is an important factor for improving the surface area of cathode electrodes and their performance. In several works, it has been shown that the formation of SPS coatings on rough substrate surfaces greatly increases the porosity and surface area [25, 26]. Enhancement of the surface area can be related to the impact of nanosized particles on the existing surface asperities, which increases the coating porosity. In other words, as the roughness of the substrate increases, the spraying angle deviates locally from 90º on the surface asperities, which further increases the porosity [26, 27]. Therefore, the electrode coatings formed on rough substrates exhibit higher surfaces and better electrochemical performances [26]. For the current electrode coating, a large variation of porosity sizes and levels was obtained by combination of SPS and APS processes. This combined technique allows for manufacturing of unique microstructures. For this electrode, larger pores formed by the APS process promote the electrolyte diffusion, while the nano-sized protrusions (about 500 nm) enlarge the surface area. Maximizing the surface area by taking advantage of both micro and nanosized features can greatly enhance the electrode's performance. Combining nano and microporous structures by engineering the electrode's surface is beneficial for gas permeability and electrocatalytic activity [28].

Prior to electrochemical measurements, all electrodes were reduced using hydrogen and studied by XRD to ensure complete reduction of NiO to Ni. The XRD pattern obtained for the APS-SPS coated electrode showed no NiO content after reduction, Figure A.5. APS and SPS coated samples also followed the same XRD pattern, with slightly different amounts of nickel oxide.

One of the most important requirements for the electrodes after reduction is that the coatings retain their structure as NiO transforms to Ni. Coatings that do not contain oxygen after the reduction process, while their structure is not shrunk or densified, exhibit the best reduction conditions and show a good electrocatalytic activity for hydrogen evolution. Therefore, the surface structure of all electrodes was studied by SEM after the reduction process, and no volume shrinkage or densification was observed.
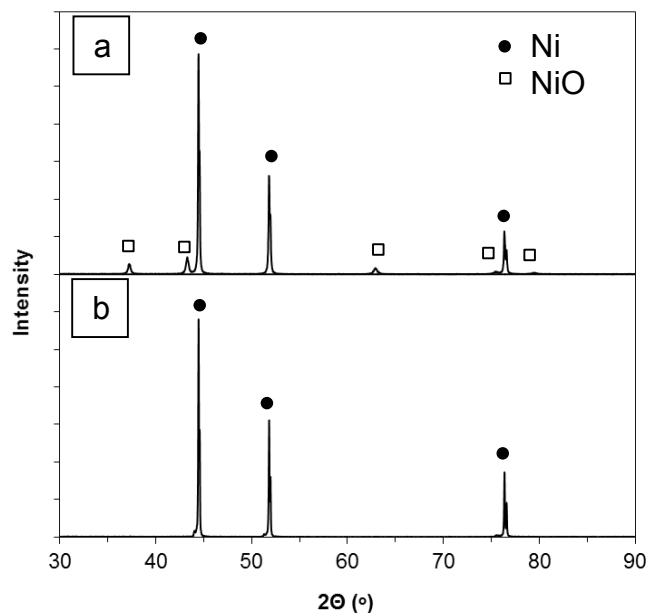
Figure A.5- XRD diagram of the APS-SPS coated electrode (a) before and (b) after reduction.

A.3.2 Steady-state polarization curves

Steady-state polarization curves were recorded for APS, SPS and APS-SPS Ni electrodes in 1 M NaOH solution at 22 °C. The catalytic activity of the electrodes was then evaluated by the apparent exchange current density obtained by extrapolation of the linear portion of the Tafel plots to the equilibrium potential divided by the projected geometrical surface area, Figure A.6. Corresponding kinetic parameters (Tafel slope b, apparent exchange current density j_0 and overpotential η) of the electrodes are summarized in Table A.2.
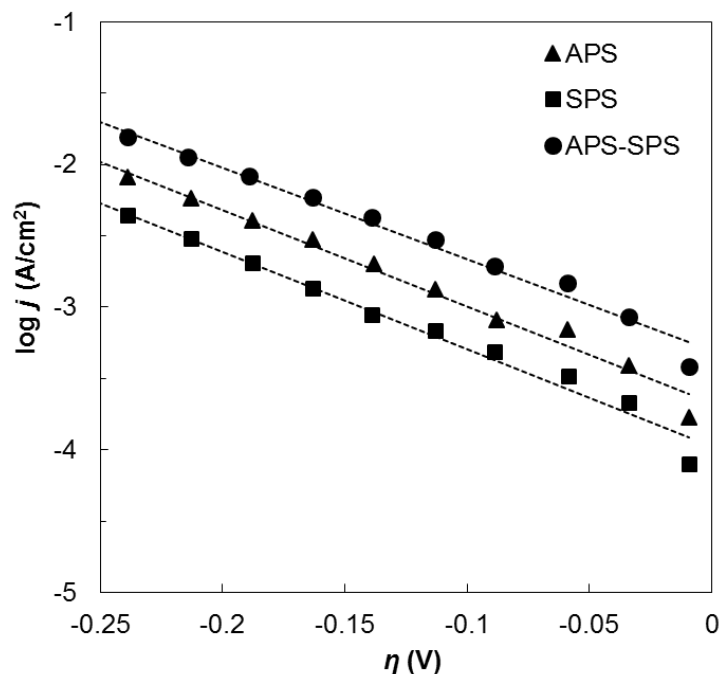
Figure A.6- Tafel curves obtained for APS, SPS and APS-
SPS Ni electrodes; j is the apparent current density.

Table A.2- Kinetic parameters obtained from steady-state polarization measurements.

Electrode	b (mV/dec)	j_0 (A/cm^2)	η_{250} (mV)
APS	156	2.7×10^{-4}	706
SPS	158	1.3×10^{-4}	746
APS-SPS	172	6.5×10^{-4}	636

The apparent exchange current densities of all samples were greatly increased compared to a smooth nickel sample with a reported value of $j_0=1.8 \times 10^{-6}$ A/cm^2 [29]. The larger activity of the coated electrodes is related to the surface morphology of the electrodes produced by the spraying process. The value of j_0 for the APS coated sample was measured 2.7×10^{-4} A/cm^2. However, this value reduced to 1.3×10^{-4} A/cm^2 for the SPS coated electrode.

153

As mentioned earlier, the activity of an electrode is highly related to the active surface area of that electrode. It is expected that an electrode with a larger specific surface area shows a better activity for the HER. It was shown that the surface area of the electrodes produced by SPS process is much larger compared to those coated by APS [19]. Therefore, a larger electrocatalytic activity was expected for the SPS coated electrode. For this electrode, the lower values of j_0 can be related to H_2 gas bubbles trapped in the inner surface of the pores in the absence of forced electrolyte convection, and less accessible electrode/electrolyte sites. In addition, presence of gas bubbles in the pores also can contribute to higher concentration polarization and ohmic resistance within the pores. However, more studies are required to confirm this hypothesis.

The APS-SPS coated electrode, with the j_0 value of 6.5×10^{-4} A/cm^2, shows the highest activity for HER. The increased activity can be related to the engineered surface of this electrode with a multi-scale porosity. The larger micropores make the surface area more accessible to the electrolyte, lower the surface occlusion by H_2 bubbles and facilitate the bubble ascension, while the nano-structured features enhance the surface area of the electrode and increase the opportunity of the surface atoms to take part in the HER. Finally, overpotential at 250 mA/cm^2 of the APS-SPS electrode characterized by the largest activity was measured to be 636 mV, which is lower compared to APS and SPS coated electrodes.

A.4 Conclusions

High performance porous Ni electrodes for alkaline water electrolysis were produced by APS, SPS and a combination of both processes. Top surface morphologies of all electrodes were studied by SEM. Electrocatalytic activity of the reduced electrodes for HER was determined using their steady-state polarization curves. The kinetic parameters including Tafel slope, apparent exchange current density and overpotential were determined for all coated electrodes. The electrode manufactured by a combination of APS and SPS processes revealed the highest electrocatalytic activity of 6.5×10^{-4} A/cm^2. The overpotential of this electrode at 250mA/cm^2 was measured to be 636 mV. The higher activity of this sample was related to the formation of nanosized features formed by SPS process on top of micron-sized asperities formed by the APS process. It is believed that the combination of both nano

and micron-scale microstructures manufactured an electrode with greatly enhanced surface area, where the larger micropores promote the electrolyte diffusion and facilitate H_2 bubble ascension from the pores and the nanosized features provide more active sites. For the SPS coated electrode smaller activity was obtained compared to the APS coated electrode. Blockage of the inner surface of the pores by gas bubbles, concentration polarization and ohmic resistance within the pores were identified as the potential reasons for lower activity of this electrode. However, further studies including electrochemical impedance spectroscopy and cross-sectional analyses are required to confirm this explanation.

References

[1] R. Henne, Solid oxide fuel cells: a challenge for plasma deposition processes, Journal of Thermal Spray Technology, 16 (2007) 381-403.

[2] W. Hu, Electrocatalytic properties of new electrocatalysts for hydrogen evolution in alkaline water electrolysis, International Journal of Hydrogen Energy, 25 (2000) 111-118.

[3] L. Birry, A. Lasia, Studies of the hydrogen evolution reaction on Raney nickel-molybdenum electrodes, Journal of applied electrochemistry, 34 (2004) 735-749.

[4] R. Henne, W. Schnurnberger, W. Weber, Low pressure plasma spraying-properties and potential for manufacturing improved electrolysers, Thin solid films, 119 (1984) 141-152.

[5] G. Schiller, R. Henne, V. Borck, Vacuum plasma spraying of high-performance electrodes for alkaline water electrolysis, Journal of Thermal Spray Technology, 4 (1995) 185-194.

[6] A.N. Correia, A.S.S. Machado, L.A. Avaca, Studies of the hydrogen evolution reaction on smooth Co and electrodeposited Ni-Co ultramicroelectrodes, Electrochemistry Communications, 12 (1999) 600-604.

[7] H. Ezaki, T. Nambu, M. Morinaga, M. Udaka, K. Kawasaki, Development of low hydrogen overpotential electrodes utilizing metal- ultra-fine particles, International Journal of Hydrogen Energy, 21 (1996) 877-881.

[8] D. Hall, Plasma-sprayed nickel cathode coatings for hydrogen evolution in alkaline electrolytes, Journal of applied electrochemistry, 14 (1984) 107-115.

[9] E. Irissou, M. Blouin, L. Roué, J. Huot, R. Schulz, D. Guay, Plasma-sprayed nanocrystalline Ti–Ru–Fe–O coatings for the electrocatalysis of hydrogen evolution reaction, Journal of alloys and compounds, 345 (2002) 228-237.

[10] M. Videa, D. Crespo, G. Casillas, G. Zavala, Electrodeposition of nickel-molybdenum nanoparticles for their use as electrocatalyst for the hydrogen evolution reaction, Journal of New Materials for Electrochemical Systems, 13 (2010) 239-244.

[11] A.M. Banerjee, M.R. Pai, S.S. Meena, A.K. Tripathi, S.R. Bharadwaj, Catalytic activities of cobalt, nickel, and copper ferrospinels for sulfuric acid decomposition: the high temperature step in the sulfur based thermochemical water splitting cycles, International Journal of Hydrogen Energy, 36 (2011) 4768-4780.

[12] K. Lohrberg, P. Kohl, Preparation and use of Raney-Ni activated cathodes for large scale hydrogen production, Electrochimica Acta, 29 (1984) 1557-1561.

[13] L. Chen, A. Lasia, Study of the kinetics of hydrogen evolution reaction on nickel-zinc powder electrodes, Journal of the Electrochemical Society, 139 (1992) 3214-3219.

[14] H. Dong, T. Lei, Y. He, N. Xu, B. Huang, C.T. Liu, Electrochemical performance of porous Ni_3Al electrodes for hydrogen evolution reaction, International Journal of Hydrogen Energy, 36 (2011) 12112-12120.

[15] H.D. Steffens, M. Mack, Plasma spraying as an advanced tool in surface engineering, Pure and Applied Chemistry 62 (1990) 1801-1808.

[16] A. Kellenberger, N. Vaszilcsin, W. Brandl, N. Duteanu, Kinetics of hydrogen evolution reaction on skeleton nickel and nickel-titanium electrodes obtained by thermal arc spraying technique, International Journal of Hydrogen Energy, 32 (2007) 3258-3265.

[17] T. Suzuki, Z. Hasan, Y. Funahashi, T. Yamaguchi, Y. Fujishiro, M. Awano, Impact of anode microstructure on solid oxide fuel cells, Science, 325 (2009) 852-855.

[18] S. Rausch, H. Wendt, Raney-nickel activated H_2-cathodes part I: modelling the current/voltage behavior of flat Raney nickel coated microporous electrodes, Journal of Applied Electrochemistry, 22 (1992) 1025-1030.

[19] M. Aghasibeig, M. Mousavi, F. Ben Ettouill, C. Moreau, R. Wuthrich, A. Dolatabadi, Electrocatalitically active nickel-based electrode coatings formed by atmospheric and suspension plasma spraying, Thermal Spray Technology, 23 (2014) 220-226.

[20] S. Sampath, X.Y. Jiang, J. Matejicek, A.C. Leger, A. Vardelle, Substrate temperature effects on splat formation, microstructure development and properties of plasma sprayed coatings part I: case study for partially stabilized zirconia, Materials Science and Engineering: A, 272 (1999) 181-188.

[21] M. Friis, C. Persson, J. Wigren, Influence of particle in-flight characteristics on the microstructure of atmospheric plasma sprayed yttria stabilized ZrO_2, Surface and Coating Technology, 141 (2001), 115-127.

[22] O. Sarikaya, Effect of some parameters on microstructure and hardness of alumina coatings prepared by the air plasma spraying process, Surface and Coating Technology, 190 (2005) 388-393.

[23] P. Fauchais, G. Montavon, G. Bertrand, From powders to thermally sprayed coatings, Journal of Thermal Spray Technology, 19 (2010) 56-80.

[24] P. Fauchais, R. Etchart-Salas, C. Delbos, M. Tognonvi, V. Rat, J.-F. Coudert, T. Chartier, Suspension and solution plasma spraying of finely structured layers: potential application to SOFCs, Journal of Physics D: Applied Physics, 40 (2007) 2394-2406.

[25] Y.C. Yang, Y.C. Chen, Influences of the processes on the microstructures and properties of the plasma sprayed IT-SOFC anode, Journal of the European Ceramic Society, 31 (2011) 3109-3118.

[26] M. Marr, O. Kesler, Permeability and microstructure of suspension plasma-sprayed YSZ electrolytes for SOFCs on various substrates, Journal of Thermal Spray Technology 21 (2012) 1334-1346.

[27] J. Ilavsky, A.J. Allen, G.G. Long, S. Krueger, C.C. Berndt, H. Herman, Influence of spray angle on the pore and crack microstructure of plasma-sprayed deposits, Journal of the American Ceramic Society, 80 (1997) 733-742.

[28] T. Burchardt, V. Hansen, T. Valand, Microstructure and catalytic activity towards the hydrogen evolution reaction of electrodeposited NiP_x alloys, Electrochimica. Acta, 46 (2001) 2761-2766.

[29] A. Lasia, A. Rami, Kinetics of hydrogen evolution on nickel electrodes, Journal of Electroanalytical Chemistry and Interfacial Electrochemistry, 294 (1990) 294-123.